# Correlating Structure and Function: An EPR Study on Cryptochromes, LOV Proteins and Channelrhodopsin

**Christopher Engelhard**

Im Fachbereich Physik der Freien Universität Berlin
zur Erlangung des Titels Doktor der
Naturwissenschaften eingereichte Dissertation

Fachbereich Physik
Freie Universität Berlin
Juli 2015

Erster Gutachter: Prof. Dr. Robert Bittl
Zweiter Gutachter: Prof. Dr. Andreas Möglich

Tag der Disputation: 30. November 2015

# SUMMARY

The perception of light is essential to many organisms, as it is an important source of spatial and temporal information. Accordingly, there are many photosensitive proteins that regulate behavioural and physiological responses. It is because of this that the investigation of photoreceptor proteins has garnered continued scientific interest.

One important aspect of a photosensor's mechanism is the conformation of the signalling state. Electron paramagnetic resonance (EPR) has been established as a useful tool for probing the structure of a protein in solution. This work utilises EPR to investigate three different proteins, YF1, cryptochrome-2 and channelrhodopsin-2.

YF1 is an example of a LOV protein, a diverse group of blue-light sensing proteins using a flavin chromophore. This work tries to elucidate the structure of the LOV domain's signalling state as well as investigate the molecular basis for LOV proteins' wide range of photocycle kinetics. Using EPR double resonance techniques, a structural model for the signalling state as well as a general motif for signal transduction is proposed. Photocycle kinetics are found to be influenced by amino acids in the chromophore's environment in a manner that is predictable and consistent over different LOV domains.

Cryptochromes are photosensing proteins closely related to photolyases. They, too, contain a flavin chromophore, and the photoreduction and following formation of a flavin radical has long been held as the important first step in the formation of the signalling state. However, recent experiments on cryptochrome variants that found them to be functional *in vivo* but lack photoreduction *in vitro*, have called this interpretation into question. This study addresses this issue, based on EPR's ability to detect the flavin radical even *in vivo*. The apparent contradiction is resolved by the finding that small metabolites like ATP play an important part in enabling flavin photoreduction *in vivo*.

Channelrhodopsins are light-gated ion channels from the rhodopsin protein family, that have recently come into the focus of research because of their potential for application in optogenetics. Information about the conformation of the open and closed states of channelrhodopsins is largely lacking. Using EPR-based distance measurements, this work investigates the closed- and open-state structure of ChR2. A movement of two helices is identified and found to be similar to changes reported for bacteriorhodopsin, despite ChR2's different transmembrane structure.

# ZUSAMMENFASSUNG

Die Fähigkeit, Licht wahrzunehmen ist für viele Organismen von zentraler Bedeutung, da Licht als Quelle für Informationen über Zeit und Richtung dienen kann. Entsprechend gibt es diverse Proteine, die regulierend in Verhaltens- und physiologische Prozesse eingreifen. Durch die große Bedeutung von Lichtrezeptoren ist ihre Erforschung von großem wissenschaftlichen Interesse.

Ein wichtiger Aspekt des Signalmechanismus von Photorezeptoren ist die Struktur ihres Signalzustandes. Elektron-Paramagnetische Resonanzspektroskopie (EPR), hat sich als Methode etabliert, Konformationen von Proteinen in Lösung zu untersuchen. In dieser Arbeit wird EPR zur Untersuchung von drei verschiedenen Proteinen, YF1, Cryptochrome-2 und Kanalrhodopsin-2, verwendet.

YF1 ist ein Beispiel für ein LOV-Protein, eine diversifizierte Gruppe von blaulichtempfindlichen Proteinen, die ein Flavin als Chromophor verwenden. Mit Hilfe von EPR Doppelresonanzmethoden wird ein Strukturmodell für den Lichtzustand sowie ein Modell für die Signalweiterleitung vorgeschlagen. Aminosäuren in der Umgebung des Flavins werden identifiziert, die die Kinetik des Photozyklus konsistent und über verschiedene LOV-Domänen hinweg, beeinflussen.

Cryptochrome sind mit Photolyasen eng verwandte Lichtrezeptoren. Wie LOV-Proteine enthalten sie ein Flavin als Chromophor. Die Photoreduktion mit anschließender Bildung eines Flavinradikals wurde gemeinhin als initialer Schritt der Ausbildung des Signalzustandes angenommen. Jüngere Experiment an Cryptochrom-Varianten, die funktionsfähig *in vivo* waren, jedoch *in vitro* keine Photoreduktion zeigten, stellen diese Hypothese jedoch in Frage. Um diesen Widerspruch aufzuheben, nutzt dieses Werk die Empfindlichkeit der EPR-Spektroskopie aus, die es ihr ermöglicht, das Flavinradikal auch *in vivo* nachzuweisen. es wird gezeigt, dass am Metabolismus beteiligte Moleküle wie ATP die Flavinreduktion stark fördern.

Kanalrhodopsine sind lichtgesteuerte Ionenkanäle aus der Familie der Rhodopsine, deren Erforschung durch klare Anwendungsmöglichkeiten in der Optogenetik an großer Bedeutung gewonnen hat. Die Struktur des offenen Zustandes von Kanalrhodopsin ist noch weitgehend unbekannt. Mit Hilfe von EPR-basierten Abstandsmessungen werden die Strukturen des offenen und geschlossenen Zustand in dieser Arbeit untersucht. Die Bewegung zweier Helizes beim Öffnen des Kanals kann gezeigt werden. Diese Bewegung entspricht den in Bakteriorhodopsin Nachgewiesenen, obwohl sich die Strukturen der beiden Proteine unterscheiden.

# CONTENTS

# LIST OF FIGURES

# List of Tables

## CHAPTER 1.

# INTRODUCTION

In many organisms, behavioural and physiological responses are regulated in a light-dependent manner, since light provides both temporal and spatial information.[1] It is therefore not surprising, that the identification and investigation of the biological photoreceptor proteins that translate light cues into physiological responses, have garnered persistent scientific interest.

Among the many different photoreceptor proteins known today, blue-light sensing proteins play a particularly important role, one, because their flavin chromophore is endogenous to all organisms and two, because many of its constituents, despite being involved in very different light-regulated processes, often share very similar structural motifs.[2–4]

Two such protein sub-groups are the focus of this work: Those of light, oxygen and voltage (LOV) domain proteins and cryptochromes.

LOV proteins[5,6] are remarkable as their blue-light sensing domain shows a particularly robust and well-conserved three-dimensional structure, while being coupled to a wide variety of effector domains.[2,7,8] One example of this adaptability is the artificial photoreceptor protein YF1, which consists of the LOV domain from *Bacillus subtilis* (*B. subtilis*) YtvA and the histidine kinase domain from *Bradyrhizobium japonicum* (*B. japonicum*) FixL.[9] Despite intense scientific focus, information about the structure of full-length LOV proteins as well the signalling mechanism that allows these domains to function when coupled to different effectors, is still lacking.

The second important group of photosensor flavoproteins investigated here are cryptochromes.[10] This group of proteins, structurally similar to photolyases,[11] is found throughout the biological kingdoms. They have been implicated in a wide variety of functions,[11,12] from the mediation of photomorphogenesis in plants, to the regulation of the circadian clock in mammals and flies.[11] Recently, evidence has mounted that they also form an integral part of magnetoreception in birds.[11] The photoreduction of their cofactor flavin adenine dinucleotide (FAD) by light-driven electron transfer along a series of three highly conserved tryptophane (trp) residues,[11,13] has long been considered as the biologically relevant primary light-sensing step. The transition from the oxidised to the radical form of the flavin is thought to induce conformational changes that lead to the signalling state.[14,15]

This mechanism of light-activation centred around the photoreduction of flavin has recently come into question, as *Arabidopsis thaliana* (*A. thaliana*) cryptochrome-2 (cry2) variants with a mutationally interrupted transfer pathway, that showed no photoreduction *in vitro*, were found to still be biologically active *in vivo*.[16]

Besides photoreception, ion transport across biological membranes is a second fundamental process in living organisms. These processes are governed by transporter proteins and channel proteins,[17,18] the former actively pumping, the latter controlling the free downhill movement of ions across the membrane. Channelrhodopsins (ChRs) are unique among ion channels, in that the opening of the channel is triggered by light instead of ligand binding, voltage or mechanical stress.[19] Since they are part of the molecular machinery that controls phototaxis in unicellular algae,[1] they represent an interesting intersection between ion channels and photoreceptors. ChRs belong to the well characterised family of microbial rhodopsins,[20] sharing with them the retinal chromophore as well as the initial step in the photoactivation process, the photo-induced isomerisation of the chromophore.[21] Which electrostatic and structural changes in ChR lead to the downstream opening of the channel, as well as the structure of the open state itself, is still unclear.

Changes in the tertiary structure of proteins can in general be favourably studied using electron paramagnetic resonance (EPR) in conjunction with site-directed spin labelling (SDSL). Flavoproteins additionally carry an intrinsic spin probe, as the radical states of the flavin chromophore are readily observed.[14,15,22,23] This work uses advanced EPR techniques to address the aforementioned questions, the light-state conformation of both ChRs and LOV proteins, the basis of different photocycle kinetics of LOV domains and the reason for contradicting *in vivo* and *in vitro* results in cryptochrome.

The ChR channelrhodopsin-2 (ChR2) from the green alga *Chlamydomonas reinhardtii* (*C. reinhardtii*), was used to investigate the conformations of the open and closed state by measuring and comparing point-to-point distances obtained using SDSL and electron-electron double resonance (ELDOR) spectroscopy, also called double electron-electron resonance (DEER).

In LOV proteins, two facets of the LOV photocycle were investigated based on the artificial protein YF1.[8] One, again using SDSL and ELDOR spectroscopy, the conformational changes caused by the photoreduction of the flavin, were investigated. Two, the structural basis for LOV domains' widely varying photocycle kinetics was investigated in a mutational study using electron-nuclear double resonance (ENDOR) spectroscopy.

In cryptochrome, the discrepancy between *in vitro* inactivity but *in vivo* functionality was investigated by examining the trp triad mutants in different environments using continuous-wave (cw) EPR and transient EPR (trEPR).

As is apparent from the debate over cryptochrome photoreduction, the potential differences between the behaviour of a protein *in vitro* and *in vivo* always need to be considered. Investigating these differences has been a special focus of this study, and *in vitro* experiments have, where possible, been performed *in vivo* as well.

## CHAPTER 2.

# FLAVINS AND FLAVOPROTEINS

Blue light has long been known to regulate various processes in plants, like phototropism, the induction of flowering, entrainment of circadian clocks or gene transcription.[24] The regulation of these responses involves a group of proteins that employ flavins as a blue-light sensing chromophore.,[2,3,25,26] comprising three major classes: BLUF (blue-light sensor using flavin adenine dinucleotide) proteins,[27] LOV proteins[28] (See Section 2.2) and cryptochromes[10] (Section 2.3).

## 2.1 THE FLAVIN COFACTOR

Flavins are ubiquitous in nature. Consisting of an isoalloxacine ring with varying sidechains, the most common variants are riboflavin (vitamin $B_{12}$), flavin mononucleotide (FMN) and FAD (Figure 2.1), with FAD and FMN being most commonly incorporated by proteins.

Flavins can exist in three different redox states, a fully oxidised quinone form, a fully reduced hydroquinone state and a radical semiquinone state. The hydro- and semiquinone form can additionally form two different physiologically relevant protonation states.[29,30] Thus, they are extremely versatile in biological systems, being able to undergo one- and two-electron transfer processes, act as electrophiles and nucleophiles and be involved in enzyme catalysis.[31,32] Additionally, they are employed as sensors for redox potential, partial oxygen pressure or light.[2,4,26] Their use as a blue-light sensor stems mainly from the ability of light to facilitate transitions between excited states and the different redox ground states. Photoreduction is employed by proteins in a variety of ways. In photolyases, photoreduction ensures that the flavin is driven to the fully reduced state,[33] which in these proteins is the catalytically active state needed for deoxyribonucleic acid (DNA) repair.[11,13] In cryptochromes and LOV proteins, flavins are photoreduced from the oxidised to the semiquinone state as part of the photocycle.

Some proteins, like cryptochromes, stabilise this radical state as part of their photocycle,[14,15] in others, like LOV domains, the radical state can be stabilised via mutation.[22,34] The presence of this intrinsic spin probe often makes EPR techniques especially suited for the investigation of flavonproteins.

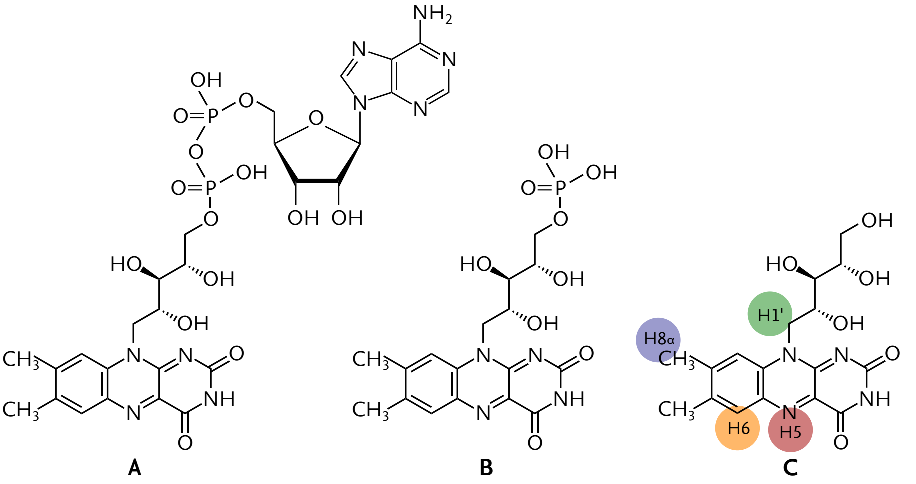

Figure 2.1. – **Different flavin variants.** (A) flavin adenine dinucleotide (FAD), (B) flavin mononucleotide (FMN) and (C) riboflavin all share the same isoalloxacine ring with different sidechains. In the flavin radical state, the protons attached at N5 (only in the neutral radical state) (red), C6 (yellow), C8α (blue) and C1' (green) can be observed using EPR (See Fig. 6.22 on p. 100).

## 2.2 LOV proteins

LOV domains are a blue-light sensing subgroup of the Per-ARNT-Sim (PAS) domain familiy. Sensor proteins utilising PAS domains can be found in all biological kingdoms,[35] where they regulate processes ranging from phototropism to the gating of ion channels.[5,36] They are small sensor modules building a compact α/β structure, with a central, antiparallel, five-stranded β-sheet flanked by α-helices.[37] PAS domains are highly modular: Different PAS domains detect a wide variety of different signals, like chemical ligand binding, light absorption or redox potential, and proteins will often incorporate multiple PAS domains, or PAS domains in tandem with other types of signalling domains.[38] The range of effector domains regulated by PAS domains is equally varied, including kinases, transcription factors or phosphodiesterases. In most cases, PAS domains covalently bind to their effector modules via their C-terminus, although a few cases are known where a PAS domain attaches to an effector domain via its N-terminus.[39]

All this points to a signalling mechanism that is simple, not reliant on specific tertiary structure contacts and easy to adapt to different quaternary structures.

The group of light-sensitive PAS domains, called light, oxygen and voltage or LOV domains, themselves also occur in a broad range of organisms and the associated sensor proteins regulate diverse processes. They are found throughout Archae, Bacteria, Protists, Fungi and plants and have been shown to regulate e.g. pho-

FIGURE 2.2. – **Structure of a light, oxygen and voltage domain, showing the typical PAS fold, an antiparallel β -sheet (blue) flanked on either side by helices (red).** A FMN chromophore (yellow) is situated in a cavity formed by the β-sheet and an α-helix. The structure shown is YF1 (pdb: 4GCZ[9]).

totropism, chloroplast movement, stress responses and circadian rhythms.[2,4,26,40] While they differ strongly in composition and structure, they all contain a photosensory LOV domain as a defining feature.

LOV domains exhibit the typical PAS fold.[41] They bind FMN in a cavity formed by the antiparallel β-sheet on one side and an arrangement of α-helices on the other and are thus sensitive to blue light (Fig. 2.2).

### 2.2.1 THE LOV PHOTOCYCLE

The dark-adapted state of LOV domains, $\mathrm{LOV}_{447}$ (Figure 2.3A), is characterised by the typical ultraviolet/visual (UV/vis) spectrum of fully oxidised flavin, with dominant absorption at 447 nm. The photocycle of LOV involves the reversible formation of a covalent bond between the FMN C4a atom and a strictly conserved nearby cysteine (C450 in the phototropin-1 LOV2 domain from *Avena sativa* (AsLOV2), C62 in YF1),[42] the so-called Cysteinyl-C4a or FMN-Cys photoadduct. This state, $\mathrm{LOV}_{390}$ (Fig. 2.3C), is readily distinguished from the dark-adapted state by its significantly blue-shifted absorption spectrum.

Photoexcitation of the oxidised flavin leads to a red-shifted flavin triplet state $\mathrm{LOV}_{660}$ (Fig. 2.3B) within nanoseconds. The flavin is then protonated at N5 from the conserved cysteine, forming a short-lived radical pair FMNH·–·S-Cys[42–44] and ultimately the photoadduct. Resulting changes in the hydrogen bonding network propagate through the LOV domain[26] and ultimately affect the output modules,[2,4,26] though the specific conformational changes remain unclear.

The return to the dark-adapted state involves the breaking of the covalent bond,

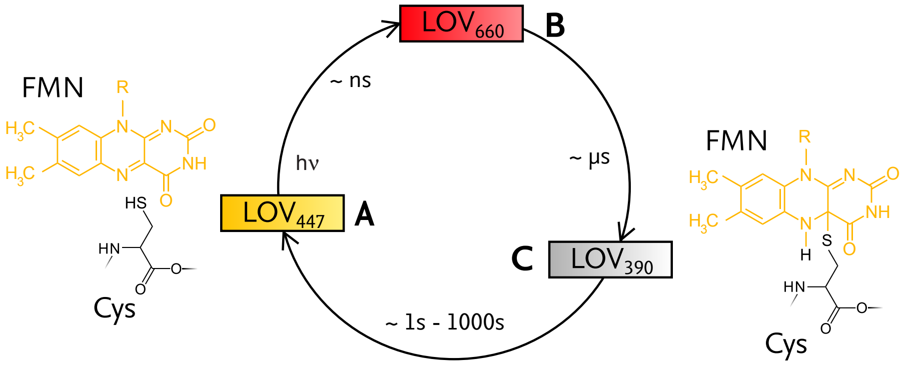

Figure 2.3. – **Simplified LOV photocycle.** In the dark state $LOV_{447}$ (A), FMN and a conserved cysteine (C62 in YF1) are not covalently bound, the cysteine's sulphur is protonated. Photoexcitation yields a transient flavin triplet state $LOV_{660}$ (B). Rapid reduction of the flavin by the conserved cysteine ultimately leads to the formation of the Cysteinyl-C4a photoadduct $LOV_{390}$ (C). The chemical structures of FMN and the cysteine in $LOV_{447}$ and $LOV_{390}$ are shown on the left and right, respectively.

deprotonation at N5 and reprotonation of the cysteine. The kinetics of this thermally driven process appear to be strongly dependent on the precise conformation of the flavin moiety, which can either hinder or promote the breaking of the bond or N5 reprotonation.[45] As a result, the observed dark-state recovery rates vary by four orders of magnitude, from seconds to several hours.[3,46–49]

### 2.2.2 YF1, A BLUE-LIGHT SENSITIVE SENSOR HISTIDINE KINASE

The elucidation of the signal transduction mechanism of LOV domains, which allows them to be utilised in a broad spectrum of structurally different proteins, has long been hampered by the lack of structural information for full-length proteins. Here, a recently published crystal structure of YF1[9] promises new insights into the mechanisms by which LOV domains interact with their effector domain partners.

YF1 is a "designer protein" constructed from a sensor histidine kinase (SHK) with a bacterial LOV domain replacing its natural sensor domain,[8] *B. japonicum* FixL is originally an oxygen-sensitive SHK with a Heme-binding PAS domain. In YF1, the oxygen-sensing PAS domain has been replaced with the blue-light sensitive LOV domain from *B. subtilis* YtvA, yielding a new protein that is now a light-regulated SHK. The resulting structure (Figure 2.4) is that of a homodimer, with two YtvA LOV domains (Figure 2.4, green) covalently attached to two FixL kinase domains (Figure 2.4, blue) via a coiled-coil linker region (Figure 2.4, gray). Interestingly, the

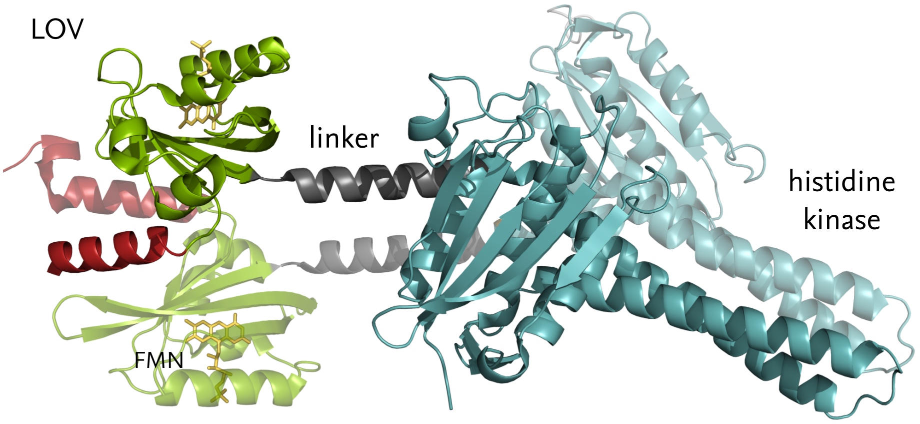

FIGURE 2.4. – **Crystal structure of YF1.**[8,9] YF1 is a homodimer, each monomer consisting of a LOV domain (green) connected to a kinase effector domain (blue) via a coiled-coil linker helix (gray). Short N-terminal helices (red) are folded in between the LOV–LOV dimer, separating the β-sheets.

LOV domains do not dimerise directly via their β-sheets. Instead, two 22 amino acid N-terminal helices are folded in between the LOV domains, pushing them apart. This general quaternary structure has also been proposed for wildtype (wt) YtvA.[50–52]

With the available crystal structure,[9] as well as an efficient functional assay,[53] YF1 is an ideal basis for the investigation of various aspects of the PAS signalling mechanism. Chapter 6.2 will shed some light on structural changes involved in the transition to the signalling state. Chapter 6.3 will investigate the structural basis of the LOV domains' highly variable dark state recovery kinetics.

## 2.3 CRYPTOCHROMES

Cryptochromes, together with CPD-photolyases and (6-4)-photolyases, form the photolyase/cryptochrome superfamily, a group of photoactive proteins that is found throughout the biological kingdoms. While photolyases are found in most procaryotes and eucaryotes, cryptochromes are found mainly in higher plants and most animals. Two major classes of cryptochromes exist, the first consisting of the classic cryptochromes cryptochrome-1 (cry1), cry2 and homologues in plants and two types found in insects and mammals, the second comprising cry-DASH cryptochromes.

The plant cryptochromes fulfil a variety of signalling roles involved in plant growth and development, among them the inhibition of stem grows of germin-

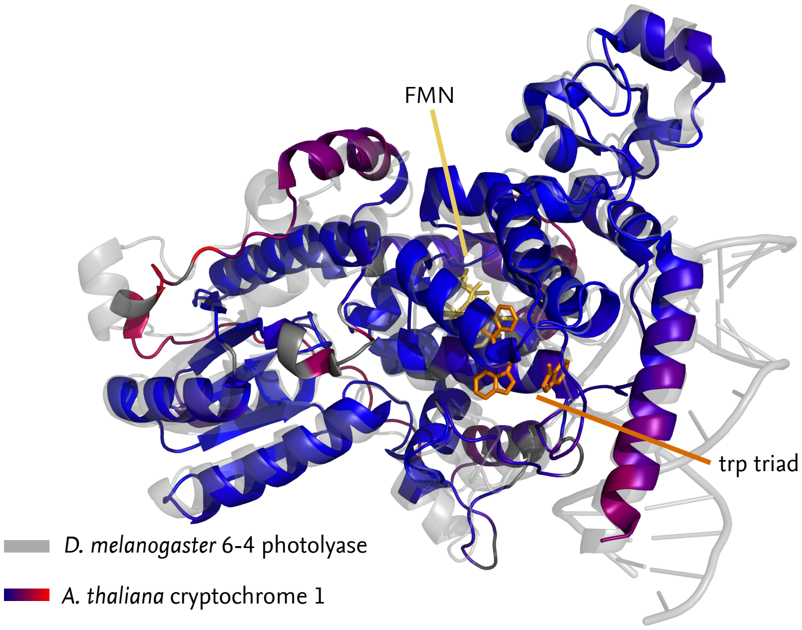

FIGURE 2.5. – **Structure of *A. thaliana* cryptochrome-1 (coloured) (pdb: 1U3C[60]) compared to that of *D. melanogaster* (6-4) photolyase (gray) (pdb: 3CVU[61]).** The structure of cry1 is colour-coded by RMSD from photolyase, with red indicating higher and blue lower deviation. The FAD cofactor is shown in yellow, the trp triad in orange.

ating seedlings (hypocotyl elongation),[10,54] the photoperiodic initiation of flowering[55,56] and the synchronisation of the circadian clock to a 24 h day.[12,57] Further processes influenced by plant cryptochromes are hormone signalling, defence and stress responses as well as metabolism.[57] Interestingly, most of these responses can be traced to effects on nuclear gene transcription or interaction with the proteasome, and cry1 has been shown to be involved in blue-light dependent gene expression[58,59] even though it is itself not capable of binding DNA.

### 2.3.1 COMPARISON TO PHOTOLYASES

Cryptochromes show significant sequence and structural homology in their photoreactive domain, with both classes sharing the same secondary structure (Figure 2.5) and both binding FAD as a chromophore. In fact, the class of cry-DASH cryptochromes is more closely related to photolyases than to other cryptochromes. Cryptochromes share the active site features of photolyases,[60] even though they are either incapable of repairing DNA (classic cryptochromes) or show impaired DNA repair function (cry-DASH).[62] While both cryptochromes and photolyases undergo photoreduction of the flavin cofactor,[11,33] in photolyases the flavin rests normally in the fully reduced state needed for DNA repair,[13] and photoreduction is employed to return radical states to this hydroquinone form,[11] whereas classical cryptochromes incorporate the flavin in the oxidised form. Cry-DASH proteins, again appearing as an intermediate between photolyases and cryptochromes can photoreduce their FAD cofactor into the fully reduced form. In light of the similarities between the two classes, cryptochromes are defined as proteins similar to photolyases, that have partially or fully lost DNA repair capabilities and instead gained signalling functions.[11]

Unlike photolyases, most cryptochromes possess an additional C-terminal extension (CCT) that varies in size from 80 to several 100 amino acids that is both poorly conserved and poorly structured in the absence of putative interaction partners,[63] but nonetheless essential for activity.[12,57] For cry1 and cry2, it has been demonstrated that the CCT interacts with COP1, a protein involved in photomorphogenesis regulation via the proteasome.[64]

### 2.3.2 PHOTOREDUCTION AND THE SIGNALLING STATE

As mentioned, the resting state of the FAD chromophore in plant cryptochromes is the oxidised form.[14,15,65] Illumination, both *in vitro* and *in vivo*, accumulates the neutral flavin radical state.[14,15] Cryptochromes contain a strongly conserved series of three tryptophane residues, termed the trp triad,[13] which connects the FAD chromophore with the protein surface (Figure 2.6). Upon photoexcitation, the flavin abstracts an electron from the nearest trp residue (W397 in cry2). A cascading electron transfer process along the triad (from W374 to W397 followed by a transfer from W321 to W374 in cry2) and subsequent re-reduction of the terminal trp (W321 in cry2) by the solvent leaves a cryptochrome containing FAD in the neutral flavin radical state,[11,13] which, being unstable, reverts back to the fully oxidised form over the course of minutes. While the trp triad is believed to be the primary electron transfer pathway, alternative pathways have been reported.[66]

The proposed activation process for cryptochrome is that in the dark, the C-terminal region is folded in a way that prevents substrate binding. Light absorption of the flavin at the N-terminal domain triggers conformational changes that then make the receptor accessible to downstream signalling partners.[67,68] Photoreduction of the flavin and formation of the neutral radical state is believed to be the initial step in the formation of the cryptochrome signalling state.[14,15] Structural changes triggered by the formation of an unstable but long-lived neutral flavin radical would provide a simple mechanism for signal transduction, as such light-induced conformational changes form the basis of photoreception in other proteins, e.g. rhodopsins and LOV proteins.

Photoreduction as the initial step in the activation mechanism of cryptochromes

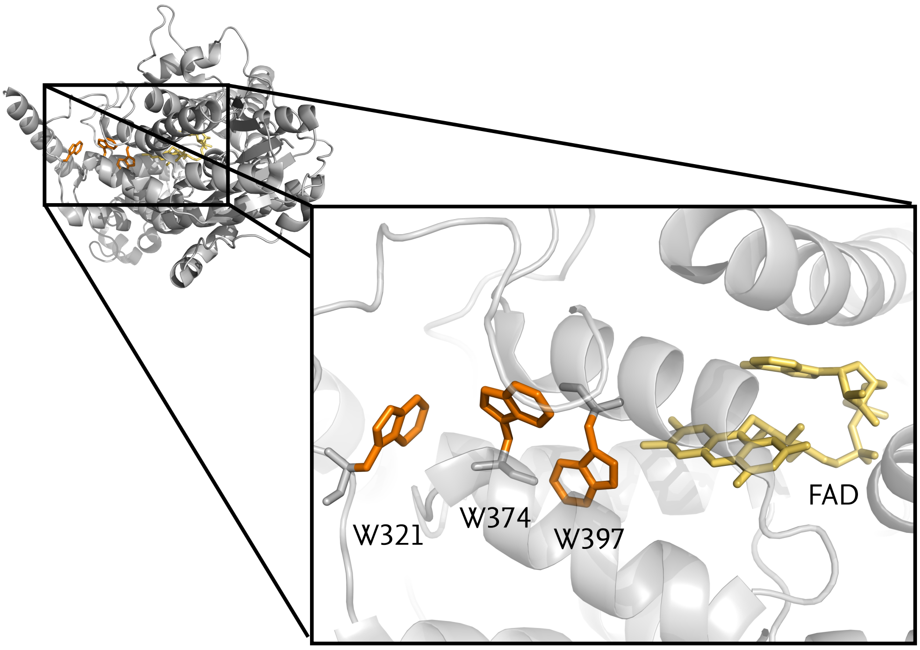

FIGURE 2.6. – **The FAD cofactor and the conserved trp triad in cryptochrome (pdb: 1U3C[60]).** Upon photoexcitation, the FAD abstracts an electron from nearby tryptophane 397. Cascading electron transfer processes along the triad yield a spin-correlated radical pair on the flavin and terminal tryptophane 321, which is then re-reduced from the solvent.

is supported by a number of lines of evidence. (1) The trp triad is highly conserved in most known plant and animal cryptochromes and functional during photoreduction of isolated cry1 and cry2.[14,15,69] (2) As mentioned above, in *in vivo* cryptochromes the resting state of the flavin is the oxidised form,[14,15,65,70] which can be photorecuded. (3) Photoreduction and radical accumulation occur in living insect cells expressing cry1 and cry2.[14,15] (4) Illumination of plants with with e.g. green light, which diminishes the amount of flavin radical present, result in diminished cryptochrome activity as well.[14,15] (5) Mutations that do not undergo photoreduction, also show reduced biological function in plants.[69] (6) The lifetime of the cryptochrome signalling state *in vivo* matches well the lifetime of the flavin radical state.[71]

Nevertheless, recent results obtained from cry2 and *Drosophila melanogaster* cryptochrome (Dm-cry), where mutant proteins that did not undergo photoreduction *in vitro* were nonetheless found active *in vivo*[16,72–75] have cast some doubt on this interpretation. This apparent contradiction will be addressed in Chapter 6.4.

## CHAPTER 3.

# CHANNELRHODOPSIN-2, A LIGHT GATED ION CHANNEL

The transport of ions through biological membranes is a fundamental process in living organisms. The proteins responsible for this transport can be divided into two groups, transporters or pumps and channels, the key difference being that the transport is active in the former and passive in the latter.[17,18] Ion channels in particular are involved in the conductance of electrical signals and other signalling processes by regulating the free downhill movement along electric potential gradients of ions across a membrane. They generally contain a water-filled pore, along which ions can pass through the normally impenetrable cell membrane and which is transiently opened and closed (gated) by the ion channel in response to external stimuli.[76]

Different groups of ion channels can be identified based on the type of trigger they respond to, commonly a molecule binding to the protein (ligand-gated ion channels), a change in the electric potential across the membrane (voltage gated channels) or a change in pressure (mechanosensitive channels).[77]

The only currently known ion channels in nature that are triggered by light (light-gated) are channelrhodopsins.[78] While the first members of this group, channelrhodopsin-1 (ChR1) and ChR2, were identified in the eye spot of the green alga *C. reinhardtii*,[19,78] there are currently many additional ChRs with differing light sensitivities, ion selectivities and kinetics known in other unicellular algae.[79–82] Of the known ChRs, ChR2 is currently the most studied.

ChR2 is a non-selective cation channel, that conducts protons and a variety of monovalent and divalent cations,[19] but no anions.[78] Permeability for monovalent cations is smaller by at least six orders of magnitude than for protons,[83,84] and divalent alkaline cations are conducted worse than monovalent alkaline cations by one to two orders of magnitude,[85] although the fraction of the total ion current not due to protons remains significant at physiological concentrations and pH values.[86] Additionally, ChR2 also shows proton pumping driven by light, with an efficiency of 0.3 ± 0.1 protons per photocycle.[87,88]

In *C. reinhardtii*, both ChR1 and ChR2 act as photosensors and are incorporated into the signalling mechanism that controls phototaxis, the process directing the algae towards or away from light to optimise photosynthesis.[1] However, the discovery of a light-gated ion channel has significant implications for optogenetics, since such a channel offers the possibility to remotely control cell potentials or ion transport processes by light, including control of nerve cell activity. This makes this class of proteins particularly interesting for neurophysiology.[89] It is therefore unsurprising that intense research efforts have been directed at describing and understanding the structure and function of this class of proteins.

## 3.1 The structure of channelrhodopsin-2

ChR2s comprises a transmembrane (TM) domain bound to a soluble cytoplasmic domain, consisting of about 400 amino acids, the function of which remains unknown. Since a truncated construct (residues 1–315) lacking this soluble domain showed nearly identical ion conduction behaviour as the wt,[19] the channel function is fully contained within the TM motif, to the extent that the truncated construct has been used in research in lieu of the actual wt ever since.

The TM part of ChR2 shows significant sequence homology with the family of microbial rhodopsins,[20] which consist of a fold of seven TM helices embedding retinal as a chromophore, which is covalently bound to a conserved lysine, forming a protonated Schiff base (SB).[21] The photocyle in bacteriorhodopsin (BR) and other microbial rhodopsins proceeds from the initial photo-induced trans-to-cis isomerisation of the retinal chromophore around the C13=C14 bond. In ChR2 this initial step ultimately leads to the opening of the channel, even though the precise electrostatic and mechanistic steps are currently not known.

A projection map of two-dimensional crystals[91] as well as a recent crystal structure of a ChR1-ChR2 hybrid (C1C2) formed from helices A–E of ChR1 and helices F–G of ChR2[90] confirm the 7-TM structural motif as well as demonstrate that ChRs form dimers, interacting via helices C and D (Figure 3.1A). The structure, as revealed by C1C2, helices C–G especially, is typical for microbial rhodopsins. Helices A and B, however, are tilted outwards by 3–4 Å relative to the structure of BR, creating in a cavity that forms an electronegative pore towards the extracellular medium (Figure 3.1B, surface of the pore shown in gray). This pore was concluded to form the outer part of the cation pathway.[90]

## 3.2 The ChR2 photocycle

In the dark state of ChR2, the retinal absorbs at 470 nm (Figure 3.2A). Photoexcitation of the retinal leads, via an electronically excited state that decays with a 1/e-

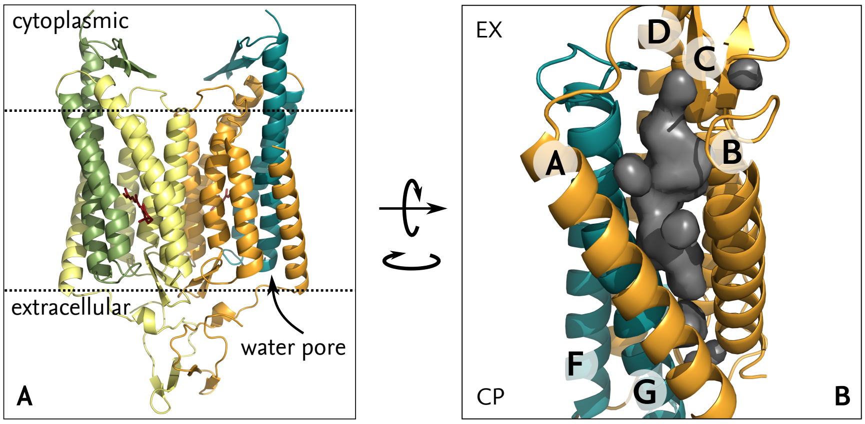

Figure 3.1. – **Crystal structure of the ChR1-ChR2 hybrid[90] (pdb: 3UG9).** (A) Helices A–E from channelrhodopsin-1 (yellow/orange) are linked to helices F–G from channelrhodopsin-2 (green/blue). Together, they form the typical 7-TM structural motif of microbial rhodopsins. (B) Helices A and B are tilted compared to the BR structure, forming an electronegative pore (gray).

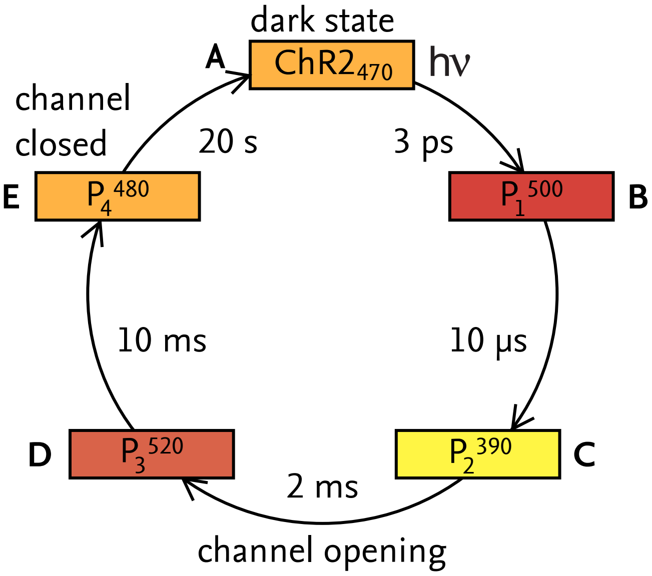

Figure 3.2. – **Simplified photocycle of channelrhodopsin-2 without side-reactions.** From the dark state (A), the retinal is photoexcited and undergoes isomerisation within picoseconds ($P_1^{500}$)(B). Within microseconds, the Schiff base is deprotonated, yielding a blue-shifted intermediate ($P_2^{390}$)(C). Reprotonation over 2 ms results again in a red shift of the absorption ($P_3^{520}$)(D). Between these two intermediates the channel opens. The channel then closes again and transforms into an additional intermediate similar to the dark state, but inactive ($P_4^{480}$)(D).

time of $\tau = 400$ fs, to a vibrationally excited, redshifted electronic ground state.[92,93] The next step is the decay, with a rate of 3 ps, to a redshifted intermediate that is characteristic for microbial rhodopsins, absorbs maximally at 510 nm and likely corresponds to the 13-cis retinal conformation.[92]

The initial steps of the photocycle were elucidated using optical pump-probe techniques on a timescale of femtoseconds to hundreds of picoseconds. The later stages, including $P_1^{500}$, where investigated using flash photolysis, on a timescale of 40 ns to 50 s, leading to a several nanosecond gap in observation. The earliest intermediate identified using flash photolysis, formed in under 40 ns is again redshifted with an absorption maximum at 500 nm and thus termed $P_1^{500}$.[94] Since the last state observed by pump-probe experiments appears to differ structurally from the first observed by flash photolysis,[92,95] it is likely that there exist several slightly different $P_1^{500}$ states with slightly different retinal conformations and/or moieties (Figure 3.2B).

Within 10 µs, the Schiff base deprotonates,[94,96] D253 being the likely proton acceptor,[90,95] yielding a new intermediate, $P_2^{390}$, absorbing at 390 nm (Figure 3.2C).

$P_2^{390}$ decays, and the Schiff based reprotonates with a proton donated from D156,[95] with a half-life of 2 ms, yielding a red-shifted intermediate with an absorption at 520 nm, $P_3^{520}$. (Figure 3.2D). $P_3^{520}$ decays with a time constant of $\tau = 10$ ms, as does the conducting state of ChR2. Thus, the decay of $P_3^{520}$ corresponds to the closing of the channel. The opening of the channel at 200 µs, however, does not coincide with either Schiff base deprotonation or $P_3^{520}$ formation and thus likely happens at a substate that is currently inaccessible to spectroscopy. Studies on variants C156A and C128T found that both variants show long-lived open states with similar photocurrents even though D156A is present primarily as intermediate $P_2^{390}$ and C128T mostly as $P_3^{520}$, indicating that the open states consist of substates from both $P_2^{390}$ and $P_3^{520}$.[97,98]

While $P_3^{520}$ decays fairly rapidly on a millisecond timescale, the dark state is only recovered with a time constant of 20 s via an additional state $P_4^{480}$, similar to the ground state (Fig. 3.2E). Time-resolved fourier-transform infrared (FTIR) spectroscopy suggests that $P_4^{480}$ is not part of a linear photocycle, but rather part of a branch transited by a fraction of ChR2 molecules.

The detailed internal mechanistic and electrostatic steps involved in the opening and closing of the channel have been, and still are, extensively studied. A more detailed treatment can be found e.g. in a comprehensive review by Lórenz-Fonfría and Heberle.[99] Knowledge of the structural changes in the tertiary structure associated with the different stages of the photocycle, well understood in other rhodopsins,[100–102] is still lacking for ChR2. Some progress towards unravelling these structural changes will be presented in Chapter 6.1.

## CHAPTER 4.

# FUNDAMENTALS OF EPR

This chapter provides the fundamental theory of EPR with the focus on those interactions of particular relevance to this work. The principles behind basic continuous-wave (cw) and pulsed EPR experiments are described as well. A more detailed description of EPR theory can be found in several comprehensive text books, including those by Jeschke and Schweiger,[103] Carrington and McLachlan,[104] or Weil, Wertz and Bolton.[105]

Paramagnetic species possess a permanent dipole moment induced by a combination of their spin and angular momentum. By introducing the paramagnetic species into an external magnetic field, the magnetic moment is quantized along the magnetic field's axis,[106] giving rise to an energy splitting called the Zeeman effect.[107]

EPR spectroscopy, first used as a spectroscopic method by ZAVOISKY in 1944,[108,109] seeks to investigate these different energy levels by driving transitions between different states using resonant microwave irradiation according to the resonance condition

$$h\nu = g_{\mathrm{e}}\mu_{\mathrm{B}}\boldsymbol{B}_0, \tag{4.1}$$

where $\nu$ is the microwave frequency, $\boldsymbol{B}_0$ is the external field, $g_{\mathrm{e}} = 2.002319$[110] is the free electron $g$-factor and $\mu_{\mathrm{B}} = \frac{e\hbar}{2m_{\mathrm{e}}}$ is the Bohr magneton.

## 4.1 THE SPIN HAMILTONIAN

Since magnetic resonance spectroscopy methods only drive transitions between different spin states, contributions to the full Hamiltonian of the system that have no spin-dependent components can be disregarded when discussing magnetic resonance. The resulting, reduced Hamiltonian is called the *spin Hamiltonian* $\hat{\boldsymbol{H}}$

$$\hat{\boldsymbol{H}} = \hat{\boldsymbol{H}}_{\mathrm{ez}} + \hat{\boldsymbol{H}}_{\mathrm{nz}} + \hat{\boldsymbol{H}}_{\mathrm{hf}} + \hat{\boldsymbol{H}}_{\mathrm{ee}} + \hat{\boldsymbol{H}}_{\mathrm{zero}} + \hat{\boldsymbol{H}}_{\mathrm{quad}}. \tag{4.2}$$

the individual terms of which will be discussed below.

### 4.1.1 ZEEMAN INTERACTIONS $\hat{\boldsymbol{H}}_{\mathrm{EZ}}$ AND $\hat{\boldsymbol{H}}_{\mathrm{NZ}}$

Just like the classical magnetic dipole moment induced by the angular momentum of charged particles, the spin angular momentum couples linearly to an external magnetic field $\boldsymbol{B}_0$. The magnetic moment of electron and nuclear spins are given by

$$\hat{\boldsymbol{\mu}}_{\mathrm{E}} = -\mu_{\mathrm{B}}\, g_{\mathrm{e}}\, \hat{\boldsymbol{S}} \tag{4.3}$$

$$\hat{\boldsymbol{\mu}}_{\mathrm{N}} = -\mu_{\mathrm{N}}\, g_{\mathrm{N}}\, \hat{\boldsymbol{I}}\ , \tag{4.4}$$

where $\hat{\boldsymbol{S}}$ and $\hat{\boldsymbol{I}}$ are the spin operators for the electron and nuclear spin, respectively, $\mu_{\mathrm{B}}$ and $\mu_{\mathrm{N}}$ are the Bohr and Nuclear magneton and $g_{\mathrm{e}}$ and $g_{\mathrm{N}}$ are the g-factors for the electron and the nucleus. The interaction between these magnetic moments and an external field is called *Zeeman interaction* and is described by the following Hamiltonians

$$\hat{\boldsymbol{H}}_{\mathrm{ez}} = -\hat{\boldsymbol{\mu}}_{\mathrm{E}}\boldsymbol{B}_0 = \mu_{\mathrm{B}}\boldsymbol{B}_0\underline{\underline{\boldsymbol{g}}}\hat{\boldsymbol{S}}_{\mathrm{z}} \tag{4.5}$$

$$\hat{\boldsymbol{H}}_{\mathrm{nz}} = -\hat{\boldsymbol{\mu}}_{\mathrm{K}}\boldsymbol{B}_0 = \mu_{\mathrm{N}}\boldsymbol{B}_0\underline{\underline{\boldsymbol{g}}}_{\boldsymbol{N}}\hat{\boldsymbol{I}}_{\mathrm{z}}. \tag{4.6}$$

For most paramagnetic species, spin-orbit coupling between the spin angular momentum $\hat{\boldsymbol{S}}$ and the orbit angular momentum $\hat{\boldsymbol{L}}$ is non-negligible, causing the strength of the interaction to be dependent on the orientation of $\hat{\boldsymbol{S}}$ and $\boldsymbol{B}_0$. This is described by introducing an orientation-dependent $g$-matrix $\underline{\underline{\boldsymbol{g}}}$ in place of the g-factors $g_{\mathrm{e}}$ and $g_{\mathrm{N}}$. Determining and analysing this empiric coupling tensor is one of the central objects of EPR spectroscopy. Nuclear spins in principle also exhibit spin-orbit coupling according to the atom shell model. While relevant in high resolution experiments like high-frequency nuclear magnetic resonance (NMR), in EPR applications the resulting anisotropy is small when compared to the linewidth of nuclear transitions. Thus, the interaction can be treated as effectively isotropic and the nuclear g-factor a scalar specific to each nucleus. Due to the difference in mass between an electron and a nucleus, the nuclear Zeeman interaction is by orders of magnitudes smaller[A] than the electron Zeeman interaction.

For systems with more than one spin, spin-spin interaction both between a nuclear and an electron spin and between two electron spins also contribute to the total spin Hamiltonian.

---

[A] $\hat{\boldsymbol{H}}_{\mathrm{NZ}} = 0.00152\hat{\boldsymbol{H}}_{\mathrm{EZ}}$ for protons.

### 4.1.2 HYPERFINE INTERACTION $\hat{\boldsymbol{H}}_{\text{HF}}$

The hyperfine interaction between an electron and a nuclear spin is expressed by

$$\hat{\boldsymbol{H}}_{\text{hf}} = \sum_{k} \hat{\boldsymbol{S}}\boldsymbol{A}\hat{\boldsymbol{I}}, \tag{4.7}$$

where $k$ indexes the nucleus under consideration. This interaction can be split into two parts, the singular part $\hat{\boldsymbol{H}}_{\text{HF,iso}}$ and the non-singular part $\hat{\boldsymbol{H}}_{\text{HF,dip}}$ of the dipole-dipole interaction between electron and nucleus. The isotropic singular, or Fermi contact, part, arises from the non-zero probability of finding the electron at the coordinate of the nucleus.

$$\hat{\boldsymbol{H}}_{\text{hf}} = \hat{\boldsymbol{H}}_{\text{hf,iso}} + \hat{\boldsymbol{H}}_{\text{hf,aniso}}. \tag{4.8}$$

The Fermi contact interaction is given by

$$\begin{aligned} \hat{\boldsymbol{H}}_{\text{hf,iso}} &= a_{\text{hf,iso}}\hat{\boldsymbol{S}}\hat{\boldsymbol{I}} \\ &= \rho_{\text{k}}\frac{2}{3}\mu_0 g_{\text{e}}\mu_B g_n \mu_{\text{N}}|\Phi_0(0)|^2\hat{\boldsymbol{S}}\hat{\boldsymbol{I}}, \end{aligned} \tag{4.9}$$

where $\rho_{\text{k}}$ is the total spin density at nucleus $k$ and $|\Phi_0(0)|^2$ is the probability of finding the electron at the nuclear coordinates. Since the latter is zero for orbitals other than s-orbitals, those do not contribute to the isotropic part of the interaction. In the case of protons, the magnetic momentum of the electron is in this case fully described by the free electron g-factor $\text{g}_{\text{e}}$, since there is no spin-orbit coupling in proton s-orbitals. This is not necessarily the case for other nuclei, since their eigenfunctions are linear combinations of multiple $^1$H eigenfunctions and could as such exhibit spin-orbit coupling.

Due to the non-symmetric geometry of p-, d-, f-orbitals, unpaired electrons in these orbitals show dipolar coupling to the nucleus and are therefore responsible for the anisotropic, dipole-dipole contribution to the hyperfine interaction

$$\begin{aligned} \hat{\boldsymbol{H}}_{\text{hf,aniso}} &= \hat{\boldsymbol{S}}\boldsymbol{A}_{\text{hf,dip}}\hat{\boldsymbol{I}} \\ &= \frac{\mu_0}{4\pi} g_{\text{e}}\mu_{\text{B}} g_{\text{N}}\mu_{\text{N}} \left( \frac{3(\hat{\boldsymbol{S}}\boldsymbol{r})(\boldsymbol{r}\hat{\boldsymbol{I}})}{r^5} - \frac{\hat{\boldsymbol{S}}\hat{\boldsymbol{I}}}{r^3} \right), \end{aligned} \tag{4.10}$$

where $\boldsymbol{r}$ is the connecting vector between the electron and nuclear spins. Even though for protons themselves, most of the spin density is usually located in s orbitals, proton hyperfine couplings in molecules still regularly show hyperfine anisotropy due to dipole-dipole interaction with electron spin density on other nuclei closeby.

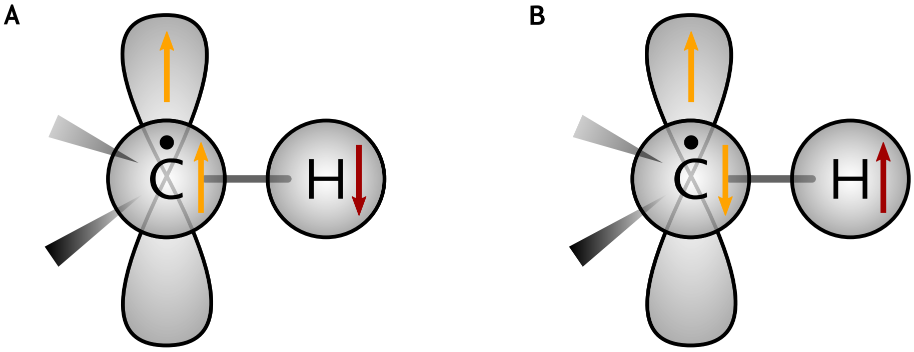

FIGURE 4.1. – **Spin polarisation on protons directly adjacent to carbon radicals.** Due to the spin density in the carbon atom's $p_z$-orbital, the spin orientation in (A) is slightly more favourable than that in (B).

### SPIN-POLARISATION IN PROTONS BOUND TO CARBON RADICALS

The interactions discussed so far can be understood in a single electron system. When discussing electrons bound to molecules, further contributions arising from correlations between multiple electrons become relevant. Consider the case of a C-H-bond, with the unpaired electron having significant probability of occupying the carbon atom's $p_z$-orbital (Figure 4.1).

In an external magnetic field, the α-state will be the preferred one for that electron. Electrons in other orbitals of the carbon atom will therefore also slightly prefer the α-state since electrons in the same spin state tend to have less electrostatic repulsion. In particular, this is also true for the electron in the carbon $sp_2$-orbital shared with the proton. As the Pauli principle requires that two electrons sharing the same orbital must have anti-parallel spin, the electron bound to the proton will slightly prefer the β-state (Figure 4.1A) over the α-state (Figure 4.1B). This corresponds to an isotropic hyperfine coupling of the proton. This effect, termed spin polarization, is found in σ-radicals, where the spin density is confined to a single $p_z$-orbital, and in, more importantly for this work, π-radicals, where the electron spin density is found in a delocalised π-system. The isotropic hyperfine coupling of such a proton in a delocalised π-system can be calculated via the McConnell relation[111]

$$a_{\text{iso}} = Q_{\text{H}}\rho_{\pi}, \tag{4.11}$$

where $Q_{\text{H}}$ is an empirical parameter with a value of ≈2.5 mT and $\rho_\pi$ is the electron density in the π-system at the coordinates of the carbon atom to which the proton is bound.

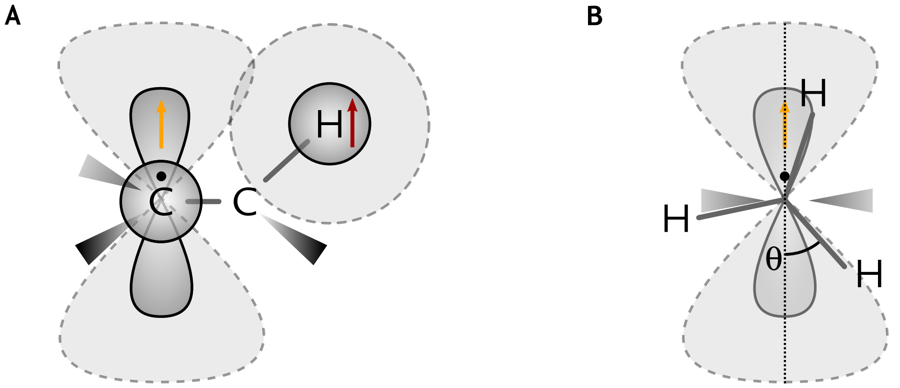

FIGURE 4.2. – **Hyperconjugation of next-neighbour (α-) protons**. The overlap between the proton's s- and the carbon atom's $p_z$-orbital (A) induces an isotropic hyperfine coupling, dependent on the angle between the $C_\alpha$-H-bond and the $p_z$-orbital (B).

### HYPERCONJUGATION IN $\alpha$-PROTONS

Protons that aren't directly bound to the carbon radical, but to an adjacent (α-) carbon, e.g. protons in a methyl group bound to a carbon with unpaired electron in $p_z$ or delocalised π-orbitals, also show pronounced hyperfine couplings The cause in this case is not spin-polarisation but delocalisation of the unpaired electron from the $p_z$- (π-) orbital to the proton's s-orbital due to the significant overlap these orbitals can have (Figure 4.2). The strength of the resulting hyperfine coupling is a function of the dihedral angle θ between the $p_z$-orbitals' axis and the $C_\alpha$-H-bond[112]

$$a_{\text{iso}} = a_1 + a_2 \cos^2(\theta)\,. \tag{4.12}$$

Specifically for methyl groups, the three protons at angles of 120° relative to each other give rise to three different couplings given by

$$a_{\text{iso}} = a_1 + a_2 \cos^2\left(\theta + \frac{2\pi}{3}k\right), \quad k = 0, 1, 2, \tag{4.13}$$

If the C-C-bond can freely rotate, as is usually the case for methyl groups, an average hyperfine coupling is observed

$$\begin{aligned} a_{\text{iso}} &= a_1 + a_2\overline{\cos^2(\theta)} \\ &= a_1 + \frac{1}{2}a_2. \end{aligned} \tag{4.14}$$

with triple intensity.

For typical directly adjacent and nearest-neighbour (α-) protons bound to a cofactor-radical in a protein, the isotropic component of the hyperfine coupling dominates the anisotropic. In a sample in frozen solution, all orientations of the sample are present simultaneously. A typical resulting hyperfine spectrum of a single proton is shown in Fig. 4.3A.

### 4.1.3 WEAK ELECTRON-ELECTRON INTERACTION $\hat{\boldsymbol{H}}_{\mathrm{EE}}$

The interaction between two weakly coupled[B] electron spins can be described in very similar terms as the hyperfine couplings between an electron and a nucleus discussed above, with the isotropic Heisenberg exchange interaction

$$\hat{\boldsymbol{H}}_{\mathrm{ee,iso}} = -2J\hat{\boldsymbol{S}}_{\mathrm{A}}\hat{\boldsymbol{S}}_{\mathrm{B}} \tag{4.15}$$

in place of the isotropic Fermi contact interaction $\hat{\boldsymbol{H}}_{\mathrm{hf,iso}}$ (Eq. (4.9)) and the anisotropic electron dipole-dipole interaction

$$\begin{aligned}\hat{\boldsymbol{H}}_{\mathrm{ee,dip}} &= \hat{\boldsymbol{S}}_{\mathrm{A}}\boldsymbol{D}_{\mathrm{ee,dip}}\hat{\boldsymbol{S}}_{\mathrm{B}} \\ &= -\frac{\mu_0}{4\pi}g_{\mathrm{a}}g_{\mathrm{b}}\mu_{\mathrm{B}}^2\left(\frac{3(\hat{\boldsymbol{S}}_{\mathrm{A}}\boldsymbol{r})(\boldsymbol{r}\hat{\boldsymbol{S}}_{\mathrm{B}})}{r^5} - \frac{\hat{\boldsymbol{S}}_{\mathrm{A}}\hat{\boldsymbol{S}}_{\mathrm{B}}}{r^3}\right)\end{aligned} \tag{4.16}$$

replacing the corresponding anisotropic electron-nuclear spin interaction $\hat{\boldsymbol{H}}_{\mathrm{hf,dip}}$ (Eq. (4.10)).

In proteins, the coupling constant for Heisenberg exchange $J$ can be approximated by an exponential

$$J(r) = \exp^{-\beta r} \tag{4.17}$$

where $\beta$ is on the order of 15 nm$^{-1}$, thus making it largely irrelevant for distances above 1.4 nm, where the dipolar interaction, due to its r$^{-3}$-dependence, becomes the dominant term.

In the high-field approximation, the two spins can be assumed to be parallel, and the dipole-dipole interaction simplifies to

$$\hat{\boldsymbol{D}} = -\frac{\mu_0}{4\pi}g_{\mathrm{a}}g_{\mathrm{b}}\mu_{\mathrm{B}}^2\frac{1}{r^3}\begin{pmatrix}1 & 0 & 0\\ 0 & 1 & 0\\ 0 & 0 & -2\end{pmatrix} = \begin{pmatrix}-\omega_{\mathrm{DD}} & 0 & 0\\ 0 & -\omega_{\mathrm{DD}} & 0\\ 0 & 0 & 2\omega_{\mathrm{DD}}\end{pmatrix} \tag{4.18}$$

---

[B] i.e. their interaction is small compared to the external magnetic field

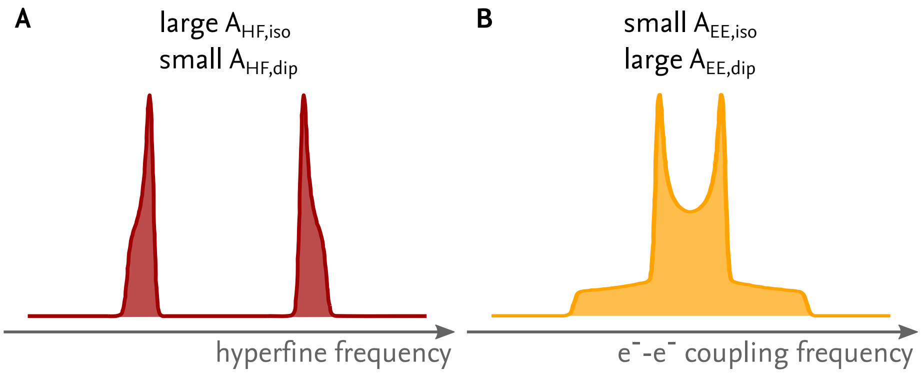

FIGURE 4.3. – **Proton hyperfine splitting compared to electron-electron couplings.** (A) α- and β-protons usually exhibit large isotropic and small anisotropic couplings, resulting in two separated lines in the spectrum. (B) Interactions between two electron spins are dominated by anisotropic dipolar couplings at typical distances, giving rise to a Pake pattern.

The dipolar coupling appears as broadening of the EPR spectrum for samples with low inter-spin distances r <1.5 nm, where the $r^{-3}$-dependence of the broadening can be used to extract distance information. At larger distances, the broadening becomes too small in relation to typical g-anisotropies and can usually be ignored[C].

If the magnetic moments of the interacting spins are parallel – a reasonable assumption for organic radicals in high fields – the dipolar interaction can be described solely in terms of the angle θ between the magnetic field axis and the spin-spin vector.

$$\hat{\boldsymbol{H}}_{\text{ee,dip}} = \omega_{\text{DD}} \left(1 - 3\cos^2\theta\right) \hat{\boldsymbol{S}}_{\text{A}} \hat{\boldsymbol{S}}_{\text{B}}, \tag{4.19}$$

When regarding a disordered sample in frozen solution, all orientations of the interspin vector are present simultaneously. The distribution in Eq. (4.19) then results in a Pake pattern (Fig. 4.3).

Using the further assumption that $g_{\text{A}} = g_{\text{B}} = g_{\text{e}}$, Eq. (4.18) can be used to derive a direct relation between the dipolar coupling frequency $\nu_{\text{DD}} = \frac{\omega_{\text{DD}}}{2\pi}$ and the distance $r$ of the two spins $A$ and $B$

---

[C] The linewidth of a well-resolved first-derivative rigid nitroxide EPR spectrum is on the order of 0.5 mT at X-Band frequencies (9.6 GHz), corresponding to ≈12 MHz. Assuming that a broadening of half that width can be safely detected, the limit is actually about 2 nm. However, this assumes a homogeneous nitroxide environment. In a real sample, the environment will be inhomogeneous and/or different for the two nitroxides, introducing additional broadening.

$$r = \sqrt[3]{\frac{52,04\,\mathrm{MHz}}{\nu_{\mathrm{DD}}}}\ \mathrm{nm}. \tag{4.20}$$

While this formula isn't useful in practical terms, due to the fact that even for a single pair of spins with a single distance a Pake pattern, i.e. a frequency distribution is observed, as discussed above, it is still very convenient for a quick estimation of the expected coupling frequency at a given inter-spin distance and *vice versa.*

### 4.1.4 FURTHER CONTRIBUTIONS TO THE HAMILTONIAN

There are, of course, other contributions to the spin Hamiltonian. Since these are, however, without relevance to this work, they will not be discussed in detail. The main, additional, contributions are zero-field splitting and quadrupole coupling.

#### ZERO-FIELD SPLITTING $\hat{\boldsymbol{H}}_{\mathrm{ZERO}}$

Zero-field splitting describes the interaction between two electrons in those cases where the high-field approximation does not hold, i.e. in situations with very small or no external field. In some molecules, transition metal ions, and lanthanides, the coupling between individual unpaired spins becomes strong enough for them to appear as a single, effective spin with S > ½. Coupling between the individual spins causes a lifting of the spin state degeneracy at zero field by splitting the different energy levels according to

$$\hat{\boldsymbol{H}}_{\mathrm{zero}} = \hat{\boldsymbol{S}}\hat{\boldsymbol{D}}\hat{\boldsymbol{S}}. \tag{4.21}$$

#### NUCLEAR QUADRUPOLE COUPLING $\hat{\boldsymbol{H}}_{\mathrm{QUAD}}$

Similarly, a nucleus with spin I > ½ possesses a quadrupole moment that interacts with the electric field gradient at the nuclear coordinates, giving rise to the nuclear quadrupole coupling

$$\hat{\boldsymbol{H}}_{\mathrm{quad}} = \hat{\boldsymbol{I}}\hat{\boldsymbol{P}}\hat{\boldsymbol{I}}. \tag{4.22}$$

## 4.2 SPIN-CORRELATED RADICAL PAIRS

For a description of spin-correlated radical pairs (scRPs), it is first necessary to consider two cases of coupled electrons. Two electrons whose exchange and dipolar interaction is large compared to the Zeeman splitting (1) will form a four-level system that is best described in terms of triplet and singlet states, i.e. as one manifold with effective spin S = 1 and one with S = 0. This situation arises for example in oxygen atoms in the gas phase, photoexcited organic compounds or any other system where two unpaired electrons exist in close proximity to each other. If the two electrons are sufficiently separated that their mutual coupling is small compared to the Zeeman energy (2), their interaction is best described as a small pertubation to the Hamiltonian, and the resulting states no longer separate into triplet and singlet manifolds, but into states with mixed singlet-triplet character. The electron pair in this case is termed a biradical.

When a radical pair is created in state (1) but then transitions rapidly into state (2) by way of a separation of the two radicals, the result is a biradical whose states are populated retaining the spin correlation, i.e. the triplet or singlet character of its precursor. The result is called a spin-correlated radical pair (scRP). Examples of scRPs are radicals created by chemical reactions that are separated through diffusion or radicals in photoexcited organic compounds that get separated through electron transfer to neighbouring molecules.

In discussing scRPs, a simplified Hamiltonian

$$\begin{aligned}\hat{\boldsymbol{H}}_{\mathrm{rp}} &= \hat{\boldsymbol{H}}_{\mathrm{A}} + \hat{\boldsymbol{H}}_{\mathrm{B}} + \hat{\boldsymbol{H}}_{\mathrm{exch,AB}} + \hat{\boldsymbol{H}}_{\mathrm{dip,AB}} \\ &= \omega_{\mathrm{A}}\hat{\boldsymbol{S}}_{\mathrm{A,z}} + \omega_{\mathrm{B}}\hat{\boldsymbol{S}}_{\mathrm{B,z}} + J\left(\hat{\boldsymbol{S}}^2 + 1\right) + \frac{3}{2}d\left(\hat{\boldsymbol{S}}_{\mathrm{z}}^2 + \frac{1}{3}\hat{\boldsymbol{S}}^2\right),\end{aligned} \tag{4.23}$$

where $\hat{\boldsymbol{H}}_{\mathrm{A}}$ and $\hat{\boldsymbol{H}}_{\mathrm{A}}$ comprise all single-electron contributions to the Hamiltonian (Eq. (4.5) and (4.7)), while $\hat{\boldsymbol{H}}_{\mathrm{exch,AB}}$ and $\hat{\boldsymbol{H}}_{\mathrm{dip,AB}}$ describe the exchange (4.15) and dipolar (4.16) coupling between the two spins A and B, respectively, both terms rewritten in terms of the total spin of the system $\hat{\boldsymbol{S}} = \hat{\boldsymbol{S}}_{\mathrm{A}} + \hat{\boldsymbol{S}}_{\mathrm{B}}$.

Using the standard basis of a two-spin vector space

$$\begin{aligned}|T_{+}\rangle &= |\uparrow\uparrow\rangle \\ |T_{0}\rangle &= \frac{1}{\sqrt{2}}\left(|\uparrow\downarrow\rangle + |\downarrow\uparrow\rangle\right) \\ |T_{-}\rangle &= |\downarrow\downarrow\rangle \\ |S\rangle &= \frac{1}{\sqrt{2}}\left(|\uparrow\downarrow\rangle - |\downarrow\uparrow\rangle\right)\end{aligned} \tag{4.24}$$

of one singlet and three triplet states, $\hat{\boldsymbol{H}}_{\mathrm{rp}}$ can be written as

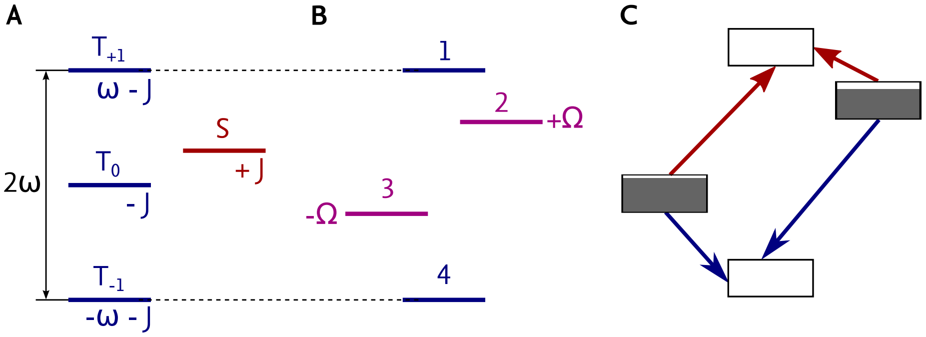

Figure 4.4. – **Energy levels of a spin-correlated radical pair.** The triplet ($T_{+1}$, $T_0$ and $T_{-1}$) and singlet ($S$) energy levels of the initial, strongly coupled radical pair (A) shift due to singlet-triplet mixing, producing two levels (1 and 4) with pure triplet and two (2 and 3) with mixed singlet-triplet character (B). See the main text for details. For a radical pair starting out as a singlet, the resulting absorbtive (red) and emissive (blue) transitions are shown in (C).

$$\hat{\boldsymbol{H}}_{\text{rp}} = \begin{pmatrix} \omega - J + \frac{1}{2}d & 0 & 0 & 0 \\ 0 & J & Q & 0 \\ 0 & Q & -J-d & 0 \\ 0 & 0 & 0 & -\omega - J + \frac{1}{2}d \end{pmatrix}, \tag{4.25}$$

with $\omega = \frac{1}{2}(\omega_\text{A} + \omega_\text{B})$ and $Q = \frac{1}{2}(\omega_\text{A} - \omega_\text{B})$ the sum and difference of the Larmor frequencies and $d = D\left(cos^2\theta - {}^1\!/\!_3\right)$ describing the angle $\theta$ between the dipolar axis and the magnetic field. Diagonalisation yields the new eigenvectors and eigenvalues of the system:

$$|1\rangle = |T_+\rangle \qquad \omega_1 = \omega - J + \frac{1}{2}d \tag{4.26}$$

$$|2\rangle = \cos\psi\,|S\rangle + \sin\psi\,|T_0\rangle \qquad \omega_2 = \Omega - \frac{1}{2}d \tag{4.27}$$

$$|3\rangle = -\sin\psi\,|S\rangle + \cos\psi\,|T_0\rangle \qquad \omega_3 = -\Omega - \frac{1}{2}d \tag{4.28}$$

$$|4\rangle = |T_-\rangle \qquad \omega_4 = -\omega - J + \frac{1}{2}d \tag{4.29}$$

where $\Omega = \sqrt{(J + \frac{1}{2}d)^2 + Q^2}$ and $tan2\psi = 2Q/(2J + d)$.

The eigenvectors $|1\rangle$ and $|4\rangle$ are identical to their counterparts in a normal spin-1 system, $|2\rangle$ and $|3\rangle$, however, represent mixed triplet-singlet states. The mixing angle $\psi$ is defined by the parameters $J$, $Q$ and $d$, $\psi = 2Q/\left(2J + d\right)$. The corresponding energy levels and their relation to the original singlet/triplet levels are

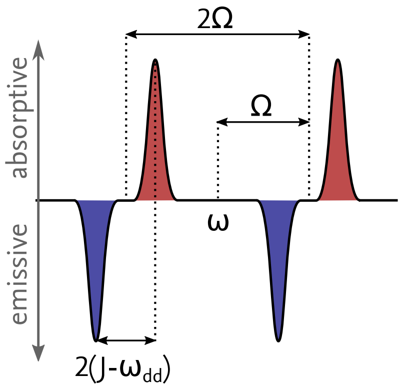

Figure 4.5. – **Simplified spectrum resulting from the spin polarisation in Fig. 4.4C.** In most system, each individual line is broadened by g-anisotropy and hyperfine couplings, resulting in a complex spectrum. Positive peaks by convention indicate microwave absorption (red), while negative peaks indicate emission (blue).

depicted in Fig. 4.4A and B.

As discussed, the radical pair "remembers" the spin state of its precursor. Since the original strongly coupled biradical exists either in a pure triplet or a pure singlet configuration, the same is true for the initial state of the radical pair. As a consequence, the initial configuration of the radical does not correspond to the thermal Boltzmann distribution. In a scRP originating from a singlet precursor, only $|2\rangle$ and $|3\rangle$ are populated. For a triplet precursor, $|2\rangle$ and $|3\rangle$ are less populated than $|1\rangle$ and $|4\rangle$. Figure 4.4C shows the configuration for a singlet precursor together with the allowed transitions between states.

The selection rule for an EPR transition ($\varDelta S = \pm 1$) allows for four transitions in this system, $|1\rangle \leftrightarrow |2\rangle$, $|1\rangle \leftrightarrow |3\rangle$, $|2\rangle \leftrightarrow |4\rangle$ and $|3\rangle \leftrightarrow |4\rangle$. In a radical pair derived from a singlet precursor, for example, this results in four EPR lines (Figure 4.4C and 4.5), two of which, $|3\rangle \rightarrow |1\rangle$ and $|2\rangle \rightarrow |1\rangle$, are absorptive, the other, $|3\rangle \rightarrow |4\rangle$ and $|2\rangle \rightarrow |4\rangle$, emissive. Hyperfine interaction and g-anisotropy in real systems lead to each individual line having its own, broadened and potentially structured, spectrum, causing the four lines to overlap. The resulting spectrum is often complex and the underlying parameters difficult to disentangle.

## 4.3 Spin System Evolution

To understand the principles of EPR, it is necessary to consider the time dependent evolution of the spin system. The equations used here to describe the spin system's time evolution, called Bloch equations, are exact geometrical representation of a

S = ½ in a magnetic field neglecting relaxation and are thus formally equivalent to the Schrödinger equation. For the sake of simplification, they will, however, only be used in terms of the observable's expectation values for a spin ensemble.[D]

### 4.3.1 BLOCH EQUATIONS

The spin system is described by the macroscopic magnetisation $\boldsymbol{M}$ as the sum over all individual molecular magnets $\boldsymbol{M} = \frac{1}{V}\sum \nu$, with the preferred state $\boldsymbol{M}_0 = M_0 \boldsymbol{e}_{B_0} = (0, 0, M_0)$ parallel to the external field $\boldsymbol{B_0} \parallel z$[E]. The time evolution of this magnetisation is then given by the equation of motion

$$\frac{d}{dt}\boldsymbol{M} = \gamma \boldsymbol{M} \times \boldsymbol{B}_0 + \mathcal{R}\left(\boldsymbol{M}_0 - \boldsymbol{M}\right), \tag{4.30}$$

where $\boldsymbol{M} \times \boldsymbol{B_0}$ describes the interaction of the magnetisation with the magnetic field and $\mathcal{R} = [(1/T_2, 0, 0)\,; (0, 1/T_2, 0)\,; (0, 0, 1/T_1)]$ describes the relaxation of the magnetisation back to the preferred state $\boldsymbol{M_0}$. $T_1$, the longitudinal relaxation time and $T_2$, the transversal relaxation time[F] are phenomenological parameters that will be discussed later.

Equation (4.30) is solved by the time dependent function

$$\boldsymbol{M}(t) = R_z(\omega_0 t) \exp^{-\mathcal{R}t} \boldsymbol{M}(0) + \left(1 - \exp^{-\mathcal{R}t}\right) \boldsymbol{M}_0 \tag{4.31}$$

with $\mathcal{R}$ as defined above and

$$R_z(\varphi) = \begin{pmatrix} \cos\varphi & -\sin\varphi & 0 \\ \sin\varphi & \cos\varphi & 0 \\ 0 & 0 & 1 \end{pmatrix} \tag{4.32}$$

a rotational matrix describing a rotation around the $z$-axis and $\omega_0 = \gamma B_0$ the Larmor frequency. In sum, this solution describes a precession of the magnetisation around the $z$-axis, that, over time, spirals back towards the preferred orientation $\boldsymbol{M}_0$.

Disregarding the term describing relaxation, we next consider the influence of a second, time dependent, circularly polarized magnetic field $\boldsymbol{B_1} = B_1\left(\cos(\omega_{\mathrm{mw}} t), \sin(\omega_{\mathrm{mw}} t), 0\right)$ which is used to excite the spins and is provided by the magnetic component of microwave radiation. To describe the effect of this secondary magnetic field, it is convenient to switch to a coordinate system of the incidental circularly polarised

---

[D] A typical EPR spectrometers has a sensitivity on the order of $10^{12}$ spins, making only ensemble averages accessible to EPR.

[E] The orientation of the external field, and with it the laboratory frame of reference, is arbitrary. By convention the external field is always assumed to be in $z$-direction, i.e. $\boldsymbol{B} = (0, 0, B_0)$

[F] Named for the direction of their influence, towards or perpendicular to the preferred magnetisation.

wave, i.e. rotating around the $z$-axis with $\omega_{\mathrm{wm}}$. With the additional definition of the frequency offset between incidental wave and Larmor frequency $\Omega = \omega_0 - \omega_{\mathrm{wm}}$, the relaxation-less Bloch equation simplifies to

$$\frac{d}{dt}\boldsymbol{M} = \gamma \begin{pmatrix} -\Omega M_y(t) \\ \Omega M_x(t) - \omega_1 M_z(t) \\ \omega_1 M_y(t) \end{pmatrix}, \tag{4.33}$$

where $\omega_1 = \gamma B_1$ is the Larmor frequency of the magnetisation with respect to the second field $B_1$, describing a nutation of the magnetisation around an effective field, that itself precesses around the $z$-axis defined by $B_0$. The inclination between the effective and the external field is given by $\delta = \arctan(\omega_1/\Omega)$, For large $\Omega$, i.e. a large offset between excitation and Larmor frequency, the inclination is approximately zero. For $\Omega \to 0$, however, $\delta \to \pi/2$ and in the case of resonance $\Omega = 0$ the magnetisation solely precesses around the rotating $x$-axis defined by $\boldsymbol{B}_1$, $\boldsymbol{e}_{\text{x,rot}} = \boldsymbol{B}_1/B_1$[G]

$$\boldsymbol{M} = R_{x,rot}(\omega_1 t)\boldsymbol{M}(0). \tag{4.34}$$

This means that, in case of resonance between $\omega_{\mathrm{mw}}$ and $\omega_0$, a) $B_1$ resonantly transfers energy to the magnetisation and b) by applying a resonant $B_1$[H] only for a short time $\Delta t$, the magnetisation can deliberately be flipped to an angle $\delta = \omega_1 \Delta t$ with respect to $B_0$. The former forms the basis for cw EPR, while the latter is the foundational concept of pulsed EPR.

### 4.3.2 RELAXATION PROCESSES

As described in Eq. (4.30), the relaxation of the magnetisation back to the ground state $M_0$ is governed by two parameters, the longitudinal relaxation time $T_1$ and the transversal relaxation time $T_2$. To understand their origin, it is necessary to go from the pseudo-classical, macroscopic sample magnetisation back to regarding individual spins.

---

[G] For simplicity's sake, the rotating-frame axes $\boldsymbol{e}_{\text{x,rot}}$ and $\boldsymbol{e}_{\text{y,rot}}$ will be referred to only as $x$,$y$ from here onwards.

[H] It should be noted that for technical reasons the incidental microwave in an EPR experiment is linearly, not circularly polarised. Since a linearly polarised wave can be described as two circularly polarised waves with opposing rotational directions, and only one of these two can be in resonance, while the other will be at frequency offset of $2\omega_{\mathrm{wm}} \gg \omega_1$, this has no influence on the experiment.

### LONGITUDINAL / SPIN-LATTICE RELAXATION

Longitudinal or spin-lattice relaxation causes the magnetisation to return to the preferred orientation along $z$. This effect is due to individual spins flipping back from the excited to the ground state, changing their energy in the process. Spontaneous emission does not play a significant role in this process[113][I]. Rather, these spin-flips are induced by coupling to phonons. At low temperatures this process is mainly driven by direct transitions while at high temperatures Raman transitions dominate. Both effects are an exponential function of the temperature, leading to an absolute minimum of the spin-lattice relaxation at an intermediate temperature specific to the system.

Longitudinal relaxation represents a loss of *energy* to the spin ensemble, as well as coherence.

### TRANSVERSAL / SPIN-SPIN RELAXATION

Transversal or spin-spin relaxation describes a loss of *coherence* to the spin system. Fluctuations in the local magnetic field experienced by the spins causes variations in the spins' Larmor frequencies, leading to an coherent spin ensemble dephasing over time. Additionally, spins can undergo random flip-flop processes, in which two individual spins with identical Larmor frequencies exchange their respective states. Both processes retain the total energy of the spin ensemble.

This, too, is a temperature-dependent process, with higher temperatures generally implying a faster spin-spin relaxation.

## 4.3.3 THE RELEVANCE OF RELAXATION PROCESSES IN EPR EXPERIMENTS

Relaxation processes play an important role in all EPR experiments, both cw and pulsed. However, they affect cw and pulsed experiments differently.[J]

Continuous-wave experiments rely on the resonant energy transfer from the microwave $B_1$-field to the spin ensemble. The population of the excited state $n_1$ relative to that of the ground state $\mathrm{n}_0$ is given by

$$\frac{n_1}{n_0} = \frac{1}{1 + \alpha B_1^2 T_1} \tag{4.35}$$

were $\alpha$ is a transition-specific parameter. Obviously, for both large $B_1$ and long spin-lattice relaxation time $T_1$, this ratio approaches 1, no further energy is transferred and consequently no signal can be detected. Thus, cw experiments at low

---

[I] the expected rate of spontaneous emission at X-Band frequencies ($\approx$10 GHz) is on the order of 1000 h.

[J] For an extensive discussion of this topic, see Poole and Farach.[114]

temperatures generally require low microwave power. Conversely, the faster relaxation at higher temperatures makes cw EPR ideally suited for room temperature experiments.

As cw EPR does not require a coherent spin packet, the spin-spin relaxation has no effect on the experiment itself. Both $T_1$ and to a lesser extent $T_2$ do however influence spectral width, and the homogeneous broadening resulting from relaxation can be used to determine relaxation times.[114]

By contrast, pulsed EPR experiments do rely on the manipulation of a coherent spin packet. Since spin-spin relaxation represents a loss of coherence, this process directly limits the *pulse sequence's length* in a given experiment. The design of a pulse sequence in a pulsed EPR experiment is based on the assumption that the spins are initially in the ground state parallel to the external field. The return to this state is governed by the spin-lattice relaxation, making it the limiting factor for the *repetition rate* of the experiment.

In a non-idealised sample and under realistic experimental conditions, other relaxation processes than a pure exchange between two spins in the excited ensemble, e.g. fluctuations in the magnetic field $B_0$, contribute to the loss of coherence and therefore to $T_2$. To distinguish these processes from the "normal" spin-spin relaxation, these processes get subsumed into an effective phase-memory time $T_m$.

Obviously, the spin-lattice relaxation of the observed spin contributes to $T_m$, since the relaxation of a spin to the ground state is itself a loss of coherence of the excited spin packet. $T_1$ thus forms an upper limit for the phase-memory time.

Other than that, the most important of these effects is instantaneous diffusion[103]. This process occurs when, in addition to the spin ensemble A under observation, the microwave pulse — either due to ever-present inhomogeneities in the field $B_1$ or the frequency spectrum of the pulse itself — also flips additional spins B, some of which may be dipolarly coupled to spins in A according to (4.16). This additional flip causes a fluctuation in the local field at coupled spins in A, altering the phase relations between the spins in the ensemble and thus destroying coherence. Reducing the sample concentration, thus increasing the mean distance between spins and, consequently, reducing the dipolar coupling between spins, increases phase memory times.

Since field fluctuations influence $T_2$ (see above), any process that alters the local field at the observed spin reduces $T_m$. $T_m$ is thus also impacted by spin-lattice relaxation of other excited spins as well as flip-flop processes that do not directly involve the observed spin.

Crucially, the spins causing fluctuations do not have to belong to the species being observed. They can be "accidentally" excited spins as described above, or nuclear spins in the vicinity. In biological samples, with their relative abundance of spin-carrying protons both in the sample itself and in the water-based solvent, the latter dominate $T_m$.[103] These nuclear spins, for the most part, do not interact with the observed spin directly, but relax via transversal relaxation among themselves. The resulting fluctuations in the local field are related to the phase memory time via

$$\frac{1}{T_\mathrm{m}} \sim \sqrt{g_\mathrm{N}^3 \sqrt{I\,(I+1)}} \tag{4.36}$$

i.e. $T_m$ is dependent on the nuclear spin $I$, but much more so on g-factor $g_N$ of the nucleus in question. This results in e.g. protons causing faster relaxation than deuterons, despite the latter's spin $I = 1$.

## 4.4 BASIC EPR TECHNIQUE

An EPR spectrometer is always built from three major components, one, a microwave bridge, two, a resonant cavity or other resonant device and three, a magnet for the generation of $B_0$. The microwave bridge comprises a microwave source, phase and amplitude adjustments, microwave detection devices and — in the case of a pulsed bridge — devices to generate and shape pulses. Resonators can be e.g. a split-ring or dielectric ring, and are usually equipped with a cryostat for temperature control.

EPR spectrometers are operated in several narrow microwave bands. The reasons for this are a) the commercial availability of parts and b) the necessity of using a resonator, greatly limiting the spectrometer's bandwidth. This resonator bandwidth limitation also means that in a typical EPR experiment, the microwave frequency remains fixed while the magnetic field is swept to record the sample's spectrum. By far the most commonly used frequency band is X-Band (9.6 GHz).

### MAGNET

For excitation frequencies up to Q-Band (34–35 GHz), a normal, water-cooled electromagnet can be used. At higher frequencies, the resonance condition for $g = g_e$ can only be fulfilled with superconducting magnets. Regardless of the set-up, field homogeneity is of paramount importance, since, as has been discussed in Section 4.3.2, field inhomogeneities directly lead to line broadening.

### RESONATOR

The resonator fulfils two tasks. Firstly, by its geometry it minimises the electric component $E_q$ of the microwave within the sample, which would otherwise tend

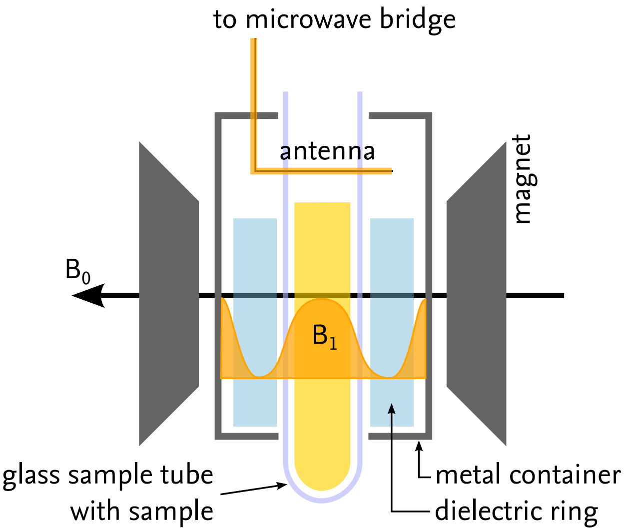

Figure 4.6. – **A schematic dielectric-ring resonator.** The resonant structure is formed by the dielectric ring (blue), with the sample centred inside. Microwave radiation is coupled into the resonator via an antenna situated above the ring. By adjusting the distance between ring and antenna, the coupling can be adjusted.

to be absorbed by the sample, damping the microwave and thus reducing sensitivity. This is especially important for biological samples in water-based buffer solutions. Secondly, by tuning the resonator to be critically coupled (i.e. impedance matched) to the resonant microwave frequency, microwave reflection from the cavity is reduced and the magnetic component of the microwave $B_1$ is greatly enhanced, leading to a stronger interaction.

The resonators used for this work were a dielectric-ring resonator (Figure 4.6), in which the electric component of the microwave is concentrated in a ring around the sample made from a dielectric material, usually sapphire, and a basic cavity resonator, consisting simply of a metal box that has its main resonant mode at the microwave frequency.

### 4.4.1 Continuous-wave EPR

For an cw experiment, the resonator is critically coupled (impedance matched) to the microwave. This means that a) the resonator operates at maximum quality factor Q and b) that the incoming microwave is fully coupled into the resonator, the reflected signal, and therefore the signal reaching the detector, is zero. When an EPR transition is excited, the sample will absorb microwave, detuning the resonator and thus causing some microwave to be reflected again. This signal is read

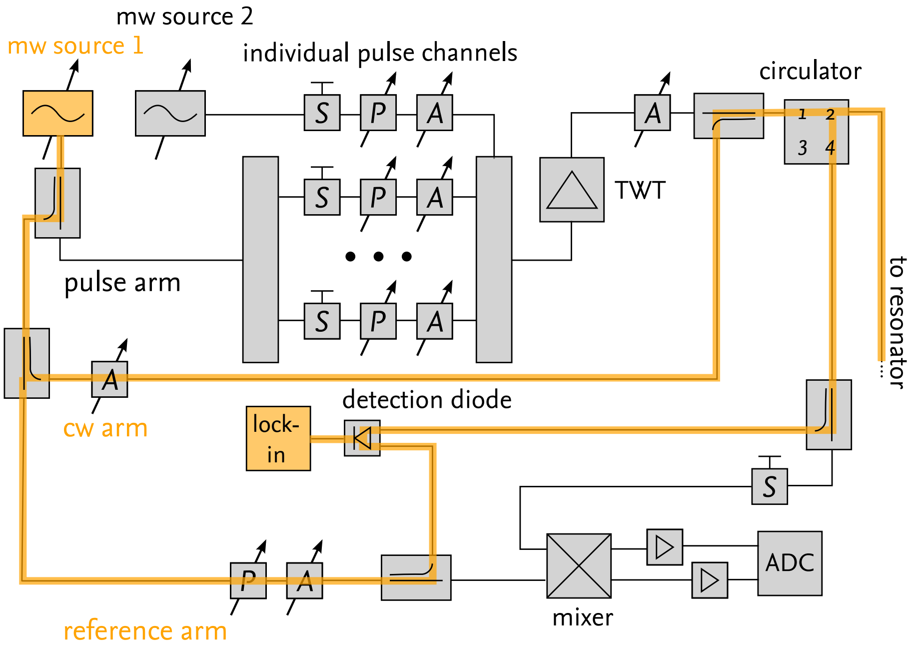

FIGURE 4.7. – **A schematic microwave bridge**. The signal path for a continuous-wave experiment is highlighted in yellow. Microwave reflected from the resonator is combined with the reference microwave and detected with a rectifier diode and a lock-in amplifier. *P* denotes a phase shifter, *A* an attenuator, *S* a microwave switch. Amplifiers are indicated with a triangle.

out at the detector.

Due to the theoretically infinitesimal bandwidth of a continuous wave, only a small fraction of spins in the sample is excited. This, however, is more than compensated for by the possibility of using extremely narrow bandwidth, and thus high Q, resonators. Additionally, a standard cw experiment modulates the magnetic field at kHz frequencies, thus modulating the signal and making it possible to use a lock-in amplifier at the detection and to suppress noise.

A schematic microwave bridge is depicted in Fig. 4.7, with the signal path for a cw experiment highlighted in yellow. The microwave is initially split on to two paths, the cw arm towards the resonator, and the reference arm. The microwave reflected from the resonator is separated from the incoming wave using a circulator, combined with the reference arm by constructive interference and detected with a rectifier diode. The amplitude of the reference signal is used to bias the detection diode to operate in the linear regime.

### 4.4.2 BASIC PULSED EPR

In a typical pulsed set-up (Fig. 4.8), the microwave is split into multiple channels of pulse gates, that can produce individually timed, phased and attenuated microwave pulses. These pulses are then again combined and strongly amplified using a travelling-wave tube amplifier (TWT) before being directed into the resonator. In order to accommodate the bandwidth of the pulses and reduce the ring-down time, i.e. the time it takes for the pulse to dissipate from the resonator, resonator with low Q-factor is used. To protect the nW-sensitive detectors from the kW microwave pulses, the detector is blanked during the pulses. This means that each pulse produces a dead time of the spectrometer, during which no detection is possible. Working around this dead time, typically on the order of about 100 ns after the end of a pulse, is a critical concern in pulsed EPR experiments. The microwave returning from the resonator is mixed with the reference microwave to remove the carrier frequency from the signal and recorded using a transient recorder (oscilloscope or other analog-digital converter (ADC)).

As demonstrated in Eq. (4.34), the length and amplitude of a microwave $B_1$ pulse can be used to flip the sample magnetisation to an arbitrary angle. The simplest possible pulse experiment would therefore be to flip all spins into the $x$-$y$-plane and to detect along the $y$- or $x$-axis of the rotating frame. This results in an instantaneous, slowly decaying complex signal called the free induction decay (FID). By recording and Fourier-transforming this signal, the full EPR spectrum could in theory be extracted[K].

This is, however, not feasible in general. Firstly, most EPR spectra are too broad to be excited simultaneously with a single pulse at achievable pulse lengths of $\approx$10 ns. Secondly, the aforementioned dead time means that it is impossible to start recording immediately after the pulse. A typical EPR FID decays fully within the dead time for most real samples.

### HAHN ECHOES

Erwin Hahn first suggested[115] the projecting the FID out of the dead time by applying a $\pi/2$-pulse[L] followed by a $\pi$-pulse after a delay time $\tau$. This second pulse causes the spin packet, which dephased in the $x$-$y$-plane after the initial plane, to refocus after an additional delay $\tau$, created back-to-back FIDs (Figure 4.10 and 4.9). The resulting magnetisation is coupled back into the resonator antenna. By choosing $\tau$ to be longer than the dead time, this so-called spin echo can be detected.

---

[K] This technique is commonly used in NMR spectroscopy.

[L] Pulses are commonly defined by their flip angle, a $\pi/2$-pulse corresponds to a pulse with a 90° flip angle. For the rest of this work, pulses will be referred to in this manner, with pulse separation times denoted with $\tau$, $\tau_1$, $\tau_2$ etc.

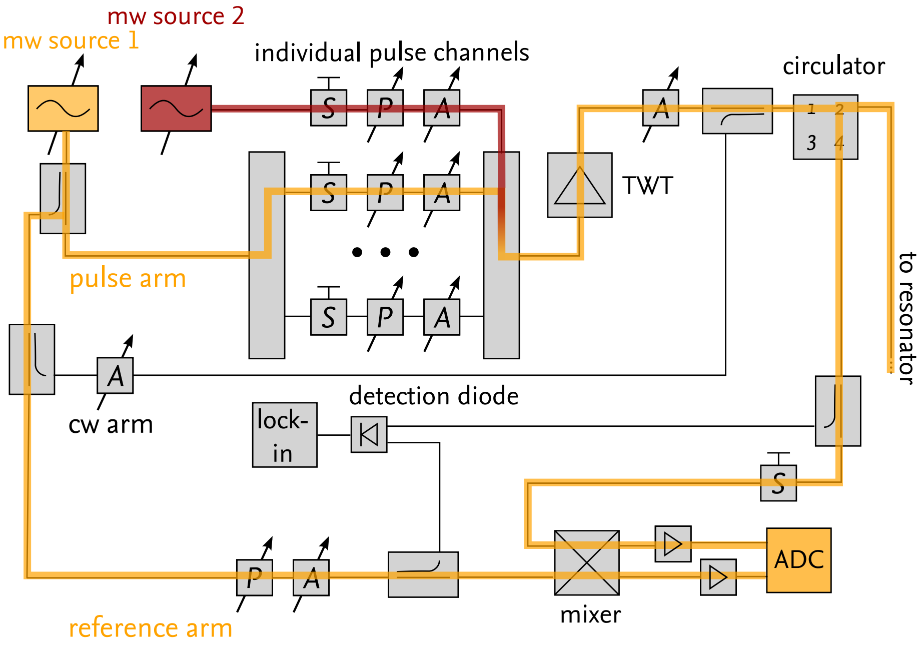

FIGURE 4.8. – **A schematic microwave bridge**. The signal path for a pulsed experiment is highlighted in yellow. Low power continuous microwave radiation is split into multiple channels that generate and shape pulses of individual timing and phase. These are then amplified using a travelling-wave tube amplifier (TWT). Microwave detection is achieved by downmixing the detection with the reference microwave and digitising the resulting signal with a transient recorder (oscilloscope or analog-digital converter (ADC)). A second microwave source, highlighted red, can be added to the setup for multifrequency experiments. For an explanation of the symbols, see Fig. 4.7.

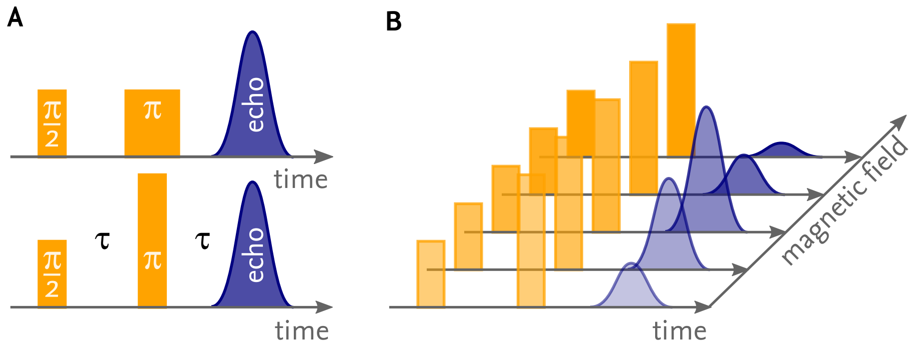

Figure 4.9. – **The Hahn echo sequence.** The spin system is initially excited using a $\pi/2$ pulse, followed by a $\pi$-pulse after a delay $\tau$ (A). After a further delay $\tau$, an echo is observed. $\pi$- and $\pi/2$-pulses can be achieved by either varying the pulse length (top) or pulse power (bottom). By repeating this sequence at different magnetic fields, the spectrum of the sample can be recorded (B). For a detailed picture of the spin manipulation involved, see Fig. 4.10.

Since this still does not solve the problem of incomplete excitation of the spectrum, the full spectrum is recorded by integrating over the echo (eliminating all but the exactly on-resonance component) and scanning the spectrum by repeating the same pulse sequence at different magnetic fields in an field-swept echo (FSE) experiment (Fig. 4.9B).

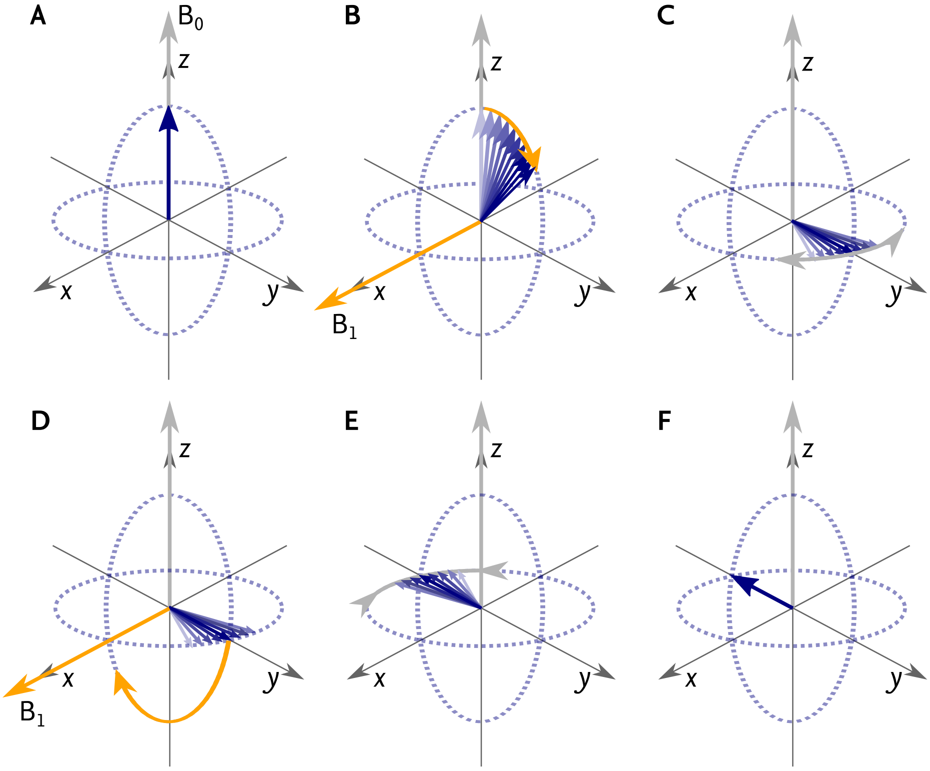

FIGURE 4.10. – **Spin picture of the Hahn echo sequence.** The spins are initially oriented along the external field $B_0$ (A): Applying a $\pi/2$ microwave pulse with $B_1$ in x direction causes the spins to rotate into the $x$-$y$-plane (B), where, after the pulse, the packet starts to dephase because the pulse also flips spins with Larmor frequencies slightly below and above the reference frequency of the rotating frame (C). The $\pi$ pulse after delay $\tau$ inverts the population in the $x$-$y$-plane (D), effectively exchanging the positions of "fast" and "slow" spins in the packet, causing them to refocus (E). After an additional delay $\tau$, the spins are refocussed again (F), allowing the resulting magnetisation to be detected outside the spectrometer's dead time.

## CHAPTER 5.

# METHODS & MATERIALS

This chapter discusses the methods used both in experiments and in data evaluation in Section 5.1 below, as well as detailed experimental parameters, measurement equipment and software in Section 5.2.

## 5.1 METHODS

### 5.1.1 ELECTRON-NUCLEAR DOUBLE RESONANCE

ENDOR is an EPR method, first developed by FEHER[116] in 1956, that is designed for detecting hyperfine couplings (HFCs). It is a two-frequency method, utilising both microwave frequencies for the excitation of electron spins and radio frequency (RF) frequencies to directly excite nuclear spin transitions. While initially a cw experiments, two pulsed variants were later developed, one by MIMS[117] in 1965 and one by DAVIES[118] in 1974. For this work, the latter was exclusively employed.

The pulse sequence of Davies ENDOR and the corresponding spin transitions are shown in Fig. 5.1. In a simplified picture of an isolated electron coupled to an isolated S = ½ nucleus, Zeeman interaction and hyperfine couplings split the electron-nucleus spin system into four levels $|\uparrow_e\uparrow_n\rangle$, $|\uparrow_e\downarrow_n\rangle$, $|\downarrow_e\uparrow_n\rangle$ and $|\downarrow_e\downarrow_n\rangle$. The first π-pulse selectively excites one of the electron transitions, creating a population inversion on that transition that can later be detected by a standard Hahn echo (see 4.4.2). If the RF pulse is in resonance with one of the nuclear spin transitions and has also a π-flip angle, it creates a population inversion in this nuclear transition, thereby ideally eliminating all population difference from both levels connected by the electron spin transition pumped by the initial π-pulse. Since only the spins contributing to a population imbalance can be detected in the following echo, this greatly reduces the echo intensity. By repeating the sequence while changing the RF frequency, the hyperfine spectrum, consisting of two lines centred around the free nuclear frequency $\nu_N$ and split by the hyperfine couplings $a_{hf}$ ($\nu_N > a$) or *vice versa* ($\nu_N < a$), can be recorded.

In essence, ENDOR can be described as EPR-detected NMR. The advantages of this method over standard NMR are twofold; one, only nuclear spins that are ac-

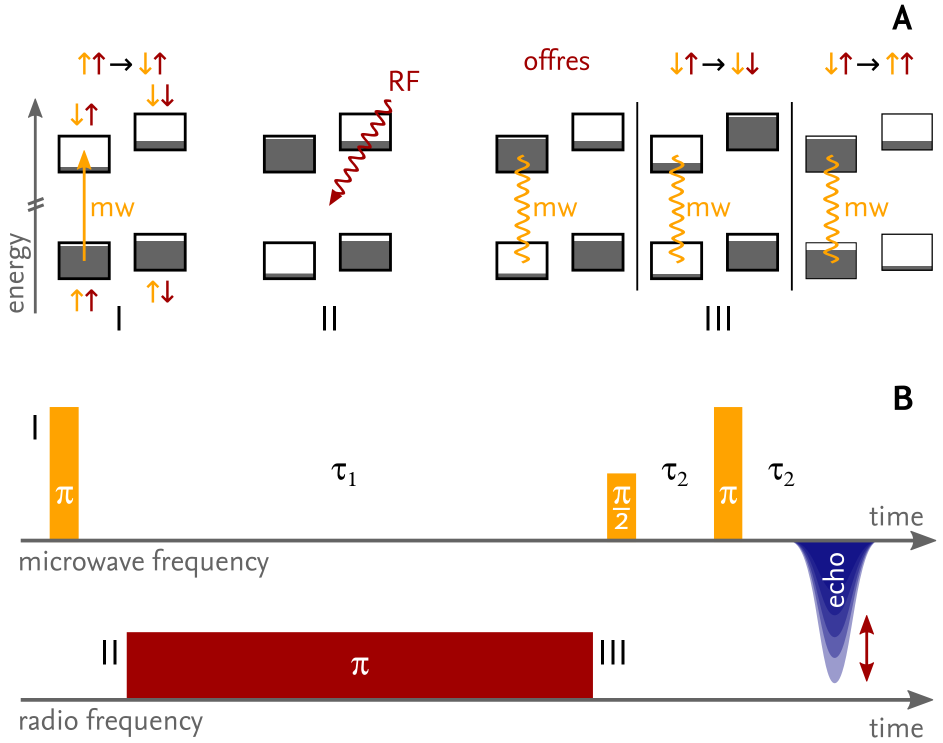

FIGURE 5.1. – **The Davies ENDOR sequence.** (A) The energy levels of the two-spin system over the course of the sequence, (B) the pulse sequence. Electron spins and micorwave excitation are shown in yellow, nuclear spins and RF excitation in red. The temporal positions of the three diagrams in (A) are marked by Roman numerals I-III. The initial pulse excites one of the EPR transitions (A-I) yielding a population inversion on that transition (A-II). Applying an RF pulse (A-II) can lead to three different cases: In the case of an off-resonant RF pulse, nothing further happens and an echo is observed when again probing the electron transition (A-III, first panel). For resonant pulses, the RF pulse eliminates the population inversion created by the microwave pulse, reducing the echo intensity (A-III, second and third panel).

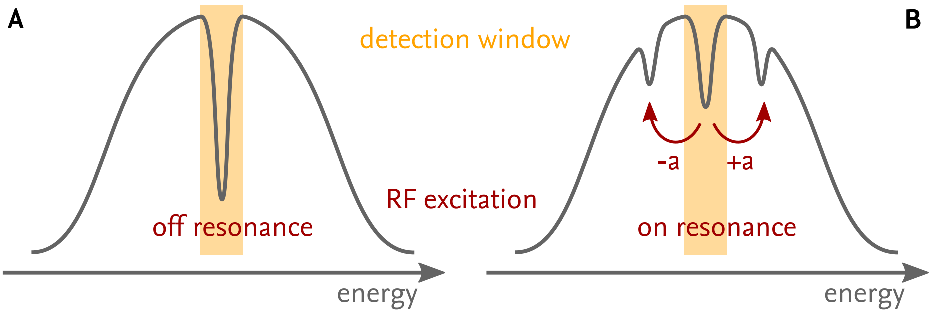

FIGURE 5.2. – **Davies ENDOR on an inhomogeneously broadened line.** Part of the hole created by the microwave inversion pulse is shifted towards lower and higher energy, depleting the hole and thus reducing echo intensity.

tually coupled to the electronic spin can be detected, making this method highly locally selective and two, the Boltzmann population imbalance between two electron spin levels is much higher than that of two nuclear spin levels, making the method much more sensitive[A].

In a real experiment, the microwave pulses cannot selectively excite only one of the two transition in the whole spin ensemble. To understand the detection principle under realistic conditions, it is necessary to consider the effect the different pulses have on an inhomogeneously broadened line (Figure 5.2).

Such a line of width $\Gamma_{\mathrm{inh}}$ consists of many superimposed spin packets, each with its own resonance frequency and homogeneous linewidth $\Gamma_{T_2}$. The initial $\pi$-pulse affects spins whose resonance frequency falls within the pulse's bandwidth, "burning a hole" into the line (Fig. 5.2a). The RF pulse, if resonant, shifts half of this hole to a resonance frequency different by the hyperfine coupling frequency $a_{\mathrm{hf}}$. The direction of the shift depends on whether the microwave pulse inverted the $|\uparrow_e\uparrow_n\rangle \rightarrow |\downarrow_e\uparrow_n\rangle$ or $|\uparrow_e\downarrow_n\rangle \rightarrow |\downarrow_e\downarrow_n\rangle$ transition. Thus, after a resonant RF pulse, half of the population remains at the original energy, one quarter gets shifted by $a_{\mathrm{hf}}$ to higher energies and one quarter gets shifted by $a_{\mathrm{hf}}$ to lower energies. Since the following Hahn echo only probes spins at the original position, this results in a 50% lower echo intensity.

It is immediately clear that this change can only appear when the shift is larger than the width of the hole. Contrary to normal practice, it is therefore important to choose a comparatively long inversion pulse. However, since the number of excited spins and thus the signal intensity is inversely proportional to the pulse length, a trade-off usually has to be made. Common inversion pulse lengths are between 100 ns and 200 ns. Thus, Davies ENDOR is inherently insensitive to small

---

[A] The population imbalance between the two $g = 2$, $m_s = \pm 1/2$ levels at 80 K and X-Band frequencies is about 0.6 %. For a proton under the same conditions it is about 0.001 %

HFCs. The Mims ENDOR sequence can improve on that to some degree, but it, too, suffers from the systematic limitation of the central hole.

## ENDOR, EXPERIMENTAL CONSIDERATIONS AND DATA ANALYSIS

**Choice of experimental parameters** Since experiments using single oocytes suffer from extremely limited effective sample quantities, the ENDOR experiments in this work were performed in Q-Qand (34–35 GHz) to take advantage of the increased sensitivity as well as the possibility of symmetrising the spectrum (see below). The main drawback of the Q-Band set-up — lack of power, necessitating longer pulses of limited bandwidth — is, as discussed above, not a limitation for Davies ENDOR.

The RF pulse transfers a large amount of energy to the sample. To avoid creating drifts and offsets in the measurement, the RF frequency is not swept continuously but stochastically. Thus, any influence the pulse has on the experiment is present as noise which can be compensated by longer accumulation, instead of drift which has to be corrected for in post processing. An additional advantage of stochastic sweeping of the RF frequency is that the impact of nuclear $T_1$ on repetition rates is reduced, as, even with the finite bandwidth of the RF pulse, a given nuclear spin is on average only excited every $\mathrm{n}^{\mathrm{th}}$ shot, where n is the number of points used to record the spectrum.

**Effects on ENDOR line intensities** Since the aim of the ENDOR experiments was — in part — to obtain the ratio of mobile-to-immobilised C8α methyl groups from the spectra, as far as possible all parameters impacting the intensity of ENDOR lines have to be taken into account.

Firstly, the line intensity is influenced by multiple properties of the spin system: It depends on the population imbalance of the levels between which a transition is induced. Since the levels are initially Boltzmann-populated, lines of higher frequency will also have higher intensities. Since the energy differences between nuclear spin states are small, this effect becomes significant only at very low temperatures. Additionally, the ENDOR transition moments contain contributions of the electron spin operators $\hat{\boldsymbol{S}}_\mathrm{x}$ and $\hat{\boldsymbol{S}}_\mathrm{y}$ for RF pulses along $x$ and $y$, respectively, that result in the intensities of a hyperfine line pair being scaled by $(1 \pm A_\mathrm{xx}/\nu_\mathrm{N})$, an effect called *ENDOR enhancement*.[119] Assymmetric spin relaxation rates also play a role.

Secondly, the line intensity depends on the RF power at the location of the sample. Relative line intensities are therefore negatively impacted by the linearity — or lack thereof — of the RF generator and amplifier used to generate the RF pulses as well as the coils coupling the RF waves into the resonator.

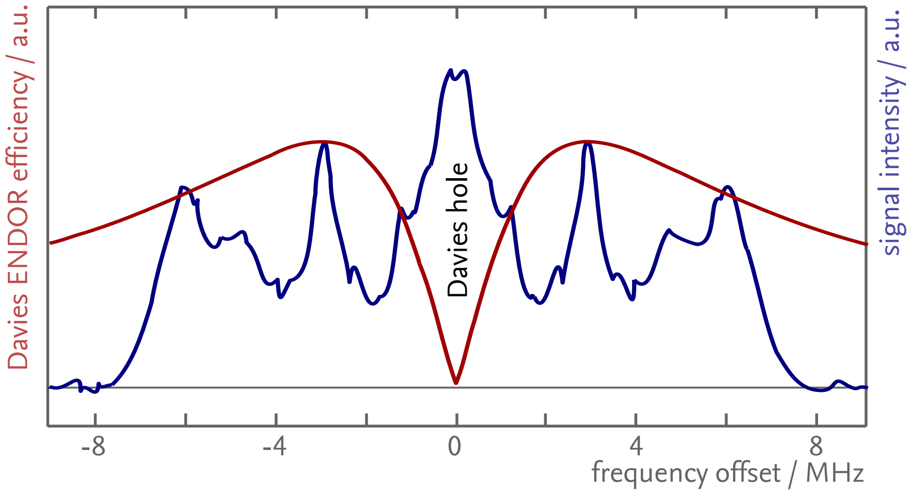

FIGURE 5.3. – **The effect of the Davies hole on ENDOR line intensity**. ENDOR efficiency when using a 120 ns inversion pulse according to Eq. (5.1) (red) as a function of the offset from the free nuclear frequency of the proton, compared to the ENDOR spectrum of a neutral flavin radical (blue). The suppression effect around $\nu = 0$ in the calculated efficiency is exaggerated since it does not take into account the finite excitation bandwidth of the RF pulse.

Lastly, the intensities of HFCs detected in Davies ENDOR depend on the length of the initial pulse $\tau_\pi$ and the effective hyperfine coupling $a_{\text{eff}}$ according to FAN *et al.*[120]

$$I_{\text{Davies}} = I_0 \frac{1.4 A_{\text{eff}} \tau_\pi}{0.7^2 + (A_{\text{eff}} \tau_\pi)^2}, \tag{5.1}$$

strongly attenuating lines at very small HFCs (Figure 5.3). While this formula suggests that very large HFCs are suppressed as well, this effect is often compensated by ENDOR enhancement,[119] leading to a roughly constant ENDOR efficiency for couplings that are large both relative to $\nu_N$ and $\tau_\pi$. Similarly, while it predicts an efficiency of zero for hyperfine couplings of zero, this is not true experimentally due to the bandwidth of the RF pulse. This, combined with the large number of very small couplings present in a real sample leads to significant signal intensity at the free frequency in real experiments.

All of these effects have been taken into account in the simulations performed in this work. Intensity variations due to the Boltzmann population factor and ENDOR enhancement are already included by the simulation software (see 5.2.3) used.

**Spectrum symmetrisation** In the absence of the aforementioned effects, a typical proton ENDOR spectrum is expected to be symmetrical around the free proton frequency. Therefore, by adding a mirrored version of the spectrum to itself, the spectral intensity can be increased twofold, resulting in a $\sqrt{2}$-fold increase in signal-to-noise ratio (SNR). Since the spectrum of each nucleus is individually split around its $\nu_N$, this is only feasible when the spectrum of one species, e.g. protons, does not overlap with that of another species, e.g. nitrogen. By choosing to perform the ENDOR experiments at Q-Band, this has been ensured in this study.[B]

An additional effect of symmetrisation is that any linear dependence of the line intensity on the resonance frequency will be eliminated in the process. This is, to a good approximation, true for Boltzmann population effects, ENDOR enhancement and the RF system's non-linearity.

It is, however, not true for the ENDOR efficiency due to the inversion pulse's length, since this itself is symmetric around $\nu_N$. It has therefore been taken into account explicitly by folding simulated spectra with the efficiency function (Eq. 5.1).

### AVOIDING LOCAL MINIMA AND DERIVING ERROR MARGINS IN ENDOR SIMULATIONS

When simulating ENDOR spectra containing multiple overlapping couplings from e.g. multiple protons, certain challenges arise:

- the increased number of free simulation parameters (at least four, $a_{xx}$, $a_{yy}$, $a_{zz}$ and the linewidth, per inequivalent nucleus) often renders automatic fit algorithms unreliable
- even when manually fitting or selecting subgroups of parameters for automatic fitting, this brings with it the very real possibility of getting stuck in local minima
- when multiple spectra overlap, changes in one can often be compensated by changes in the other, drastically increasing error margins for these "coupled" parameters. This is especially true for parameters defining the relative intensity of a line.

If, as was the case in this study, parameters are to be used in further calculations, it is necessary to also derive reliable error margins, something that is in general not easy to do with simulated spectra.

---

[B] The width of the flavin ENDOR spectrum is 20 MHz when disregarding the H5 coupling. Proton free Larmor frequency at typical Q-Band frequencies is 51.7 MHz, the most significant secondary contribution to the full ENDOR spectrum is nitrogen, with a free Larmoe frequency of 3.7 MHz. Nitrogen couplings that are large enough to overlap with the proton spectrum will have too low spectral density to be visible.

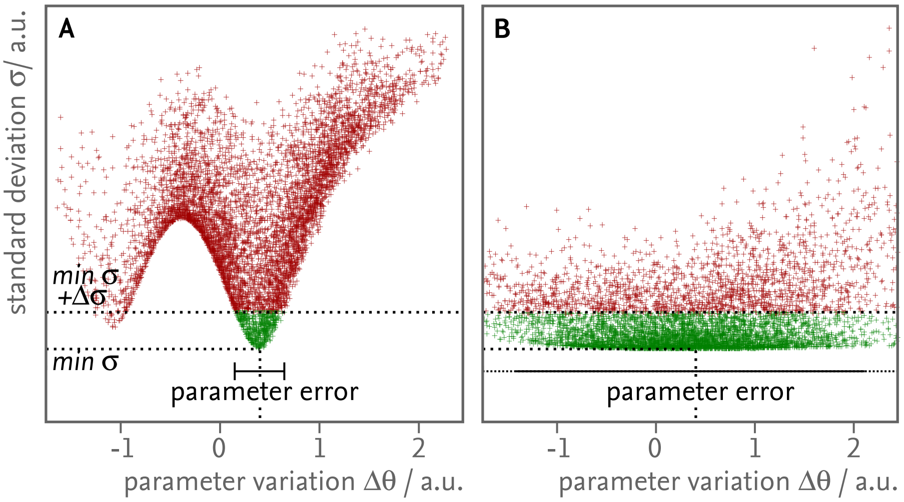

FIGURE 5.4. – **Evaluation of ENDOR simulation.** Parameters are randomly varied and the resulting error plotted over the parameter variation. (A) example of a parameter that has a local minimum (here an rotational angle influenced by the symmetry of the system), (B) example of one parameter being compensated by a second (here the intensities of two lines with very similar hyperfine parameters). The green markers represent those parameter sets that fall within the range of acceptable deviations.

The approach taken in this work was to first simulate the spectra manually, producing an initial guess for the "true" set of parameters, and then repeatedly simulating the spectra while varying subsets of the total parameter space in a Monte-Carlo experiment. For each set of parameters thus generated, the standard deviation $\sigma$ of the simulation from the experiment was calculated.

This method, one, finds an optimal simulation – the parameter set with the lowest $\sigma$ – within the confines of its variation space, two, addresses the problems discussed above and three, allows one to derive parameter errors.

Local and global fit minima as well as cases of parameters compensating each other can be identified by plotting the standard deviation $\sigma$ over the variation of a parameter $\delta$, the former as minima of the $\sigma$-distribution (Figure 5.4A), the latter as a distribution that is independent of the chosen variation parameter (Fig. 5.4B).

The same plots can be used to determine an error for the simulation parameter. This is achieved by setting an acceptable deviation of $\sigma$ from the optimum. From all parameter sets with lower $\sigma$ (Fig. 5.4, green markers), those farthest from the optimum define the acceptable range of parameters and thus the error.

This method is only feasible if individual simulations are fast enough to repeat them often. This is usually the case for proton ENDOR. For analysis of ENDOR

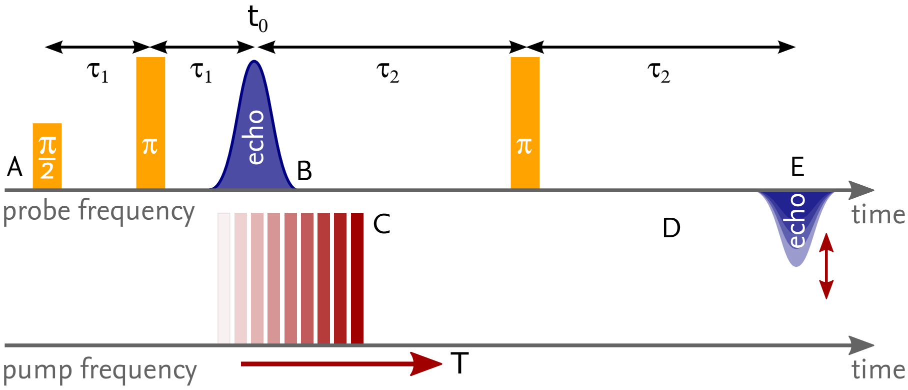

FIGURE 5.5. – **The DEER sequence.** Using pulses at two different microwave frequencies, the spins excited by the Hahn echo and detected with a refocusing $\pi$ pulse on the probe frequency are influenced by the dipolarly coupled spins exited by the pulse on the pump frequency, thereby changing the echo intensity. By changing the position of the pump pulse, the dipolar coupling can be determined. The positions (A-E) correspond to the respective panels in Fig. 5.6. See there and in the text for details.

intensities, spectra only need to be scaled, and the spectra of individual nuclei have only to be calculated once for all sets. The computational cost is then negligible.

In all data analysis, special attention was paid to minimise observer bias. To this end, software was written to automatically vary parameters, determine optimal parameters and calculate errors. Since the initial simulations were already quite convincing, parameter variations were biased towards zero using a normal distribution, in order to increase resolution in that area. From visual inspection of the simulated spectra, a 5% increase in $\sigma$ was set as the acceptable level. While this choice to some degree also represents observer bias, this mainly manifests itself in the absolute, not relative error values: Simulations with large minimal $\sigma$ will produce larger errors than those with small minimal $\sigma$, parameters that greatly influence the spectra will have smaller errors than those that contribute little, and so forth. Accordingly, the errors thus determined were used as weighing factors, i.e. relative errors, for further calculations.

### 5.1.2 ELECTRON-ELECTRON DOUBLE RESONANCE

ELDOR is a method designed to measure dipolar couplings between electron spins. It is today predominantly used in structural biology for distance measurements in spin-labelled proteins. ELDOR experiments were introduced, as a cw technique by BOWERS and MIMS[121] in 1959 and as a pulsed experiment by NECHTSCHEIN

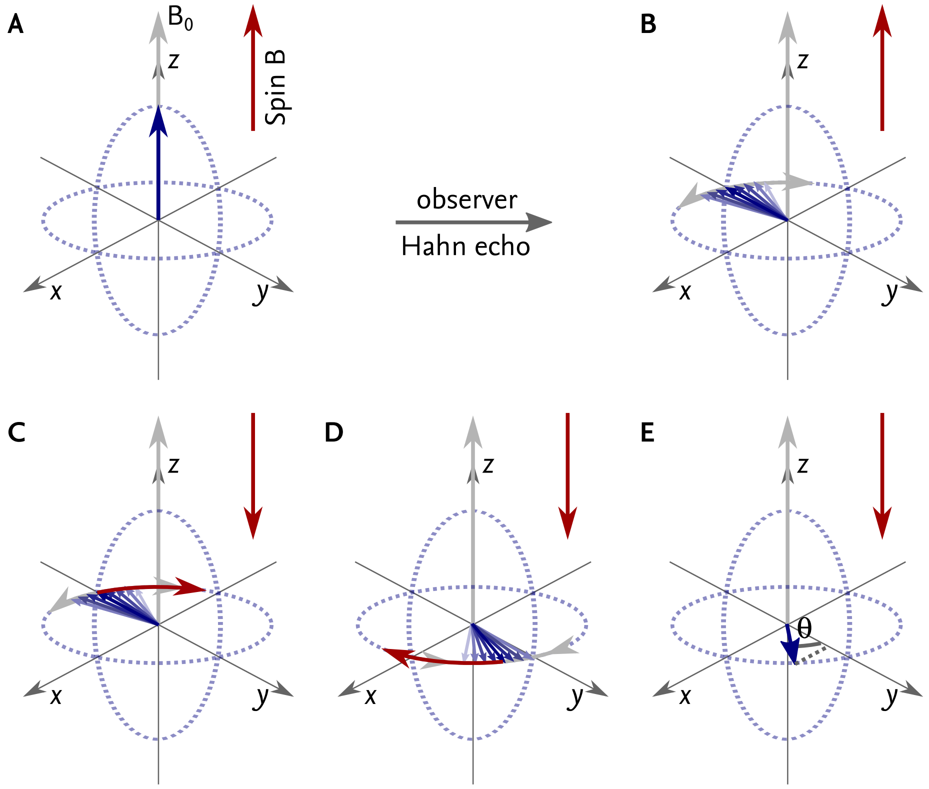

FIGURE 5.6. – **The DEER sequence - spin picture.** The spin packet A is prepared by a standard Hahn echo using the probe frequency (A-B). After flipping spin packet B using a $\pi$ pulse on the pump frequency, the changed effective field at spin A causes it to acquire a phase shift proportional to the time it evolved under the influence of the changed field and the dipolar coupling frequency (C). Refocussing packet A with a probe frequency $\pi$ pulse (D) recreates the echo at a phase offset $\theta$ (E).

and HYDE[122] in 1970, for the investigation of concentration effects and relaxation mechanics, and only later employed in distance measurements using the $r^{-3}$ dependence of the dipolar coupling by MILOV *et al.*.[123–125] The original experiment, called three-pulse ELDOR (3pELDOR), consists of three pulses, a Hahn echo experiment on one microwave frequency exciting one spin population A, with a $\pi$ pulse of different frequency set in between the Hahn echo pulses, exciting a different, dipolarly coupled population, B.

In 1998, the method was augmented by MARTIN *et al.*,[126] by introducing a second $\pi$ pulse after the Hahn echo sequence and moving the second-frequency pulse in between the $\pi$ pulses (Fig. 5.5) in a sequence termed DEER. This arrangement eliminates dead time at the cost of a longer pulse sequence and corresponding loss of signal intensity.

The experiment works as follows: In the absence of the pump pulse, only the spins in population A are excited by the probe pulses, an echo is produced at time $2\,\tau_1$ by the initial Hahn sequence, the spins are refocused by the second $\pi$ pulse, set at a delay $\tau_2$ after the initial echo, producing a second echo at time $\tau_2$ after the second $\pi$ pulse. By making the initial Hahn echo sequence as short as allowed by the spectrometer, as introduced by Pannier *et al.*,[127] the penalty in sequence length when compared to 3pELDOR is all but eliminated. This improvement has made DEER the de facto standard for ELDOR experiments, and the two terms are used, for the most part, synonymously.[C]

The effect of the pump pulse is shown in Fig. 5.6. The initial phase of the experiment (5.6A and B) is identical to the standard Hahn echo. At some time during the evolution of spin packet A after the second pulse, spin B is flipped by the pump pulse (5.6C). Since the two spins are dipolarly coupled, this changes the effective field at, and thus the Larmor frequency of the observer spin A, causing it to acquire a phase shift relative to the rotation frame of the detection frequency (5.6D). Thus, the observer spin packet A does not refocus along the $y$-axis of the rotating frame, but at an angle

$$\theta\left(T\right) = \omega_{\mathrm{dd}}\left(T - t_0\right), \tag{5.2}$$

where $\omega$ is the dipolar coupling frequency and $T$ is the time since spin B was flipped (5.6E). Only the component of the magnetisation parallel to $y$, $I = \cos\left(\omega_{\mathrm{dd}}\left(T - t_0\right)\right)$ is detected. By recording the signal intensity as a function of the pump pulse position, the dipolar frequencies can be detected in the time domain, while the constant-time nature of the experiment for the observer spins suppresses all other effects that could influence echo intensity. Fourier transformation yields the dipolar spectrum.

The advantage of DEER over 3pELDOR is that the pump pulse can pass over the echo without interference from detection pulses, allowing the zero time $t_0$ of the dipolar evolution to be recorded, knowledge of which, here as in all methods using Fourier transformation from phase space to local space, is essential.

The method typically needs to be applied at low temperature, as it is requires long pulse sequences and, consequently, slow relaxation rates. Additionally, since the dipolar coupling tensor is traceless, the species of interest has to be more or less immobile on the timescale of the experiment.

---

[C] Unless noted otherwise, ELDOR will denote the DEER experiment in this work.

### ELDOR, experimental considerations

Since the maximum detectable distance is, as per (4.18), proportional to the cubic root of the length of the time trace, necessitating long pulse sequences, ELDOR is severely limited by the phase memory time. $T_m$ for a spin labelled protein in water-based buffer is often below 1 µs at 80 K, too fast for a proper ELDOR experiment. Great care thus has to be taken to set up the experimental conditions in a way that maximises $T_m$.

**Choice of solvent** As explained in 4.3.3, a large contribution to $T_m$ relaxation comes from coupling of the electron spin to other electron spins and to the proton bath in the sample and solvent. Three steps can be taken to reduce this influence:

- The background interaction is linearly dependent on sample concentration, as reduced concentration increases the mean distance between electron spins. Since this, of course, also reduces the signal intensity, a trade-off usually has to be made between reduced relaxation and reduced primary signal intensity. In this work, a final concentration between 50–100 µM was found to be a good compromise.

- The coupling to the proton bath depends on solvent inhomogeneity. By adding 50% (v/v) glycerol to the sample, causing it to freeze as a glass, the relaxation time can be increased by about a factor of 1.5—2.

- By exchanging the solvent protons with deuterons, a theoretical increase in relaxation time of a factor of 13 can be achieved (see Eq. (4.36)). In practical terms, due to residual protons in the solvent as well as of course protons in the protein itself, a factor of 1.5—3 is common.

**Choice of temperature** As with the choice of sample concentration, the choice of measurement temperature also represents a trade-off. In principle, one would like to set up the sequence to be as long as possible, repeating it as fast as possible. Since the sequence length is, assuming $\mathrm{T_M} \ll \mathrm{T_1}$[D], limited by $\mathrm{T_M}$ while the repetition rate is limited by $\mathrm{T_1}$, and both increase at lower temperatures, this is usually not possible.

**Excitation pulses** The microwave pulses in an ELDOR experiment should be set up to excite the spectrum as broadly as possible, firstly to maximise the resulting signal by maximising the number of spins excited and secondly to minimise the influence of orientation selection by maximising the spectral range of the spins

---

[D] A valid assumption for nitroxide labels bound to a protein.

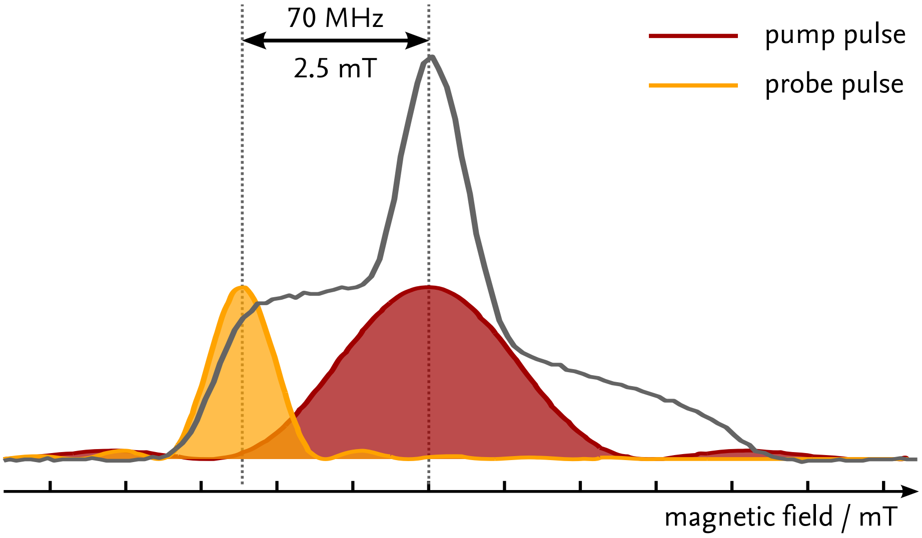

FIGURE 5.7. – **Bandwidth of a 12 ns (red) and 32 ns (yellow) pulse in relation to the nitroxide spectrum (grey).** The pulse's spectrum was calculated assuming perfectly rectangular pulses. Real pulses will contain less energy far off from the central frequency. The distance between the pulses is optimised to minimise overlap while maximising total bandwidth.

excited.[128] Ideally, the pump pulse's frequency is set to match the center frequency of the resonator and it's length set to the minimum $\pi$-pulse length the spectrometer will allow (usually, a 12 ns pump pulse can be achieved with a standard X-Band spectrometer using a 1 kW TWT). The observer pulses are set up under the same set of criteria, with the additional provision that they should only have minimal spectral overlap with the pump pulse. For a nitroxide label's spectrum, given a 12 ns pump pulse, these conditions are met by 32 ns pulses offset by 70 MHz. 32 ns $\pi/2$-pulses are created by halving the microwave power. Figure 5.7 depicts the pump and observer pulse's excitation profile in relation to the nitroxide spectrum.

**Nuclear modulation averaging** Some overlap between the excitation pulses is unavoidable. This overlap causes some observer spins to be influenced by both observer and pump pulses. For these spins, the experiment is no longer constant-time and additional phase shifts, mainly those caused by partially allowed/forbidden transitions, become dependent on the pump pulse's position. This results in electron spin-echo envelope modulations (ESEEM) superimposed onto the time trace. For protons, these can mostly be eliminated by increasing the Hahn echo's $\tau$ stepwise in each repetition to a maximum of one full nuclear modulation period. Since the phase of the ESEEM modulation depends on the Hahn echo $\tau$ while that of the dipolar evolution function does not, this averages their contribution.

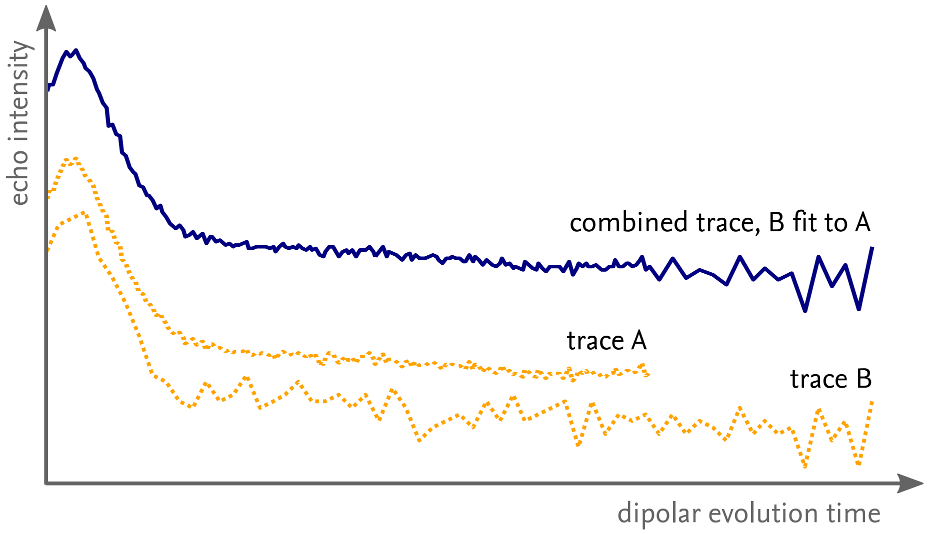

FIGURE 5.8. – **Combining ELDOR traces.** A high signal-to-noise ratio, short time trace A is combined with long trace with low signal-to-noise ratio B. The combined measurement retains all the information of the short trace, while increasing the maximum detectable distance.

This approach is only effective when the modulation intensity is small relative to the total intensity. It therefore does not work well when applied to deuterated samples or solvents, because the deuteron modulations are both low frequency and very intense. The former causes the echo intensity in the absence of ESEEM modulation to drop over one averaging period due to relaxation. The latter result in the echo intensity in the modulation's minima to drop to almost zero. Therefore, only traces where the initial $\tau$ matches maxima in the modulation contribute significantly to the averaging process, eliminating the effect. Additionally, the drastic intensity changes also render the averaging of proton modulations less effective. It is therefore not unusual to detect both in deuterated-buffer samples, even with averaging. However, they appear in the distance distribution as sharp features at predictable distances, making them easy to identify if they do not overlap with real distances.

**Combining multiple ELDOR traces** Due to their dependence on sample $T_m$, good SNR ELDOR measurements with high time resolution (i.e. small time increments and, accordingly, many points per trace) can only be achieved for comparatively short traces. These conditions, short time trace with high resolution are optimal for the detection of short distances. Due to the $r^{-3}$ dependence of the dipolar frequency, longer distances require much longer time traces, but can get away with much lower time resolution. The same applies for proper background correction (see Section 5.1.2 for details). When measuring distributions containing both long and short distances, setting up one experiment that addresses these requirements is not possible without drastically increasing measurement time on the limited Bruker hardware, allowing only for a constant Δt in a sequence.

It has been previously proposed[129] to ameliorate this problem by fitting a short, high resolution, high SNR DEER trace for the initial part of the dipolar evolution to a longer, lower resolution 3pELDOR trace, a method termed *DEER-Stitch*. The resulting combined measurement retains all the information contained in the short measurement, while also including interaction of spins with larger distances only contained in the long trace.

In this work, a slightly different approach was used to address the same problem. Instead of combining a short DEER with a long 3pELDOR measurements, two DEER measurements, long and short, where combined (Fig. 5.8). While this comes at the cost of increasing the length of the long experiment's pulse sequence by twice the τ of the initial Hahn echo compared to the standard DEER-Stitch approach, it has the advantage of having the peak at time zero present in both traces, making fitting much less ambiguous.

Again, to prevent observer bias, a program was written to phase-correct and then fit the two traces together, by minimising their difference's deviation from a constant.

### ELDOR, DATA ANALYSIS

Users of ELDOR are faced with two main challenges in data analysis, one, reliably deriving the distribution of inter-spin distances from the measured data and two, relating the thus determined distance distribution of spins to the underlying structure of the protein.

### BACKGROUND CORRECTION, MODULATION DEPTH AND LONG-DISTANCE ARTEFACTS

**Background correction** Any ELDOR measurement contains dipolar couplings both from the spins within one doubly labelled species of interest (intra-protein couplings) as well as couplings between spins in different species (inter-protein couplings). The latter give rise to a background dipolar signal that needs to be separated from the former to allow proper analysis. The time trace can be separated into the product of two contributions

$$I_{\text{DEER}} = B(t)F(t) = F(t)\exp\left(-kt^{d/3}\right), \tag{5.3}$$

where $d$ is the dimensionality of the background and $F(t)$ is the so-called form

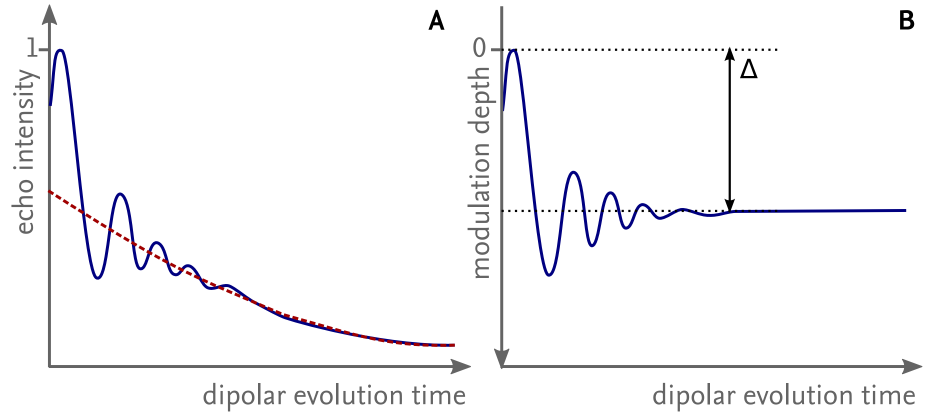

FIGURE 5.9. – **An example ELDOR trace of a labelled protein before (A) and after (B) background correction**. Coupling of the observer spin to spins in the homogeneous spin background appears as an exponential decay of the signal (A). Removing that from the time trace yields the dipolar evolution function of spins contained within one protein (B).

factor, the dipolar evolution function of intra-protein interactions. For a soluble protein, the distribution of background spins can be assumed to be homogeneous in three dimensions, leading to a monoexpoentially decaying background signal. Proteins bound in e.g. two-dimensional membranes can give rise to background distributions of lower dimensionality. $k$ is proportional to the sample concentration.[130,131] Fitting of $B(t)$ is reliable only in those parts of the timetrace where $B(t)$ can be approximated by a linear function. Low frequencies, i.e. large distances are difficult to distinguish from a non-linear $B(t)$ at long $t$, making background extraction in the presence of long distances difficult.

**Modulation depth** While $k$ is a measure for the concentration of the sample, i.e. the number of interacting spins outside one protein, the modulation depth $\varDelta = 1 - B(0)/F(0)$ (see Fig. 5.9) is a measure for the number of spins interacting within one protein. For a small number of interacting spins $N$ (small number of labels per protein), the normalised dipolar evolution function $D(t) = F(t)/F(0)$ is given by[132]

$$D(t) = \frac{1}{N} \sum_{A}^{N} \int_{\theta,r} \prod_{A \neq B}^{N} \left(1 - \lambda \left(1 - \left(\cos\left(\omega_{\text{dd}}^{A,B} t\right)\right)\right)\right) d\theta dr, \tag{5.4}$$

where $r$ and $\theta$ are the distance and angle between the spins and $\lambda$ describes the excitation efficiency. For $t = 0$, all contributing $\cos\left(\omega_{\text{dd}}^{A,B} t\right) = 1$ and $D(t) = 1$. For large $t$, the product of cosine functions averages to zero. The modulation depth is therefore given by[131–133]

$$\varDelta = 1 - (1 - \lambda)^{N-1}\,, \tag{5.5}$$

allowing for the determination of the average number of interacting spins $N$, assuming the excitation efficiency $\lambda$ is known.[131,134]

## Fitting of ELDOR data

If the distance distribution is very narrow, as is the case for paramagnetic species like the flavin radical in LOV domains[50] or the tyrosine radical in photosystem II,[135,136] analysis by simple Fourier transform is feasible in principle since the resulting spectrum in the frequency domain is a simple Pake pattern (see Eq. (4.19)). For small molecules in solution that show inherent flexibility, however, this is usually not the case.

This is especially true for spin-labelled samples, due to the high degree of flexibility of the MTSSL spin label (see Fig. 5.11a). To derive the spin distance distribution in those cases, one generates a distance distribution $P(r)$ of arbitrary shape. By calculating this distribution's spectrum and time trace

$$\begin{aligned} S(t) &= \int dr P(r) K(t,r) && (5.6)\\ &= \int dr P(r) \int d\chi \cos\left(\left(3\chi^2 - 1\right) \omega_{\mathrm{dd}}(r) t\right) && (5.7) \end{aligned}$$

and fitting it to the measured data, the "real" distribution can be determined.

Multiple approaches to generating $P(r)$ are common.

**Tikhonov regularisation** Initially, the distance distribution is generated from a superposition of multiple Gaussian peaks of identical width at different positions and intensities. Then, the number of individual peaks used is gradually reduced while the width of each peak is increased.

The algorithm seeks to minimise

$$\begin{aligned} G(P,\alpha) &= |S(t) - D(t)|^2 + \alpha |\frac{d^2}{dr^2} P(r)|^2 && (5.8)\\ &= \delta^2 + \alpha\sigma^2, && (5.9) \end{aligned}$$

that is the deviation of simulated time trace from experiment, plus the second derivative of the distance distribution, weighted by the *regularisation parameter* $\alpha$. This parameter determines the weight "smoothness" is given in the simulation;

the larger $\alpha$, the greater the penalty for a highly structured distribution. Ideally, the optimal $\alpha$ is chosen via the *L-curve*, the plot of the smoothness of $P(r)$, $\sigma^2$, over the deviation $\delta^2$: a too smooth $P(r)$ will produce a large deviation $\delta^2$ with small $\sigma^2$, while a too structured $P(r)$ will increasingly produce higher $\sigma^2$ while having little impact on the deviation $\delta^2$. In very high SNR traces with pronounced modulation, this will produce a sharp bend at the optimal $\alpha$. More typical traces will produce a more decay-like plot, while traces with low SNR or very broad and complex distributions will produce disordered L-curves. This is especially the case for distribution that contain sharp and unstructured features and reveals one of the major drawbacks of the method:

While the Tikhonov-regularisation approach is generally said to be "model-free", it imposes the rather strict requirement that $P(r)$ can be well described by a sum of Gaussians of identical widths. Often, this will lead to overly structured distributions that suggest resolution where there is none.

**Gaussian models** An alternative approach is to generate P(r) using a model of the distribution, most often a small number of variable width Gaussians. Calculation of the time trace and fitting is performed as for Tikhonov regularisation, with $\sigma^2$ being omitted. While this imposes an even stronger constraint on the possible distributions, it does take into account distributions that contain contributions of variable width. It will in general reproduce an approximate envelope of the distance distribution and is therefore especially suited for broader distribution with little structural resolution and distributions with distinct narrow and broad contributions.

**Long distance artefacts** The maximum observable modulation period is, in accordance with the sampling theorem,[137] defined by the length of the time trace $\tau_2$, . Since the phase of all modulations caused by dipolar interactions is intrinsically zero at $t = t_0$ (See Fig. 5.5 and Eq. 5.2), the maximum resolved inter-spin distance is, according to (4.20), $r = \sqrt[3]{52.04\tau_2/\mathrm{\mu s}}$. Tikhonov regularisation especially is prone to producing spurious peaks at this distance, mainly resulting from unresolved longer distance contributions and imperfect background correction.

### 5.1.3 TRANSIENT EPR

To investigate transient, most often photo-induced, paramagnetic species, trEPR is employed. In its simplest form, employed for this study, it is based around a cw EPR experiment (Figure 5.10). A laser pulse is used to excite transient paramagnetic species in the sample. Instead of a lock-in amplifier, the response of the system to the laser pulse is directly detected using a transient recorder triggered by the

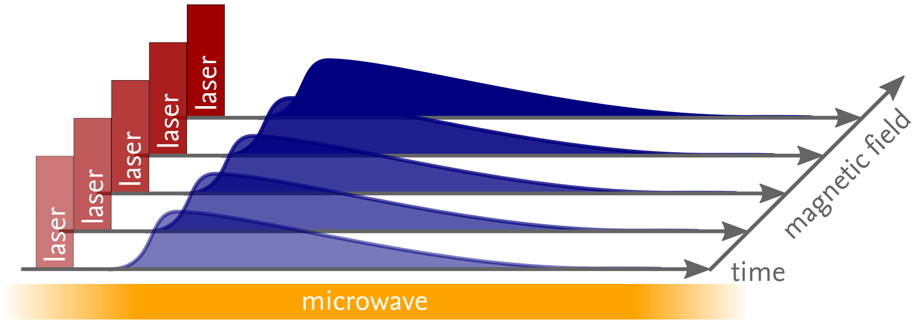

Figure 5.10. – **Transient EPR set-up.** Transient paramagnetic species are generated by a laser pulse (red) and detected using continuous-wave EPR (yellow) in a field-swept experiment. The EPR response of the system (blue) is recorded with a transient recorder. After background correction, the signal of the transient species can be extracted.

laser flash via a photo diode. The experiment is repeated at different field positions, creating a two-dimensional dataset.

The laser flash creates a large, slowly decaying and field independent background signal in the resonator. By measuring over a field range wider than the expected spectrum of the paramagnetic species, this background can be removed from the data by linear interpolation from the first and last magnetic field slice.

Contrary to cw EPR, a lock-in amplifier is usually not used. This makes the trEPR experiment inherently less sensitive and more time-consuming than standard cw EPR. However, sacrificing the increase in sensitivity from the lock-in amplifier results in a dramatically increased time resolution, essentially limited only by the bandwidth of the detection system, including the resonator.

### 5.1.4 Modelling spin label distance distributions

The spin label used in the study, MTSSL bound to a cysteine, can freely change the dihedral angles around all five bonds connecting the protein backbone to the nitroxide ring, resulting in a large number of possible rotamer conformations and accordingly a broad distance distribution between two such labels bound to a protein (Figure 5.11A).

Since ELDOR measures distances between the spin label's nitroxide radical at the end of the ring, but the structural information that one seeks to extract from the measurement are distances between protein backbone $C_\alpha$ carbons, it is necessary to simulate the possible conformations of the label attached to the protein. Because of this, ELDOR as a method is mainly useful in cases where a crystal structure of a protein (or a reasonable approximation of one) exists.

Two simulation approaches have been implemented and are commonly used.

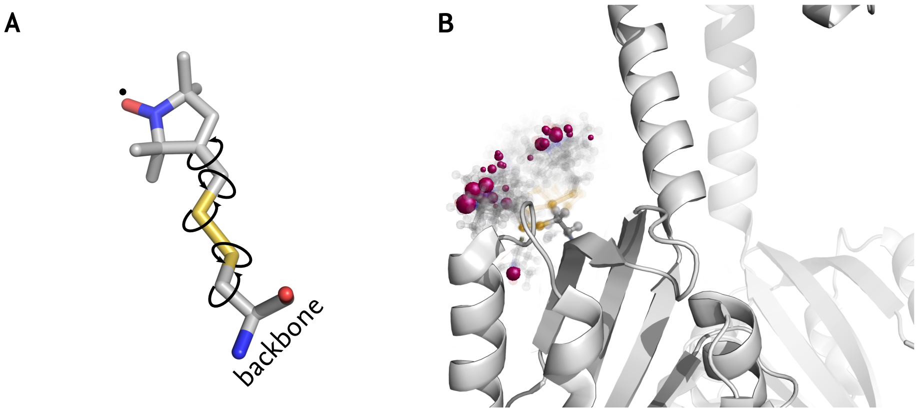

FIGURE 5.11. – **MTSSL mobility in proteins**. (A) Structure of MTSSL attached to a cysteine. The center of the spin density is indicated by a black dot. The spin label is free to rotate along multiple axes, namely the $C_\alpha$–$C_\beta$-, $C_\beta$–$S_1$-, $S_1$–$S_2$-, $S_2$–$C_{1'}$- and the $C_{1'}$–$C_2$-axis, giving an MTSSL–MTSSL distance a total variability of ≈1.5 nm. (B) spin label rotamers simulated at position Q93 in the crystal structure of YF1.[9] The centres of spin density are indicated in violet, larger balls indicate higher density.

Both work by mutating a cysteine into a given crystal structure and then attaching possible rotamers to that cysteine, filtering those rotamers that clash with the crystal structure. The main difference between the two lies in the way rotamers are selected.

The MMM program[138] uses a rotamer library approach, fitting spin label rotamers selected from a library of possible conformations generated using QM simulations. This approach is fast, because no rotamer structures have to be generated, plus it can take into account frozen-solution effects of the spin label condensing into a smaller selection of preferred rotamers when gradually cooled during sample freezing.

The MtsslWizard program[139] attaches a single rotamer to the structure and rotates it around all bonds, while filtering clashing rotamers. This approach is slower than the MMM approach, but scans a larger range of conformational space, finding more possible rotamers and thus producing a more conservative i.e._ wider guess of the distance distribution.

Neither method takes into account the flexibility of the protein backbone, both are based exclusively on a crystal structure.

### 5.1.5 ELASTIC NETWORK MODELLING

Changes in distances between labels observed by ENDOR can be related to structural changes of the protein by way of rigid-body docking (RBD), if the structural change involves multiple protein domains that individually mostly retain their structure, or an elastic network model (ENM) if the structural change is more complex.

In an ENM, each particle of a system is simplified as a point-like node and all interactions between particles as springs connecting these nodes. A protein is represented in an ENM by replacing the amino acid residues as nodes, using the $C_\alpha$ coordinates as the nodes' positions, essentially modelling the protein backbone. Two main categories of ENMs exist, gaussian network models (GNMs), which consider only the amplitude of node fluctuations, and anisotropic network models (ANMs), which consider both amplitude and direction of node movement. Including the direction of movement in the calculation makes the prediction of large-scale motions in proteins possible and was thus preferred over the faster-to-calculate GNM.

Several different models for assigning force constants for the protein network model are in use,[140–142] including models with a uniform force up to a certain cutoff distance or various polynomial dependencies of the force constant on the distance r, commonly $r^{-2}$ for GNMs and $r^{-6}$ for ANMs. For the anisotropic modelling used in this study, essential dynamics (ED)[143] ENM (ED-ENM), a $r^{-6}$-dependence fitted to reproduce protein flexibility observed in molecular dynamics (MD) and ED simulations.[144]

Once node coordinates and force constants are assigned, the vibrational dynamics of the protein model are computed by setting up the Hessian matrix from the force constants and solving the 3N-dimensional eigenproblem, where N is the number of nodes in the model, i.e. residues in the protein. The six lowest eigenvalues equal zero, and describe the three translational and three rotational degrees of freedom of the system. The remaining 3N - 6 eigenvalues are the squared vibrational frequencies of the protein's normal modes. The corresponding eigenvectors then describe the amplitude and direction of the relative movement of each node in a given normal mode.

Slow, i.e. low vibrational energy, modes contribute most to large scale vibrations, corresponding to deformations of the network that require the least energy. Testing of pairs of known protein structures has demonstrated[145,146] that large-amplitude structural changes in proteins proceed predominantly along these slow modes.

By using these slow modes to fit a given structure to a series of distance constraints, structural transitions can be modelled:[147,148] Using slow modes of an ENM to change a given state A structure of a protein to match the constraints imposed by measured distances in the protein's state B, a structure for B generated from A and the transition of the protein from A to B along vibrational modes can be visualised.

## 5.2 MATERIALS, EQUIPMENT & SOFTWARE

### 5.2.1 SAMPLE PREPARATION

All biochemical work, comprising site-directed mutagenesis (SDM), protein expression and purification, functional assays (if applicable) as well as spin labelling was performed by collaborators, namely Dr. Ralph P. Diensthuber and Nora Lemke in Prof. Andreas Möglich's group at the Humboldt Universität zu Berlin (LOV-Proteins), Xuecong Wang and David Robles in Dr. Margaret Ahmad's group at the University of Paris VI (cryptochromes) and Nils Krause in the group of Dr. Ramona Schlesinger at the Freie Universität Berlin (ChR2). Experimental details for this work can be found in [50, 149] for LOV proteins, [150] for cryptochrome and [151] for ChR2.

**LOV proteins YF1/AsLOV2** Samples intended for ENDOR experiments were used as-is, samples intended for ELDOR experiments were buffer-exchanged by washing with deuterated HEPES buffer and had 50% (v/v) fully deuterated glycerol (Sigma Aldritch, St. Louis, MO, USA) added.

The samples were transferred into quartz tubes (QSIL GmbH, Ilmenau, Germany; 1.2 mm/1.6 mm inner/outer diameter for ENDOR measurements and 3.0 mm/3.9 mm inner/outer diameter for ELDOR experiments), illuminated with a 450 nm LED (LUXEON Lumiled, Phillips Lumileds, San Jose, CA, USA) for 10 min and 5 min for ENDOR and ELDOR samples, respectively, and rapidly frozen in liquid nitrogen.

*Xenopus laevis* (*X. laevis*) oocytes were injected with YF1 C62A variant protein and incubated over night. To transfer them into tubes compatible with the spectrometer without rupturing them, special quartz capillaries were created. Using a hydrogen burner, tubes with a rounded top and almost closed bottom (Figure 5.12) were created from 1.4 mm/1.6 mm inner/outer diameter tubes open on both ends (QSIL). Individual oocytes were then sucked into the tubes using silicon tubing and syringes. During this, the rounded edges on the top end prevented the oocytes from rupturing, while the almost closed bottom end allowed buffer to be sucked through while preventing the oocyte from slipping out.

Once inside the quartz tubes, the oocytes were immediately illuminated for 5 min using the same set-up as above, and rapidly frozen in liquid nitrogen.

**Cryptochrome-2** Cell samples of cry2 variants expressed in Sf21 cells and purified protein for cw EPR spectroscopy were first transferred into 3.0 mm/3.9 mm

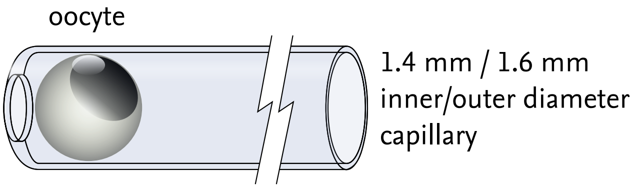

FIGURE 5.12. – **Measurement capillary for single oocytes.** Special tubes with an open top and almost closed bottom prevent the oocyte from rupturing while being transferred into the tube, and from slipping out during illumination and freezing. Using silicone tubing and a syringe, the oocyte can be sucked into the tube from the open end.

inner/outer diameter quartz sample tubes from QSIL, illuminated with a Streppel halolux 100HL halogen lamp at 450 nm and then rapidly frozen. For cell samples, multiple samples illuminated for 10, 20 and 30 min were investigated to verify that a maximally excited state was obtained. For purified protein, two samples for each variant were prepared, both with the same amount of sample, but one with 10 mM adenosine triphosphate (ATP) added. Samples were illuminated for 10 min with the set-up described above and then rapidly frozen. Purified protein intended for transient EPR had 10 % glycerol to ensure a liquid sample at 274 K and 5 mM $K_3Fe(CN)_6$ to enable flavin re-oxidation added. Two samples each, with and without 10 mM ATP, were produced, with the ATP-less sample topped up with $H_2O$ to ensure identical protein concentrations. Samples were then transferred into 1.0 mm/2.0 mm inner/outer diameter quartz sample tubes (QSIL) and kept at 2 ℃ until transferred to the spectrometer.

**Channelrhodopsin-2** Samples were used as-is. The samples were transferred into quartz tubes 3.0 mm/3.9 mm inner/outer diameter (QSIL), illuminated with a 450 nm LED (LUXEON Lumiled, Phillips Lumileds, San Jose, CA, USA) for 3 min and a 456 nm LED M455D2 (Thorlabs Inc, Newton, NJ, USA) for 20 s for initial and final ELDOR experiments, respectively, and rapidly frozen in liquid nitrogen.

### 5.2.2 MEASUREMENT EQUIPMENT & PARAMETERS

**LOV proteins YF1 and AsLOV2, channelrhodopsin-2** Q-Band pulsed ENDOR spectra were recorded using a commercial pulse EPR spectrometer Bruker E580 in conjunction with a cavity ENDOR resonator Bruker EN5107D2, all from Bruker Biospin GmbH, Rheinstetten Germany. For radio-frequency pulse generation a Bruker DICE2 frequency generator in conjunction with an Amplifier Research Model 250A250A 250W RF amplifier (Amplifier Research, Souderton, PA, USA) were used.

X-Band pulsed ELDOR spectra were recorded using an EPR spectrometer Bruker E680 with ELDOR microwave source E580-400U in conjunction with a dielectric-ring resonator Bruker EN4118X-MD5 and TWT microwave pulse amplifier Applied Systems Engineering Model 117X (Applied Systems Engineering Inc., Fort Worth, TX, USA).

For Davies-type ENDOR, a microwave pulse sequence $\pi$–$\tau_1$–$\pi/2$–$\tau_2$–$\pi$ using 40 ns and 80 ns $\pi/2$ and $\pi$ pulses, respectively, and a radio frequency pulse of 15 µs duration starting 1 µs after the first microwave pulse were used. The separation times $\tau_1$ and $\tau_2$ between the microwave pulses were set to 18 µs and 300 ns, respectively. The repetition time for the entire pulse pattern was adapted for each temperature to exclude any saturation effect due to the long $T_1$ relaxation time of the flavin radical. The repetition time thus varied from 10 ms at 120 K to 2 s at 5 K. Notably, 2 s is the longest consistent repetition time achievable with the instrument, and consequently to some degree saturation could not be avoided at 5 K. The proton free Larmor frequency at Q-Band is around 51.7 MHz, the RF sweep range was accordingly set to 41–61 MHz. All ENDOR spectra were recorded at magnetic-field values corresponding to the maximum intensity of the EPR spectrum of the flavin radical.

For ELDOR, the DEER sequence using 12 ns pump and 32 ns detection pulses was used. A constant excitation profile for probe pulses was achieved by adjusting the power of the $\pi/2$ pulse, allowing 32 ns $\pi/2$ and $\pi$ pulses to be used for probing. Pulse separation for the initial Hahn echo was 346 ns, optimized for the maximum of the deuterium ESEEM modulation, for deuterated samples and 200 ns everywhere else. Initial ELDOR experiments on ChR2 were performed using 80 ns for all pulses, since nuclear modulation averaging proved insufficient to suppress proton ESEEM artefacts. The experiments were performed at 40 K for YF1 and 50 K for ChR2, with a shot repetition rate of 4 µs. The field and pulse separation were set up as indicated in Fig. 5.7.

Cryogenic temperatures in both set-ups were set with an Oxford CF-935 cryostat and were controlled using an Oxford ITC503 temperature controller (Oxford Instruments, Oxfordshire, UK).

**Cryptochrome-2** Both cw-EPR and trEPR experiments were performed on laboratory-built X-Band (9–10 GHz) spectrometers. The spectrometer used for cw EPR consists of a microwave bridge ER 041 MR, microwave controller ER 048 R, magnet power supply ER 081 S and field controller BH 15, all from Bruker, and an AEG X-Band magnet (AEG Aktiengesellschaft, Berlin, Germany). The resonator used was a Bruker ER 4122 SHQ E cavity resonator; for signal detection a Stanford Research SR810 lock-in detector (Stanford Research, Sunnyvale, CA, USA) was used. Microwave frequency measurements were performed using an Agilent 53181A frequency counter (Agilent Technologies, Santa Clara, CA, USA). Transient EPR experiments were performed using a ER 046 XK-T microwave bridge, ER 048 R microwave controller, a field controller BH 15, all from Bruker, as well as a Varian V7900 Q-Band magnet and magnet power supply (Varian Inc., Palo Alto, CA, USA). An ER 4118X-MD5 resonator was used.

The sample was excited using a SpectraPhysics DCR-11 Nd:YAG Laser (Spectra-Physics, Santa Clara, CA, USA) with an OPTA OPO at 460 nm (OPTA GmbH, Bensheim, Germany). The EPR signal was detected using a LeCroy WaveRunner 104MXi (Teledyne LeCroy, Chestnut Ridge, NY, USA) as a transient recorder. The microwave frequency was measured using a Hewlett Packard 5352B frequency counter (Hewlett Packard, Palo Alto, CA, USA). For cw EPR, the samples were measured with 2 G modulation amplitude, 100 kHz modulation frequency and 100 ms lock-in time constant. The microwave power was 200 µW and the frequency around 9.38 GHz. For each measurement the current microwave frequency was recorded. The spectra are averages over 30 scans. Cell spectra were smoothed using a window of 3 % of data points. For trEPR, the samples were measured at microwave frequencies of around 9.69 GHz and 2 mW microwave power. Samples of cry2 wt were measured with 1 mJ pulse energy, while W374A and W321A were measured with 1.5 mJ. Each pair (±ATP) of samples was measured consecutively to minimize laser power drift, and the pulse energy was constantly monitored. Pulse energy variation over the course of a measurement pair was 10 % root-mean-square deviation (RMSD). The shot repetition rate was 2.5 Hz. Since the repeated photoexcitation gradually depletes the added $K_3Fe(CN)_6$, the signal intensity of each individual scan was recorded and the full accumulation cut off well before depletion was visible. This resulted in each measurement being accumulated from 30 scans with 10 shots per point, making for a total of 300 accumulations. Spectra were smoothed using a window of 3 % of data points.

Cw EPR measurements were performed at 80 K, the trEPR measurements at 274 K. Low temperatures were reached with an Oxford ESR 910 cryostat and Oxford ITC503 temperature controller and a laboratory-built cryostat with LakeShore 321 Autotuning temperature controller (LakeShore cryotronics, Westerville, OH; USA) for cw and transient experiments, respectively.

### 5.2.3 SOFTWARE

The spectrometers were controlled using the Xepr software package from Bruker for pulsed machines and the fsc2 software package[152] for cw and trEPR machines.

All data analysis was performed using MatLab (The MathWorks Inc., Natick, MA, USA), Origin (OriginLab, Northhampton, MA, USA), and PyMol.[153] ENDOR simulations were performed using the MatLab toolbox EasySpin.[154] For ELDOR data evaluation the MatLab toolbox DeerAnalysis[155] was used. Label rotamer simulations were performed in the MatLab Toolbox MMM[138] and the PyMol plug-in MtsslWizard.[139] Elastic network modelling using the ED-ENM force constant model[144] was performed using MMM. Rigid body modelling was performed in PyMol using mtsslDock.[156] The temperature dependence of the fraction of mobile C8α methyl signal was globally fitted to phenomenological logistic functions using Origin.

## CHAPTER 6.

# RESULTS & DISCUSSION

This chapter describes the data obtained from each of the three biological systems described in Chapters 2 and 3 as well as discusses the results. The structural investigation of ChR2 is presented in Section 6.1, research into strutural basis of the LOV signalling mechanism and recovery kinetics is presented in Sections 6.2 and 6.3, respectively, and, finally, the influence metabolites have on the light sensitivity of cryptochrome-2 will be discussed in Section 6.4.

## 6.1 INVESTIGATING THE DARK AND LIGHT STATE OF CHANNELRHODOPSIN-2 USING ELDOR

To determine the conformational changes the tertiary structure of ChR2 undergoes during its photocycle (Section 3), inter-helical distances were measured using SDSL and ELDOR in order to detect shifts in the TM helices' relative positions.

Wildtype ChR2 contains nine native cysteines that are, to varying degrees, accessible to MTSSL. For this study, all but one (C79, abbreviated ChR2-C79) or two (C79 and C208, abbreviated ChR2-C79/C208) cysteines were replaced by alanine, with the exception of C128, which was replaced with threonine. The C128T mutation causes the variants to accumulate the conductive state $P_3^{520}$ upon illumination,[97,157] while the wt protein accumulates $P_4^{480}$, a desensitized, non-conductive state.[96] A third mutant based on ChR2-C79 with additionally Q117 replaced by cysteine, was also investigated. Unfortunately, no constructs lacking C79 could be expressed at sufficient levels. This results in all variants except ChR2-C79 being doubly labelled. The chosen variants yield two label positions on the cytoplasmic side of the channel, with C79 situated in the loop connecting helices A and B, adjacent to B, and C208 in helix F at the beginning of the loop connecting it to helix E and one position on the extracellular side, Q117C in helix C.

Cw spectra of ChR2-C79 (Figure 6.2A, blue) show the label at cysteine 79 to be mostly rigidly attached to the protein backbone, as evidenced by the peaks at 332.5 mT and 339.5 mT. The presence of signal especially between 332.5 mT and 334.0 mT, however, indicates that fractions with higher mobility are also present

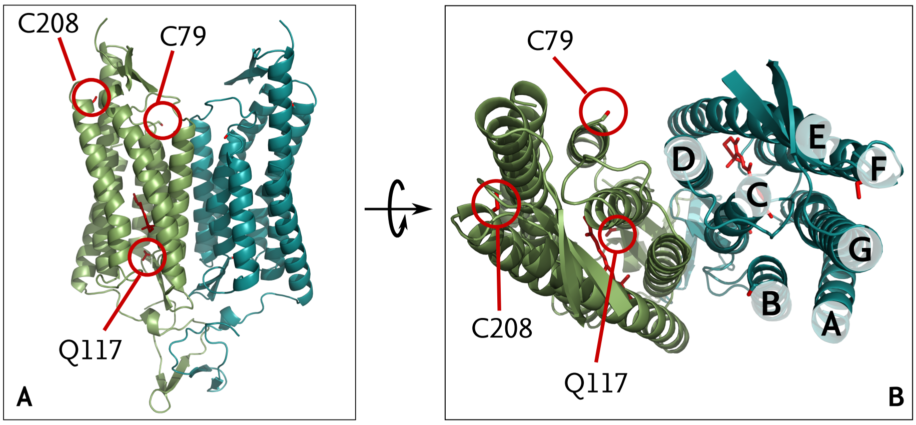

Figure 6.1. – **Labelling positions in channelrhodopsin-2.** Two naturally occurring cysteines on the cytoplasmic side, C79 situated in the loop between helices A and B adjacent to helix B and C208 in helix F, as well as one position on the extracellular side, Q117 in helix C, were chosen. All positions marked in red. The structure shown is the ChR1-ChR2 hybrid structure (pdb: 3UG9[90]).

Table 6.1. – **ChR2 variants investigated using ELDOR.** No variants lacking C79 could be expressed. The substitution C128T, present in all variants, causes the conducting state $P_3^{520}$ to be accumulated.

| Construct name | Substitutions | Description |
|---|---|---|
| ChR2-C79 | C34,36,87,179,<br>183,208,259A,<br>C128T | Only C79 remaining |
| ChR2-C79/C208 | C34,36,87,179,<br>183,259A,<br>C128T | C79 and C208 remaining |
| ChR2-C79/Q117C | C34,36,87,179,<br>183,208,259A,<br>C128T, Q117C | Only C79 remaining + Q117C |

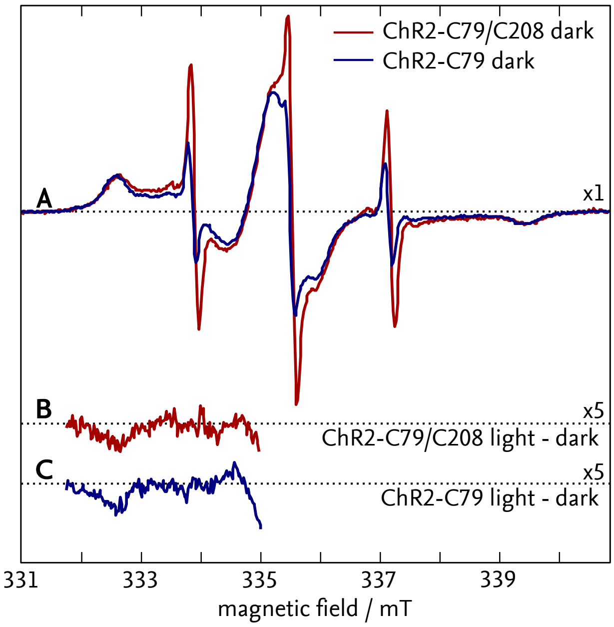

FIGURE 6.2. – (A) Room temperature continuous-wave spectra of spinlabelled ChR2 variants ChR2-C79 (blue) and ChR2-C79/C208 (red). Sharp peaks at 332.5 mT and 339.5 mT correspond to the label at C79 and indicate a rigidly bound label. The spectrum of ChR2-C79/C208 (red) exhibits additional intensity between 333 mT and 339 mT, indicating a more flexibly bound label. The peaks at 334.0 mT, 335.7 mT and 337.3 mT are due to free spin label. Light–dark difference spectra of ChR2-C79/C208 (B) and ChR2-C79 (C) show very slight changes of the mobility of the label at C79.

in the sample. The influence of free spin label, visible as three sharp peaks at 334.0 mT, 335.7 mT and 337.3 mT, is negligible. The spectrum of ChR2-C79/C208 (Fig. 6.2A, red) shows larger free label peaks, the integral intensity, however still indicates a less than 5 % free label content. Apart from the change in free label content, the spectrum shows additional signal between 333 mT and 339 mT that can be attributed to the label at cysteine 208. Hence this label has an overall higher mobility than the one at cysteine 79. While light–dark difference spectra (Figure 6.2B and C) show a slight change of mobility for the label at cysteine 79, the effect is not significant.

Initially ELDOR experiments on the dark/closed and illuminated/open states of ChR2-C79 and ChR2-C279/C208, reconstituted in MES buffer containing DM as detergent, were performed as described (Section 5.1.2, p. 48), the resulting time traces are shown in Fig. 6.3. For both variants, a 1.4 µs measurement was combined with a 2.8 µs one as described in Section 5.1.2 (p. 53) to create timetraces that are long enough for adequate background fits (Fig. 6.3, dotted lines). Since the achievable SNR of the 2.8 µs-traces was very low, distance distribution data extracted from the noisy sections of the datasets is very unreliable. To use the long datasets for background correction, while preventing long-distance noise artefacts from dominating the fit, the datasets were treated with a hamming window. While this has the effect of suppressing distances, whose associated dipolar frequencies are close to the length of the timetrace, given the noise these distances would not be distinguishable from noise artefacts.

### 6.1.1 The open state of ChR2

The dipolar evolution functions obtained after background corrections as well as the resulting distance distributions are shown in Fig. 6.4, in the left and right column, respectively. In all cases, a good fit (left hand columns, solid lines) of the data (shaded lines) could be obtained. Due to the presence of both narrow and broad distance components in the measured data, a distance model using two Gaussian distributions, with the width, center and relative integral intensities as free parameters, was found to be superior to the more standard Tikhonov regularisation approach.

The time trace of the singly labelled ChR2-C79 in the closed state (Fig. 6.4A, blue) shows a fast decay within the first 500 ns, incompatible with a singly labelled monomer. Indeed, the corresponding distance distribution (Figure 6.4B, blue) shows a sharp peak at 3.7 nm, proving that this ChR2 variant is dimeric in solution, as predicted by the C1C2 crystal structure.[90] The C79–C79 distance is well resolved, even though ChR-C79 lacks cysteines 34 and 36, which reportedly stabilise the dimer by forming disulphide bonds between the monomers.[90] A pronounced broad distance component between 2 nm and 6 nm is most likely due to

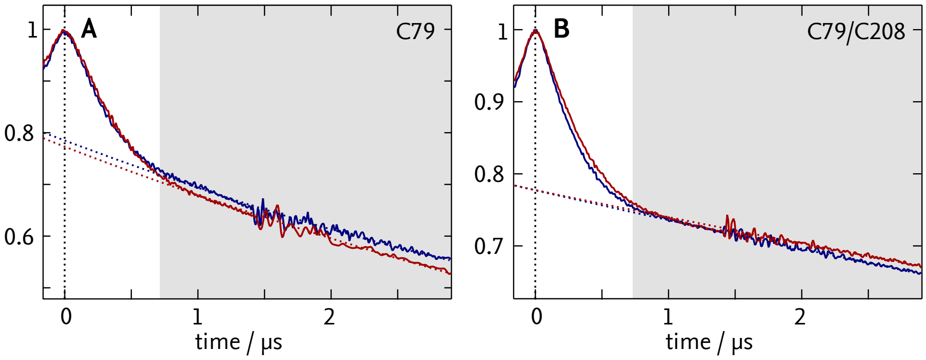

Figure 6.3. – **ELDOR data of spinlabelled ChR2 variants ChR2-C79 and ChR2-C79/C208**. Raw ELDOR measurements (solid lines) of dark/closed (blue) and light/open state (red) ChR2 are shown together with their respective background fits (dotted). The vertical dotted line indicates the zero position, the shaded, gray area indicates the part of the time trace that was used for background correction. Before further evaluation was performed, data was cut at the end of the background fit area, eliminating artefacts. The timetraces are the result of combining two measurements of different lengths as described in 5.1.2.

aggregation of the protein.

A direct comparison of these distances with the C1C2 crystal structure[90] is difficult, since C79 is situated in the part of the chimera protein taken from ChR1 (See Fig. 6.5). Additionally, it is the only fully resolved amino acid of the loop connecting helices A and B. Rotamer predictions using either structure are therefore bound to be imprecise. However, given this as well as potential differences arising from protein flexibility, the observed distance is still very well compatible with the 3.3 nm mean distance predicted by MMM.

Upon illumination, the low-noise section of the time trace clearly shows a slower signal decay in conjunction with a loss of visible oscillations (Fig. 6.4A, red), reflected in the distance data by a shift of the maximum by about 0.5 nm to 4.2 nm together with significant broadening (Fig. 6.4B, red). The observation of broadening of the distance is somewhat at odds with the previous finding that there are no significant changes in mobility upon illumination, since larger conformational freedom of the label at cryogenic temperatures is likely to correspond to higher mobility at room temperature. Distances beyond 5 nm are not changed by illumination, indicating that they indeed result from aggregation of the protein and not from an intra-protein C79–C79 interaction.

The dimeric arrangement of ChR2 yields four labels present in ChR2-C79/C208, with four inequivalent pair distances, severely complicating the interpretation of the distance data for this sample. However, a shift towards longer distances in

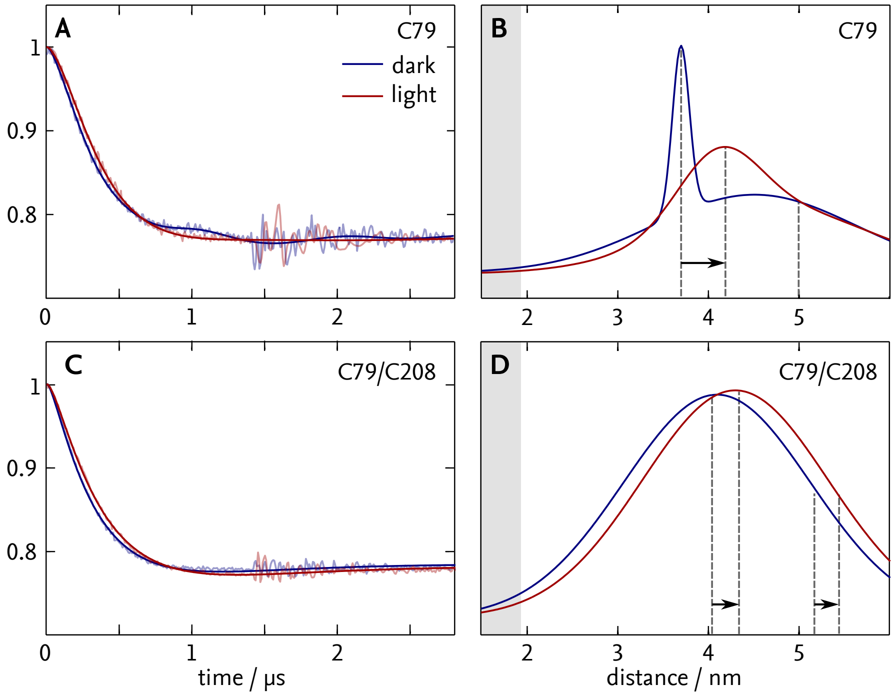

FIGURE 6.4. – **Dipolar evolution and distance distribution of ChR2-C79 (A, B) and ChR2-C79/C208 (C, D).** Left: Dipolar evolution data (shaded) and fit (solid). The modulation depth of the light state measurement (red) has been scaled to match that of the dark state (blue). Right: Distance distribution corresponding to the best fit (solid) as derived from a model of two Gaussians. The positions where artefacts from proton can appear are shaded gray. Both ChR2-C79 and ChR2-C79/C208 show a component shifting towards smaller frequencies and thus, larger distances, on top of a wide, unstructured and unchanging component.

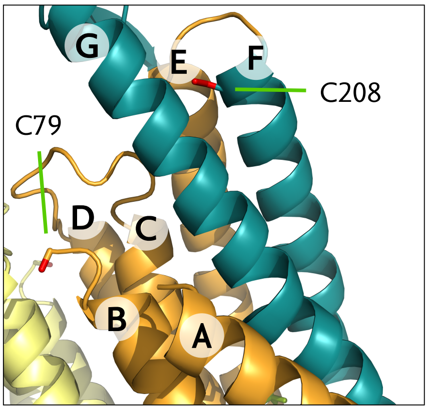

Figure 6.5. – **Label positions with respect to the C1C2 structure (pdb: 3UG9[90]).** Detailed view of the cytoplasmic side containing C79 and C208. C79 (residue 118 in C1C2) is situated in the ChR1 part (orange) ot the chimera protein, additionally it is the only resolved residue of the loop connecting helices A and B. C208 (residue 247 in C1C2) is situated directly at the connection between the ChR1 (orange) and ChR2 (blue) sections.

the lit state compared to the dark state is still clearly visible in the time trace (Fig. 6.4C). The oscillation visible in the data from the ChR2-C79 dark state is absent in ChR2-C79/C208. Correspondingly, the distance distributions are severely broadened (Fig. 6.4D, blue), with significant distance contributions already appearing around 2.5 nm as well as around 5 nm. Based on the C1C2 structure,[90] short distances around 2.5 nm are expected for the C79–C208 intra-monomer pair, while the long distances observed fit well with a inter-monomer C208-C208 distance. The inter-monomer C79–C208 distance is expected to be around 4 nm, overlaying the already identified C79–C79 distance. This overlap of distances, coupled with the likely presence, again, of aggregates, explains the lack of visible oscillations in the ChR2-C79/C208 data compared to ChR2-C79.

As was the case for ChR2-C79, illumination of the sample shifts the maximum of the distribution (by 0.4 nm) towards longer distances (Fig. 6.4D). Interestingly both the lower and upper inflection points of the distribution shift as well: The lower by about 0.15 nm, the upper by 0.2 nm. The global shift of the distribution is consistent with an increase of both the intra- and inter-monomer C79–C208 distance, as well as the inter-monomer C208-C208 distance.

**Comparing the Gaussian model to Tikhonov regularisation** The standard approach to ELDOR data analysis is Tikhonov regularisation. To motivate the choice of a Two-Gaussians model over the standard approach in this particular case, Fig. 6.6 shows the distance distribution derived from the ELDOR data by using Tik-

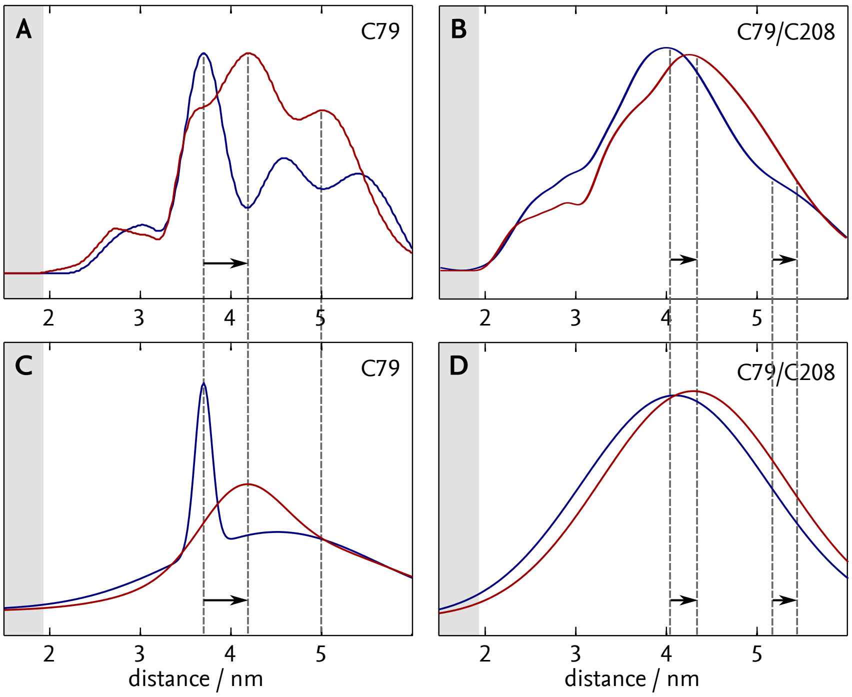

Figure 6.6. – **Distance distribution of ChR2-C79 (A, C) and ChR2-C79/C208 (B, D) derived from Tikhonov regularisation (top) and a Two-Gaussians model (bottom).** Both methods reflect the general features of the distribution equally well, however, the narrow individual Gaussians the Tikhonov fit is built from suggest a resolution not present in the data. C and D are taken from Fig. 6.4.

honov regularisation (A, B) with a regularisation parameter of 100, compared to the distribution resulting from the Two-Gaussian model at similar RMSD.

As can be seen from the dashed lines, the maxima of the distributions are quantitatively identical in both approaches, as well as the general shape of one narrow component that is broadened in the lit state plus a broad second component in the case of ChR2-C79, just one broad distribution in the case of ChR2-C79/C208. However, the distribution generated by Tikhonov regularisation is highly structured due to the relatively narrow constituent Gaussians. For ChR2-C79/C208, this tendency could be compensated by choosing the largest possible regularisation parameter that does not significantly impact the RMSD of the fit.

Crucially, this is not possible in the case of ChR2-C79, where a larger regularisation parameter would lead to artificial broadening of the narrow distance peak at 3.7 nm. The result is a distribution that, while correctly representing the narrow features, implies a resolution that is not present in the data.

Given this, the Two-Gaussians model is clearly superior to the Tikhonov ap-

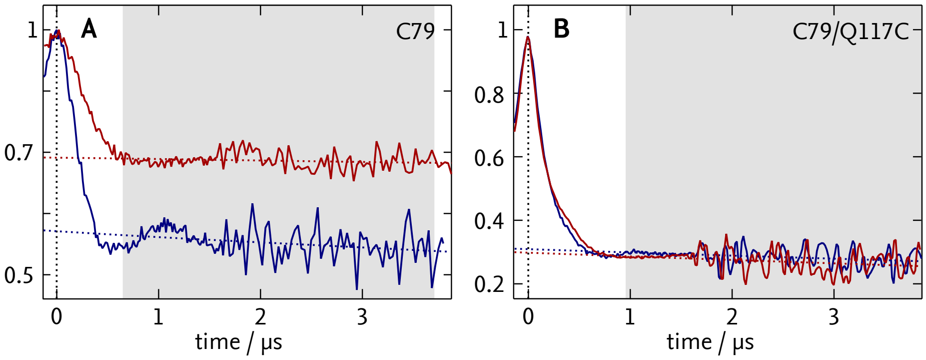

Figure 6.7. – **Raw ELDOR traces for ChR2-C79 (A) and ChR2-C79/Q117C (B) in nanodiscs.** The traces show very little background contributions for both dark (blue) and light (red) samples, indicating the absence of aggregates.

proach in describing the ChR2-C79 data. While Tikhonov regularisation with a large regularisation parameter could be employed in the case of ChR2-C79/C208, for direct comparability of the datasets, the same approach was used for both constructs.

### 6.1.2 Reducing the influence of protein aggregates

Clearly, one of the major issues with this data is that the distance distributions contain many contributions from unspecific aggregates, that not only greatly limit the structural information that can be extracted from the data, but also cause a faster spin relaxation as well as a more difficult background correction by effectively increasing the sample concentration. To preclude the formation of aggregates, ChR2 variants were reconstituted in nanodiscs.[158] The size of the discs was chosen so as to only accommodate a ChR2 dimer, the oligomeric state of the protein was verified by comparing the retinal content per nanodisc using UV/vis absorption spectroscopy.

**ChR2-C79 in nanodiscs** Figures 6.7A and 6.8A show ELDOR distance measurements of ChR2-C79 reconstituted in nanodiscs. A clear improvement over previous data is already apparent in the raw data (Fig. 6.7A), in that the timetrace shows very little background contribution, indicating a lower effective concentration due to a lack of aggregates. The virtually flat background makes background correction much less ambiguous even in the presence of larger distances.

The general tendencies that were observed in the detergent-solubilised samples, namely a distinct modulation in the dark state (Figure 6.8A, blue) that gets less pronounced in the lit state (6.8A, red), are present in the background-corrected traces

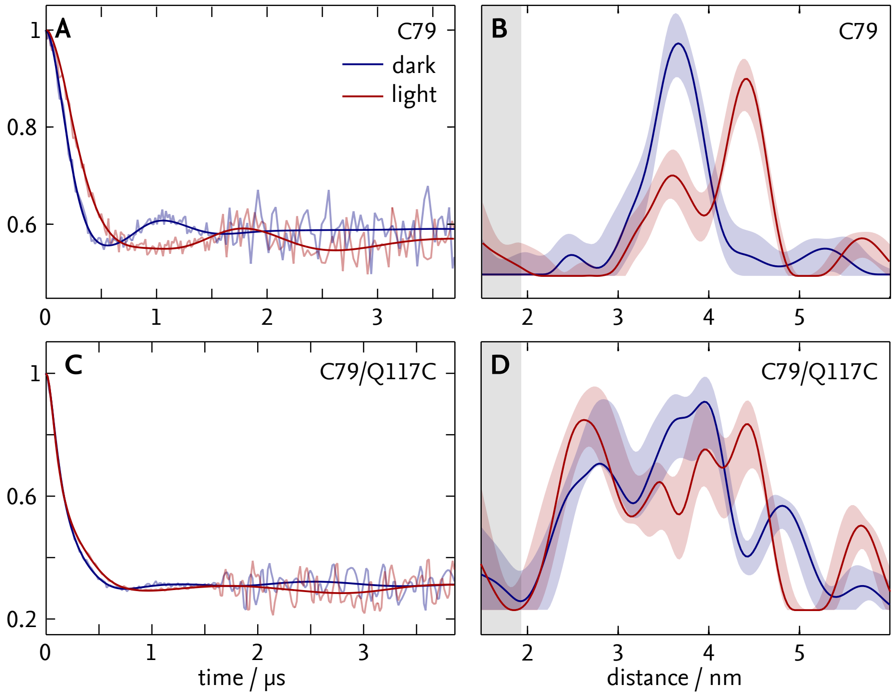

Figure 6.8. – **Form factor (left) and distance distributions (right) of ChR2-C79 (A,B) and ChR2-C79/Q117C (C,D) in nanodiscs.** Distinct modulations are visible in both states of ChR2-C79 (A), yielding fairly narrow distance distributions (B). The distance observed (B) for the dark state (blue) matches that observed previously (Figure 6.4). This distance shifts upon illumination (red), however, dark-state contributions are still visible. The modulation depth of the lit sample in A has been scaled to match that of the dark sample. ChR2-C79/Q117C shows less distinct modulations due to the dimeric nature of the protein (C). Accordingly, a broad distance distributions (D) is observed for both the dark (blue) and the light state (red). In addition to the distances from ChR2-C79, a short distance centred at 2.8 nm can be observed, that corresponds to the Q117C-Q117C distance and does not shift significantly upon illumination.

as well, however, compared to the previous measurements the loss of modulation is much less pronounced, with a distinct modulation, albeit at smaller frequency, being visible even in the lit state (6.7A, red). This, too, indicates that aggregates that significantly broaden the distance distribution and thus wash out the modulation, are no longer present in nanodisc-reconstituted samples. Accordingly, the distance distribution of the dark state consists of only one significant, narrow distance peak centred at 3.6 nm (Figure 6.8B, blue).

Upon illumination, a second peak appears in the distribution at 4.4 nm (Figure 6.8B, red). An additional small peak at 5.8 nm corresponds to a modulation period identical to the length of the time trace and is thus most likely a typical Tikhonov artefact due to incomplete background correction.

Interestingly, the peak at 3.6 nm remains present but is less pronounced. This indicates that part of the sample even under saturating illumination conditions remains in the dark state, at least in terms of the structural changes observable at cysteine 79. Thus, the broadening effect that was observed in the earlier measurement is not due to a broadening of the spin label's conformational space, but rather to an unresolved mixture of dark and light state structures, bringing the ELDOR results again in line with those from room temperature cw EPR. An incomplete illumination is also compatible with data obtained from UV/vis spectra[A]. Unfortunately, it is not possible to reliably quantify the fraction of ChR2 in $P_3^{520}$ using optical absorption spectroscopy, since its spectrum overlaps strongly with that of the dark state. Here, the ELDOR data offer a helpful tool for ascertaining the illumination status of the sample.

In the case of incomplete illumination of a ChR2 dimer, three different distances are to be expected, the *fully dark* distance (both monomers in the dark conformation), the *fully lit* distance (both monomers in the light conformation) as well as a the *half lit* distance (one monomer in the dark, the other in the light conformation). Interestingly, the observed distribution appears to be purely bimodal, with relative intensities of 35 % and 65 % (measured as the integral intensity from 2.8–3.9 nm and 3.9–5.0 nm) between dark and light conformations, respectively, hinting at a potential cooperative behaviour of the ChR2 monomers, as has been reported for BR.[159–161] An alternate explanation would be that a fraction of ChR2 in the sample is non-functional and thus does not undergo any structural changes upon illumination.

**ChR2-C79/Q117C in nanodiscs** The raw ELDOR data of nanodisc-reconstituted ChR2-C79/Q117C also shows very little contribution from background spins (Figure 6.7B). The background-corrected timetrace of dark-state ChR2-C79/Q117C (Fig. 6.8C, blue) shows a distinctly more rapid initial decay than the corresponding trace

---

[A] Experiments performed by Nils Krause in Dr. Ramona Schlesinger's group of ChR2-C79 (Fig. 6.8A). While a shift towards smaller frequencies and therefore longer distances is visible in the light-state trace as well (Fig. 6.8C, red), the initial decay remains unchanged. Tikhonov regularisation yields a short distance between 2.6–3.0 nm in the dark state (Fig. 6.8D, blue) that shifts only very slightly towards smaller distances upon illumination (Fig. 6.8D, red), consistent with a Q117–Q117 distance, predicted from the C1C2 structure to be 2.7 nm. Due to the dimeric nature of ChR2, the distribution is - as in the case of ChR2-C79/C208 - very broad. However, the previously assigned C79–C79 distance can be identified in both the dark (3.6 nm) and the light (4.4 nm) state. Additional contributions around 3.9 nm in both the dark and the light state match very well the C79–Q117C distance of 3.8 nm as predicted from the C1C2 structure. Again, some fraction of uncorrected long-range interactions give rise to a peak at 5.8 nm. Interestingly, a distance peak also appears at 4.8 nm in the dark state that disappears or becomes part of the long-distance artefact in the light state. This peak is incompatible with any intra-dimer distance involving C79 and Q117C and is thus most likely due to either inter-dimer distances or a degenerated protein. However, absent long time traces with better signal to noise, a clear assignment of this distance is not possible.

### 6.1.3 The structure of the $P_3^{520}$ state of ChR2

The increases in the C208–C208 and C79–C208 distances observed in ChR2-C79/C208 point towards an outward movement of helix F, in agreement with previous EPR results from BR and sensory rhodopsin II (SRII).[100–102] The distance that could be assigned to Q117C–Q117C in ChR2-C79/Q117C does not change from the closed to the open state of ChR2, indicating that the extracellular side of helix C does not undergo a conformational change. The crystal structure of the C1C2 protein[90] indicates that helix F, and therefore the label at cysteine 208, is located remote from the dimerisation interface (see Fig. 6.1). Movements of helix F should therefore only influence distances involving C208. Contrary to that, ELDOR data from ChR2-C79 indicate an unambiguous change of the C79–C79 distance. Therefore, the structural change cannot be limited to helix F, but has to involve either the dimerisation interface or helix B as well. 2D diffraction experiments using neutrons,[162] X-rays[163–165] as well as electrons[166] have demonstrated a movement of helix B in BR in purple membranes. The ELDOR experiments indicate that, even though the arrangement of the TM helices in ChR2 is different than that of other microbial rhodopsins (See Chapter 3), the changes in the tertiary structure between the closed and the open state seem to be largely conserved.

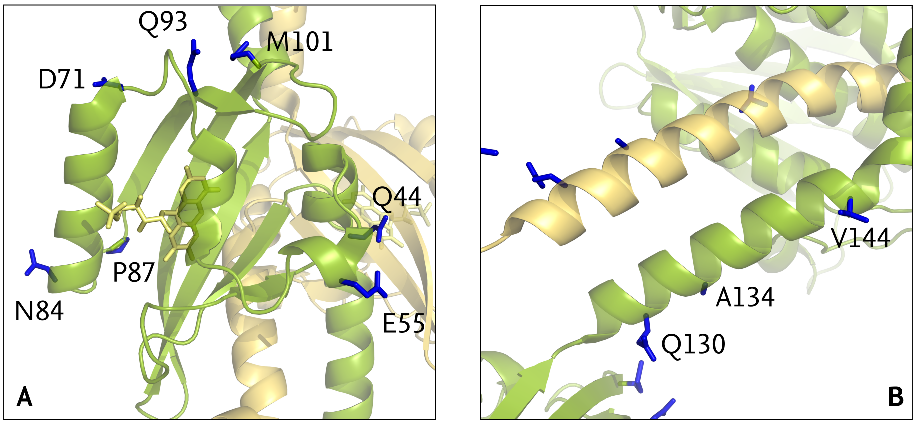

Figure 6.9. – **Labelling positions in YF1 (pdb: 4GCZ[9]).** Seven positions in the LOV domain, M101, Q93, P87, N84, D71, E55 and Q44 (A) within or surrounding the β-sheet and three positions in the linker, V144, A134, Q130 (B), were chosen. All targeted amino acids marked in blue.

## 6.2 Structural changes upon light activation of YF1 investigated by SDSL and ELDOR

To address an important question about the signalling mechanism of LOV photosensor proteins, namely, how the structural changes induced by photoexcitation of the flavin chromophore can be transmitted from the LOV to coupled effector domains, structural changes were investigated using SDSL and ELDOR.

For the investigation of structural changes between the active (light) and inactive (dark) state of YF1, two groups of residues were targeted for SDSL. One group, residues Q44, E55, D71, N84, P87, Q93 and M101, mapping the conformation of the YF1 LOV-domain, especially the β-sheet's structure around the beginning of the coiled-coil helix connecting LOV and kinase domain (Figure 6.9A), and the second, residues Q130, A134 and V144, along the coiled-coil linker itself (Figure 6.9B). Positions were chosen based on the projected accessibility to spin labels, favourable distances and closeness to regions of interest. Due to the dimeric nature of YF1, the variants contain each residue twice, causing a variant with a single cysteine-exchanged residue to be doubly labelled. To avoid the additional complexity of multi-spin distance measurements, only single-cysteine variants were produced.

All mutants retained their functionality *in vivo*. After labelling, variant Q93C remained in an always active state independent of illumination, while Q130C remained inactive. The other variants were functional even after labelling, albeit at a reduced activity in the case of A134C.

ELDOR experiments on the dark and illuminated state of each variant were per-

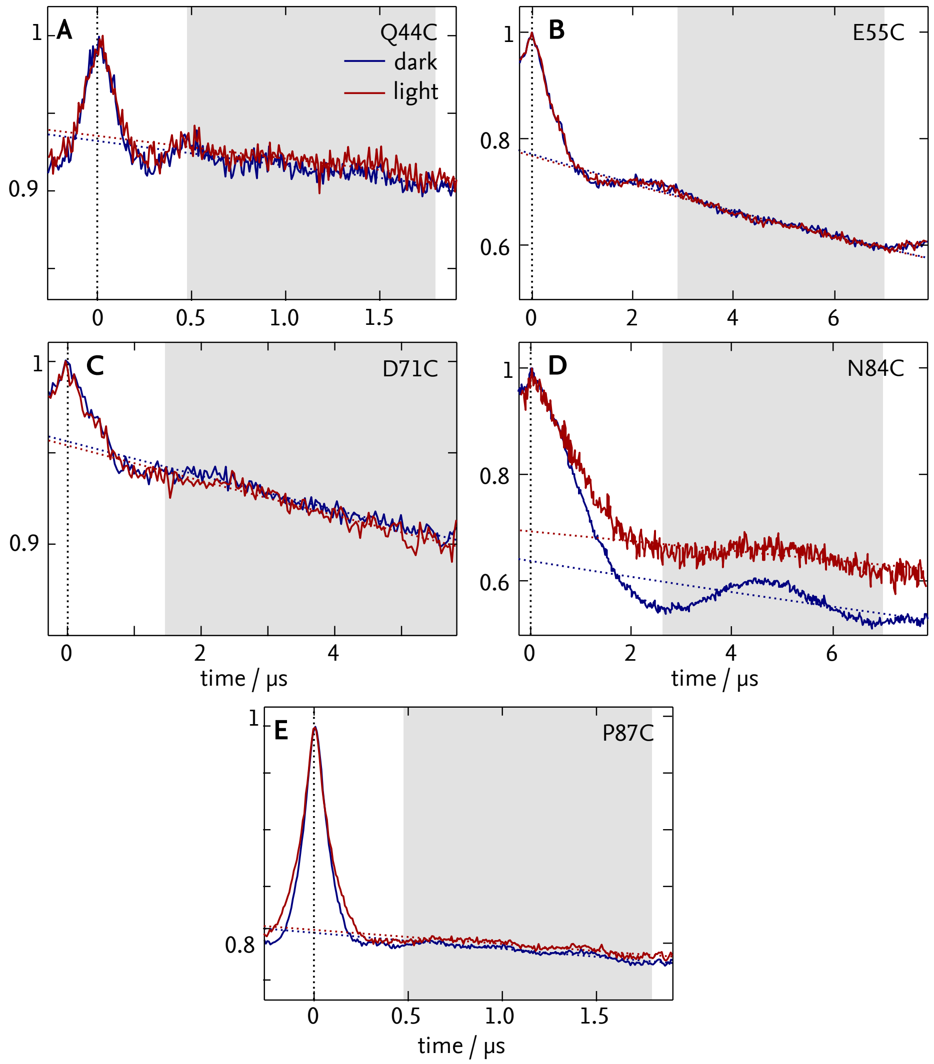

Figure 6.10. – **ELDOR data of spin-labelled YF1 variants Q44C, E55C, D71C, N84C and P87C.** Raw ELDOR measurements (solid lines) of dark (blue) and light state (red) YF1 are shown together with their respective background fits (dotted). The vertical dotted line indicates the zero position, the shaded, gray area indicates the part of the time trace that was used for background correction. Before further evaluation was performed, data was cut at the end of the background fit area, eliminating artefacts.

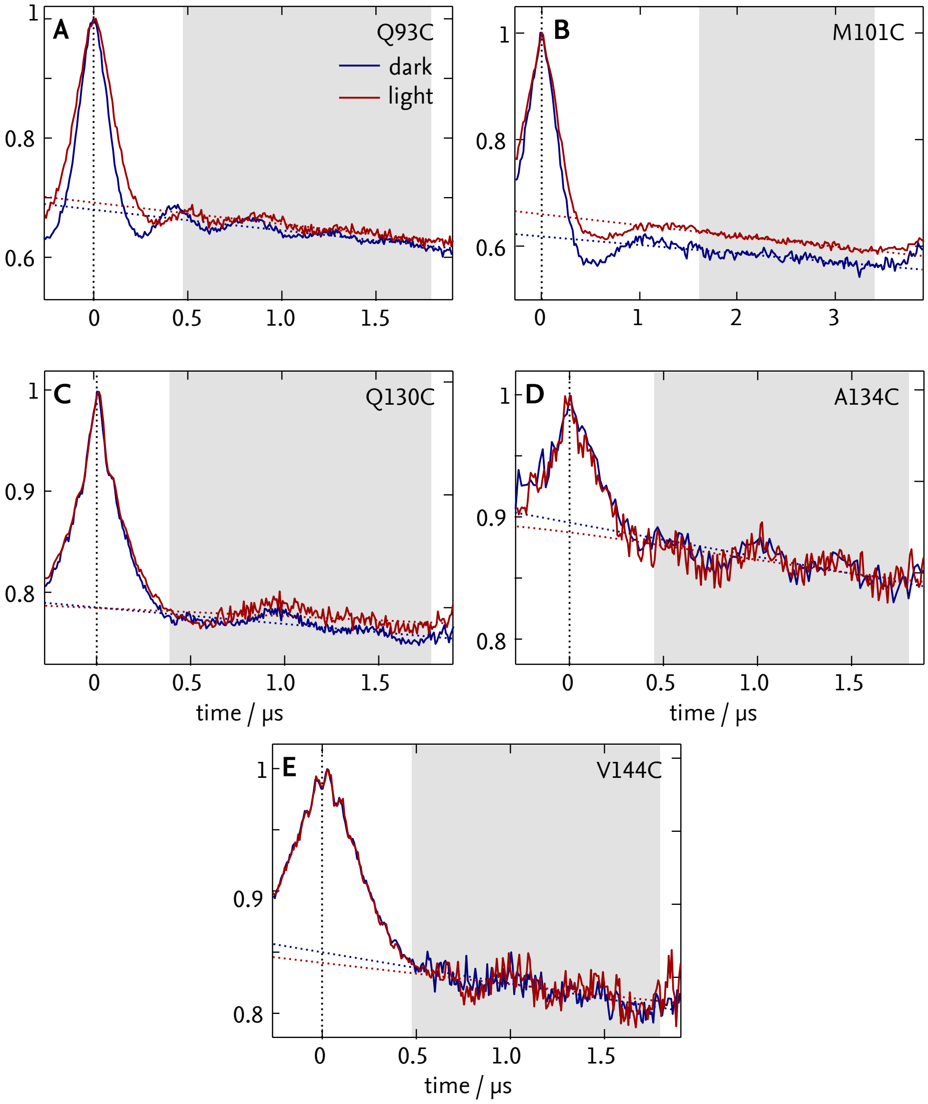

Figure 6.11. – **ELDOR data of spin-labelled YF1 variants Q93C, M101C, Q130C, A134C and V144C**. For a detailed description see Fig. 6.10. The V144C and Q130C time traces are the result of combined datasets (see Section 5.1.2).

TABLE 6.2. – **YF1 variants investigated using ELDOR.** Four residues inside the LOV domain close to the linker, and three inside the linker itself were chosen for SDSL.

| Protein | Variant | Functional | Location |
|---|---|---|---|
| YF1 | Q44C | fully | LOV-domain |
| | E55C | fully | LOV-domain |
| | D71C | fully | LOV-domain |
| | N84C | fully | LOV-domain |
| | P87C | fully | LOV-domain |
| | Q93C | only unlabelled | LOV-domain |
| | M101C | fully | LOV-domain |
| | Q130C | only unlabelled | Linker |
| | A134C | partly when labelled | Linker |
| | V144C | fully | Linker |

formed as described (Section 5.1.2, p. 48), the resulting time traces are shown in Fig. 6.10 and 6.11. The maximum achievable time trace length varied greatly between samples, due to the varying impact the deuterated buffer had on the sample's $T_2$ relaxation time, with the most exposed positions E55 (Fig. 6.10B), D71 (Fig. 6.10C), N84 (Fig. 6.10D) and M101 (Fig. 6.11B) yielding traces of up to 4–8 µs, while the remaining samples were limited to 2 µs traces (Fig. 6.10A and E, Fig. 6.11A, C–E). For V144C (Fig. 6.11E) and Q130 (Fig. 6.11C), a 2 µs trace was combined with a 0.8 µs one as described in Section 5.1.2. Regardless, for all samples but N84C (Fig. 6.10D), the time traces were long enough to allow a reliable background fit (Fig. 6.10 and 6.11, dotted lines).

### 6.2.1 ELDOR MEASUREMENTS REVEAL STRUCTURAL CHANGES IN THE LIT STATE OF YF1

The dipolar evolution functions obtained after background corrections as well as the resulting distance distributions are shown in Fig. 6.12–6.14, in the left and right column, respectively. In all cases, a good fit (left hand columns, solid lines) of the data (shaded lines) could be obtained. The solid lines represent in all plots of the distance distributions (right hand columns) the best fit of the data, while the shaded area plots indicate error estimates.

**Labels in the N-terminal region of the LOV domain** In the dark state, the traces of labels situated on the N-terminal side of the LOV domains, Q44C, E55C, N84C

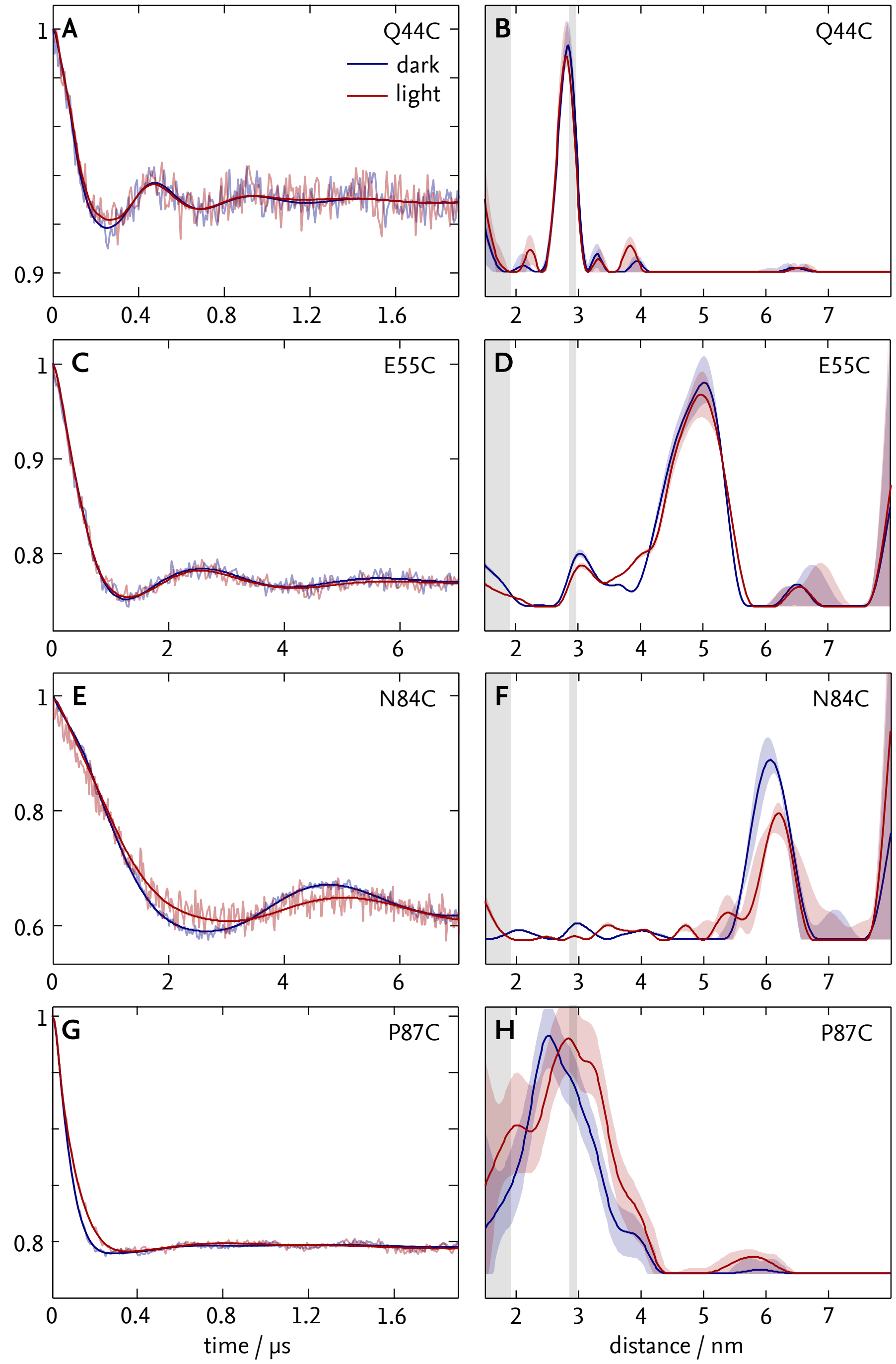

FIGURE 6.12. – **Dipolar evolution and distance distribution of YF1 Q44C (A, B), E55C (C, D), N84C (E, F) and P87C (G, H).** Left: Dipolar evolution data (shaded) and fit (solid). The modulation depth of the light state measurement (red) has been scaled to match that of the dark state (blue). Right: Distance distribution corresponding to the best fit (solid) with error estimate (shaded). The positions where artefacts from proton and deuteron nuclear modulations can appear are shaded gray. Q44C and E55C show no significant change upon illumination, N84C and P87C exhibit a distinct shift towards smaller frequencies and, correspondingly, distances.

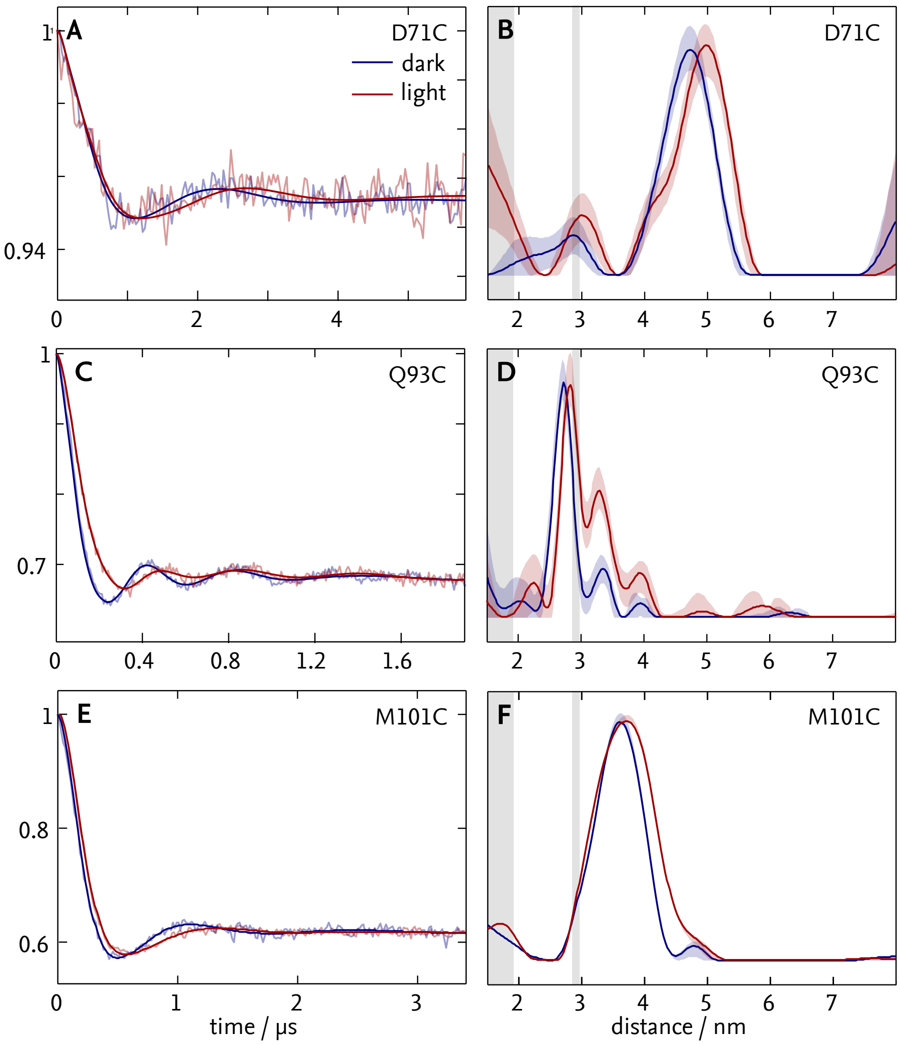

FIGURE 6.13. – **Dipolar evolution (left) and distance distribution (right) of YF1 D71C (A, B), Q93C (C, D) and M101C (E, F).** Data presented as in Fig. 6.12. All three variants exhibit a distinct shift towards smaller frequencies and, correspondingly, distances.

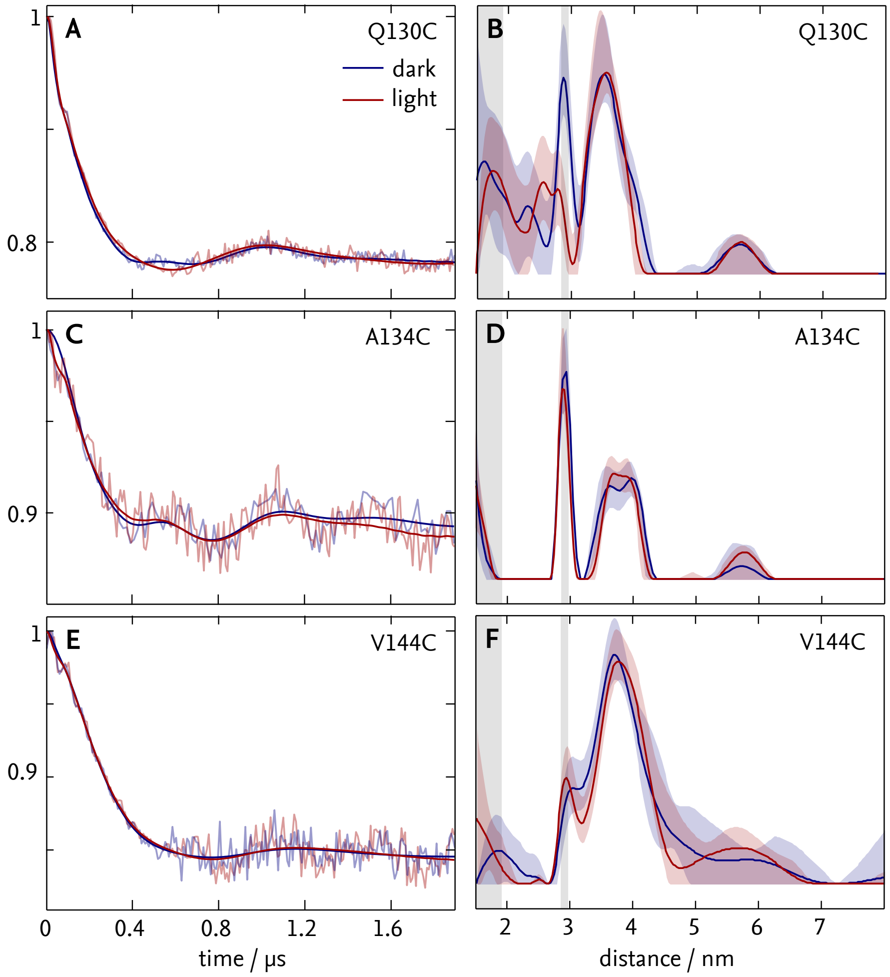

Figure 6.14. – **Dipolar evolution (left) and distance distribution (right) of YF1 Q130C (A, B), A134C (C, D) and V144C (E, F).** Data presented as in Fig. 6.12. Time traces of A134C and V144C are strongly impacted by proton and deuteron nuclear modulations (shaded gray), All three variants show a dominant distance at around 3.8 nm that is unchanged by illumination.

(Fig. 6.12A, C and E, blue) show a distinct modulation, yielding a single dominant and fairly narrow distance peak, centred at 2.8 nm (Q44C, 6.12 B, blue line), 5.0 nm (E55C, D) and 6.1 nm (N84C, F). P87C, while showing a less distinct modulation (D) and correspondingly a broader distance distribution, still yields a single dominant distance centred at 2.7 nm. This result is expected for samples containing a single pair of labels and indicates that the protein is present in only a single conformation in the dark state.

Blue light illumination yields no significant change in the distance distributions of Q44C (A and B, red lines) and E55C (C and D). Both N84C (E and F) and P87C (G and H), however, show a clear shift of the dominant peak towards larger distances – 0.1 nm and 0.3 nm for N84C and P87C, respectively – in the lit state relative to the dark state. This shift towards smaller frequencies is already apparent in the time traces of these samples, a clear indication of structural changes in the protein. Since no change can be observed for Q44C and E55C, situated closest to the N-terminus, this could indicate that only the C-terminal side of the LOV-LOV-dimer moves upon illumination.

**Labels in the C-terminal region of the LOV domain** The labels situated in the C-terminal part of the LOV domain, D71C, Q93C and M101C (Fig. 6.13A, C and E, blue lines) show distinct modulations, yielding distances of 4.7 nm (D71C, B), 2.7 nm (Q93C, D) and 3.6 nm (M101, F). The D71C measurement suffers from much worse SNR compared to the other two, giving rise to spurious distance contributions below 3.5 nm, as the intensity of deuteron and proton nuclear modulations (indicated by gray shaded areas) increases relative to that of the dipolar coupling.

All three samples show a shift of the distance distributions towards larger distances in the lit state (red lines). While D71C shows a shift of 0.2 nm without significant changes in the distribution's shape (B), both Q93 (D) and M101 (F) show a shift of both the average distance (by about 0.5 nm and 0.1 nm for Q93 and M101, respectively) and the distribution's width. Greater conformational freedom leading to widened distance distributions could indicate that these two labels are situated in a region were the conformational changes occur, as opposed to an inert region of the LOV domain that just alters its mean distance from the second monomer due to conformational changes elsewhere. In Q93C in particular, the change is accompanied by the appearance of additional structure, yielding a strongly non-Gaussian shape that could indicate a label that is locked into a few distinct conformations by the surrounding residues.

**Labels in the linker** Measurements of label Q130C in the linker region shows good SNR (Fig. 6.14, A) but a rather broad distance distribution, with distance contributions covering 1.5–4.2 nm (Fig. 6.14, B). A134C and V144C in the linker region suffer from poor SNR and, consequently, from artefacts arising due to proton and deuteron nuclear modulations in the time traces (Fig. 6.14, C and E). The associated distance peaks are especially apparent in the distance distribution of A134C (D, shaded gray). Nonetheless, in all three samples, dominant distances of 3.7 nm, 3.8 nm and 3.7 nm for Q130C (B), A134C (D) and V144C (F), respectively, can be identified. These distances do not change significantly upon blue-light illumination.

### 6.2.2 Relating interspin distances to structure

To relate the observed distance changes to specific structural changes of the LOV domains, the spin label conformations were simulated in the dark-state crystal structure of YF1 (pdb code 4GCZ[9]) using both the MD-based rotamer library approach implemented in MMM[138] (library approach) and the approach of filtering van-der-Waals (vdW) clashes from the total conformational space employed by MtsslWizard[139] (geometric approach). To ensure a maximal set of conformations, i.e. the broadest possible distribution, in the geometric approach, the constraints were set to “loose”, implying a vdW cutoff of 0.25 nm with 5 allowed clashes with the protein to take into account the protein flexibility not represented in the crystal structure. Figures 6.15 and 6.16 show the comparison of the measured distance distributions (blue) of the dark state to the simulations in the geometric approach (black, dotted) and rotamer approach (black, dashed).

In general, the library approach yielded narrower and more structured distribution simulations than the geometric approach, due to the restriction to a set of 120 rotamers as well as the weighting of individual rotamer conformations. Since such detailed structure can seldom be reliably extracted from ELDOR data, either because of uncertainties in the crystal structure or because of the ever-present flexibility of the spin label’s surrounding residues, the geometric approach in general can be considered a safer choice. As can be seen throughout Fig. 6.15 and 6.16, the geometric approach in general, while mostly overestimating the width of the distribution, matched the measured distributions better than the rotamer approach.

**Labels inside the LOV domain** Of the seven label pairs located in the LOV domains investigated, in all but P87C (Fig. 6.15E) and Q93C (Fig. 6.16A) both simulation approaches matched the measured distribution well, either directly in the case of N84C (Fig. 6.15D) or assuming the observed label distribution to be a subset of the simulated one in the case of Q44C (Fig. 6.15A), E55C (Fig. 6.15B), D71C (Fig. 6.15C) and M101C (Fig. 6.16B). Both the simulated distribution of P87C (Fig. 6.15E) and of Q93C (Fig. 6.16A) are shifted towards longer distances by about 1 nm and 1.3 nm, respectively. While there is still significant overlap between the distributions in the case of P87C, this is not the case for Q93C. For both, this indicates a

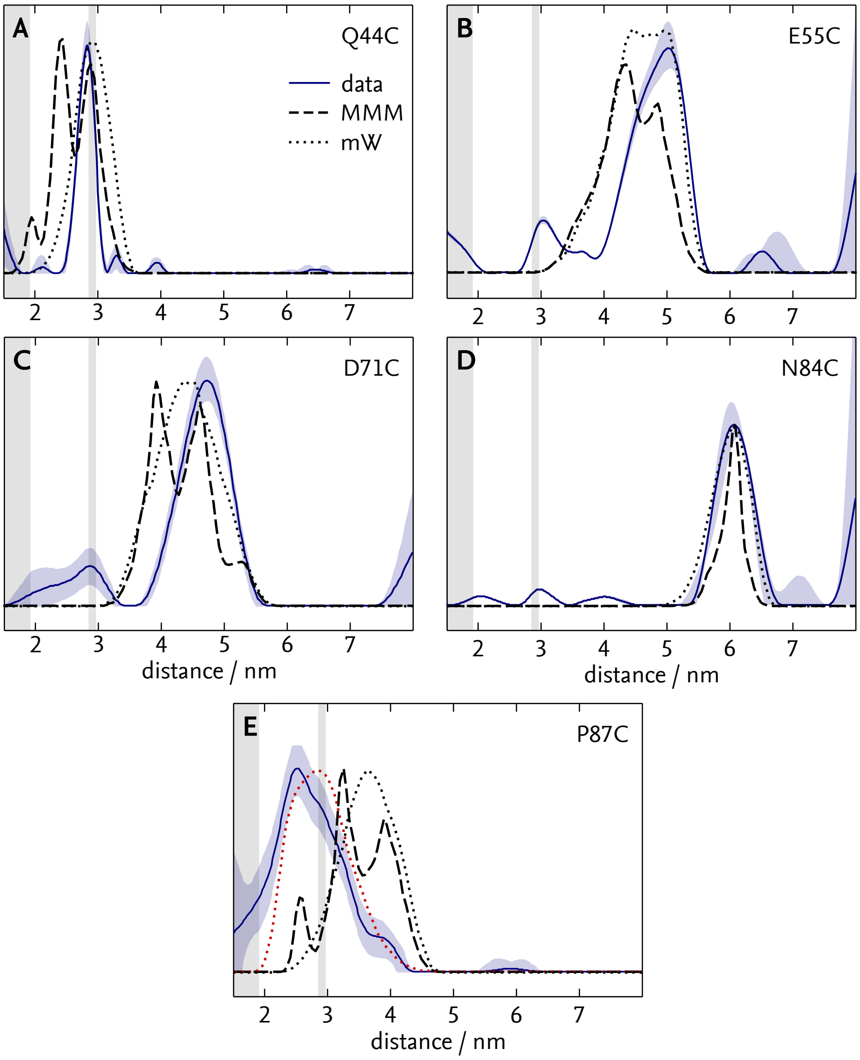

Figure 6.15. – **Distance distributions measured by ELDOR (blue) vs. simulated via MMM rotamer library (black, dashed) and purely by van-der-Waals clashes in MtsslWizard (black, dotted).** For Q44C (A), E55C (B), D71C (C) and N84C (D), the simulation purely by vdW clashes matches the observed distribution very well, assuming that the real rotamer distribution is a subset of the maximal conformation set generated by MtsslWizard. The measured distribution of P87C (E) deviates significantly from the simulation, however, it can still be represented by a – albeit small – subset of the total rotamer population (red, dotted).

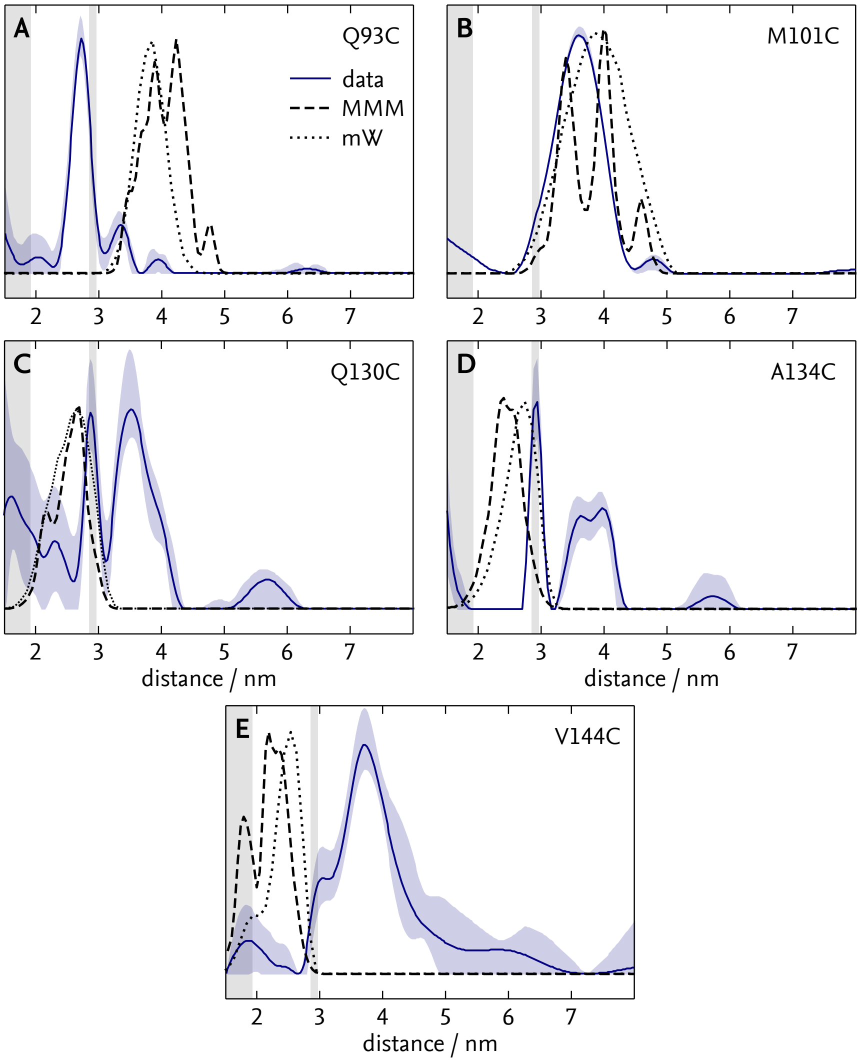

FIGURE 6.16. – **Distance distributions measured by ELDOR (blue) vs. simulated via MMM rotamer library (black, dashed) and purely by van-der-Waals clashes in MtsslWizard (black, dotted).** Only the simulated M101 distance distributions match the data well (B), the Q93C distance is too large by 1.3 nm (A), while Q130C, A134C and V144C are too short by about 1.5 nm (C-E).

deviation of the YF1 structure a crystal from that of the protein in frozen buffer solution.

**Labels inside the linker** For all three label pairs inside the linker, the simulated distance distributions in both the library and the geometric approach are wholly incompatible with the measured data, with simulated distances being shorter by at least 1 nm (Fig. 6.16C-E), again indicating a deviation of the crystal structure from the solubilised protein. Moreover, the observed distances are, at 3.7 nm, 3.8 nm and 3.7 nm for Q130C, A134C and V144C, respectively, incompatible with the maximum label distance obtainable in a coiled-coil helical structure (less than 3 nm) in general. This, together with the fact that both Q130C and A134C had no or impaired function after labelling (see Table 6.2), leads to the conclusion that attaching labels in these positions disrupts the structure of YF1, destroying the linker. The same is true for Q93C, since this variant was also functionally impaired after labelling. Strikingly, the measured distances in V144C indicate that this variant shares the disrupted structure of Q130C and A134C, while still being functional after labelling. The likely explanation here is that this position, situated very close to the histidine kinase domains, is only accessible to labelling in the structurally compromised conformation, effectively eliminating the functional fraction of the protein from the ELDOR data.

Leaving the positions that clearly disrupted the proteins structure aside, the crystal structure appears to match the observed distances very well, with the only indication of a difference between crystal and solubilised structure being P87 in the loop linking the α-helix containing N84 to the β-sheet.

Summarising the ELDOR results, the positions examined can be separated into three groups, highlighted in the structure in Fig. 6.17:

1. labels that impair the function of the protein and/or strongly disturb its structure (Q93C, Q130C, A134C and V144C) (red),
2. label positions that shift towards longer distances upon blue-light illumination (D71, N84, P87, M101) (green),
3. label position where illumination induces no changes (Q44 and E55) (blue).

From this, a rough model of the conformational change can be generated, wherein the N-terminus of the LOV-LOV dimer remains fixed, while the β-sheets as well as the helix containing N84 tilt outwards in their entirety.

### 6.2.3 STRUCTURAL MODELS DERIVED FROM MEASURED CONSTRAINTS

For a more detailed description of the conformational changes induced by the illumination of YF1, the structure of the lit state of the protein was modelled using the

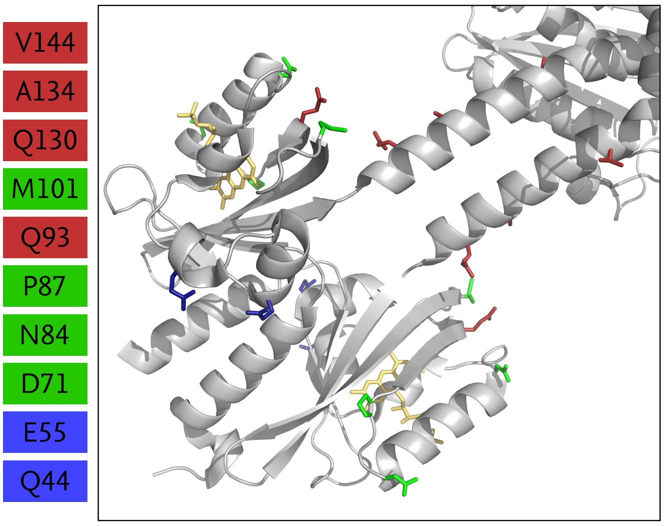

FIGURE 6.17. – **YF1 structure with the investigated labels attached, colour-coded by group**: Label positions that impair the function of the protein and likely disturb the coiled-coil linker (red), label positions where a shift towards longer distances could be observed in the lit state (green) and label positions where no change upon illumination was observed (blue).

distances obtained via ELDOR as constraints for the modelling algorithms. Since the changes observed are small and the number of available constraints limited, methods must be found to evaluate whether or not the model obtained algorithmically is actually relevant to the real structure. One way to address this problem is to use multiple modelling approaches and parameters consecutively, looking for structural motifs that are consistent through all models.

In this work both an ENM (Models ENM-<...>), implemented in MMM[138] (see Section 5.1.5), and constrained RBD (Models RBD-<...>), implemented in mtsslDock,[156] were used. As constraints for the fit, the average distances of each of the six label pairs in group (2) and (3) above were used, i.e. labels that were shown to disturb the structure were excluded. Since it is not entirely clear whether the deviation between simulated and measured differences in P87C is due to a real difference between the structure of wt protein in a crystal and in frozen solution, or due to a structural change induced by the labelling process, each model was run both with (<model>-all) and without (<model>-no87) the P87C–P87C label distance as a constraint. Moreover, to prevent any general deviations between modelled and measured distances from being incorporated into the conformation of the light state, each model was run both with light state and with dark state distance constraints. This approach has two beneficial effects; one, the overall quality of the fit can be judged from the deviation of the dark state model from the

Table 6.3. – **Constraints used for modelling.** Errors given are relative to each other. The lower set of constraints, involving A134C, V144C and H145C, were used only in the RBD model and are derived from the crystal structure.

| Label pair | distance (nm) | | error (nm) |
|---|---|---|---|
| | dark state | light state | |
| Q44C–Q44C | 2.85 | 2.85 | 0.30 |
| E55C–E55C | 5.05 | 5.05 | 0.40 |
| D71C–D71C | 4.75 | 5.00 | 0.30 |
| N84C–N84C | 6.10 | 6.20 | 0.40 |
| P87C–P87C | 2.75 | 3.05 | 0.20 |
| M101C–M101C | 3.60 | 3.75 | 0.20 |
| A134C–A134C | 2.45 | 2.45 | 0.20 |
| V144C–H145C | 2.60 | 2.60 | 0.20 |
| H145C–V144C | 2.45 | 2.45 | 0.20 |
| V144C–V144C | 2.60 | 2.60 | 0.20 |
| H145C–H145C | 2.05 | 2.05 | 0.20 |

crystal structure and two, by comparing the modelled light state to the modelled dark state instead of the crystal structure, any residual deviations of the simulated distances from the measured are filtered out, leaving only changes related to actual changes observed in the distance distribution data.

For the ENM, the crystal structure was cut off at residue I126 at the beginning of the linker, since in the absence of constraints in either the linker and the histidine kinase domains, transversal modes of the entire dimer along the linker tended to dominate the fit. Apart from this, the crystal structure was used as-is. Constraints for both the dark state and the light state model are given in the top half of Table 6.3.

The rigid-body docking proved to be more complex. Firstly, the model as implemented in mtsslDock comprises an evolutionary algorithm to perform the docking. Thus, identical constraints do not lead to identical results in consecutive runs. To ensure a reliable model, 50 consecutive runs were performed for each parameter set and then scored. The experimental constraints were identical to those used for the ENM, given in Table 6.3, top half.

Since the algorithm proved unable to reproduce the docking interface of the full dimer, the crystal structure was again cut, this time at the top of the linker at residue H145, with one LOV+linker monomer being docked to the other. To filter out results with an improper orientation of the two domains, additional constraints, derived from labels simulated into the crystal structure, were introduced

Table 6.4. – **RMSD of the modelled YF1 structures with respect to the crystal structure and measured constraints**. Models are named for their parameters: ENM/RBD = model type, all = all constraints, no87 = without constraints on P87C distance, dark/light = illumination state. RMSD was calculated both with and without the deviation of the P87 distance taken into account.

| Name | RMSD (nm) with respect to | | |
|---|---|---|---|
| | crystal structure | distance constraints | |
| | | with | without |
| | | P87 distance | |
| ENM-all-dark | 0.30 | — | — |
| ENM-no87-dark | 0.40 | — | — |
| RBD-all-dark | 0.33 | — | — |
| RBD-no87-dark | 0.32 | — | — |
| ENM-all-light | — | 0.27 | 0.24 |
| ENM-no87-light | — | 0.34 | 0.14 |
| RBD-all-light | — | 0.33 | 0.27 |
| RBD-no87-light | — | 0.38 | 0.22 |

into the model (Table 6.3, bottom half). The resulting models were scored by the RMSD of all constraints, with the measured constraints given twice the weight of the crystal-structure-derived.

**Dark-state models** Overall, the different models of the dark state represented the crystal structure about equally well (Table 6.4, second column), with RMSD values of around 0.3 nm. Only ENM-no87 with a RMSD of 0.4 nm showed a significantly higher deviation relative to the crystal structure. Interestingly, including the P87C–P87C distance did not increase the RMSD to the crystal structure compared to models excluding it. In fact, the structure of ENM-all (Figure 6.18) shows that the changes with respect to the crystal structure are mainly limited to the outer helix and the loop region, containing P87, that connects it to the β-sheet. It is unclear why ENM-no87, the constraints of which are actually closer to the crystal structure than ENM-all, fared so much worse. One possible explanation is that, given the sparsity of constraints in general, the reduced number of constraints in this model outweighs the advantage gained by the smaller discrepancies between measured and simulated constraints.

**Light-state models** As a consistency check, the deviations of the light structures from the measured constraints have been calculated for all models both with (Table

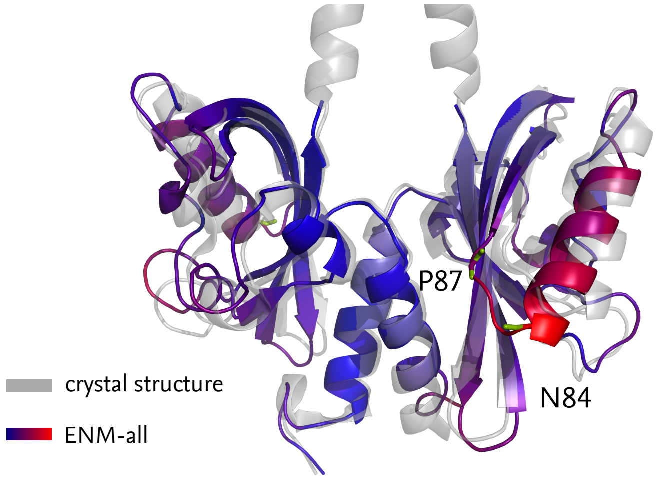

Figure 6.18. – **The RMSD of the full ENM model (color) relative to the crystal structure (gray).** Blue indicates lower, red higher RMSD values. The deviations are mainly limited to the outer $\alpha$-helix and the loop connecting it to the $\beta$-sheet, near P87 and N84, marked green.

6.4, column 3) and without (column 4) the P87C–P87C distance included. Unsurprisingly, in the former case better RMSD values were produced by models that included this distance in their constraints than those that did not, while the reverse was true in the latter case. In both cases, the ENM models fared significantly better (RMSD of 0.27 nm and 0.14 nm for ENM-all-light and ENM-no87-light, respectively) than their RBD counterparts (RMSD of 0.33 nm and 0.20 nm for RBD-all-light and RBD-no87-light, respectively). This indicates that the structural change upon illumination is not adequately described exclusively by a movement of the two monomers' LOV domains with respect to each other, but based on a conformational change of the individual LOV domains.

Comparing the simulated light state structures (Figure 6.19 A-D, red) to their corresponding dark state structures (blue), a variable shift outwards of the point where the LOV domains connect to the linker can be identified. This shift is present in all models to varying degrees, with RBD-all predicting the smallest shift of 0.17 nm (Figure 6.19A) and RBD-no87 predicting the largest shift (0.31 nm) (C). The ENM-based models yield shifts of 0.19 nm and 0.27 nm for ENM-no87 (D) and ENM-all (B), respectively.

### 6.2.4 A model for the signal transduction mechanism of LOV domains

There are four main conclusions that can be drawn from the data presented so far:

1. While some residues located in the linker can be replaced without issue, the

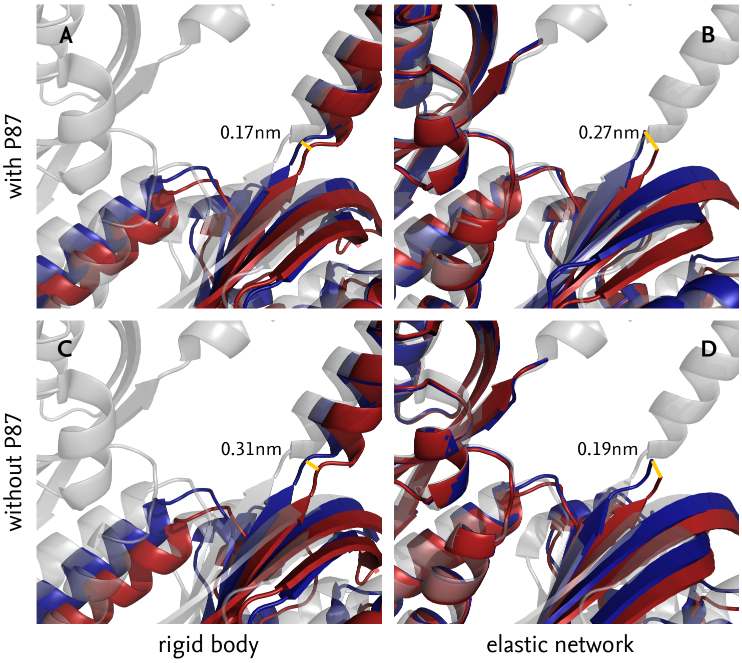

FIGURE 6.19. – **Structures of the YF1 dark (blue) and light (red) state.** A-D, structures derived from ENM and RBD models, including and excluding the P87 constraint. Shown in gray is the crystal structure.

act of attaching labels to the linker connecting sensor and effector domains significantly disrupts the structure and function of the protein, emphasising the critical role the linker plays in signal transduction,

2. the observed changes in distance distributions are limited to labels situated in the C-terminal side of the LOV dimer, implying that changes in the protein conformation are limited to this region as well, while the N-terminus remains fixed,

3. light state structure obtained with models that include protein flexibility (ENM-all and ENM-no87) have lower RMSD from the measured constraints than their rigid-body counterparts, indicating a conformational change within the LOV domain that is inadequately described by rigid-body docking,

4. all simulations, regardless of the model or the parameters used, consistently predict a shift outwards of the connection points between the LOV domains and the linker region.

Point (3), especially, is crucial for understanding how the information of light-activation having occurred in the LOV (sensor) domain is transmitted to the histidine kinase (effector) domain (Fig. 6.20). The shift is induced by the two LOV domain β-sheets tilting away from each other, thus pushing the two individual linker helices further apart (0.17 nm measured between the I126-Cα-atoms of chain A and B in both ENM-all and ENM-no87). In this manner, the LOV domains and the linker form a lever-like arrangement (shown in yellow in Fig. 6.20) capable of transmitting conformational changes from the sensor to the effector domain.

This represents the first structural model of the signal transduction mechanism between the LOV blue-light sensor domain and its effector domain partners. While it has been demonstrated here for the artificial protein YF1, this mechanism is likely to apply to other LOV domain proteins as well. Firstly, a similar arrangement of a LOV-LOV homodimer attached to an effector dimer via a coiled-coil linker has already been proposed as the structure of YtvA,[50] one of YF1's "parent proteins". Secondly, the extraordinarily wide range of different effector domains LOV domains are found coupled to in nature makes a common mechanism likely.

## 6.3 THE FLAVIN COFACTOR ENVIRONMENT STUDIED BY ENDOR

As has been discussed in Chapter 2.1, the recovery kinetics of the dark state of LOV domains vary by four orders of magnitude from protein to protein. To better understand the influence changes in the immediate chromophore environment have on LOV dark recovery kinetics, and to understand if such changes can be produced consistently, YF1 wt and three variants with point mutations in the vicinity

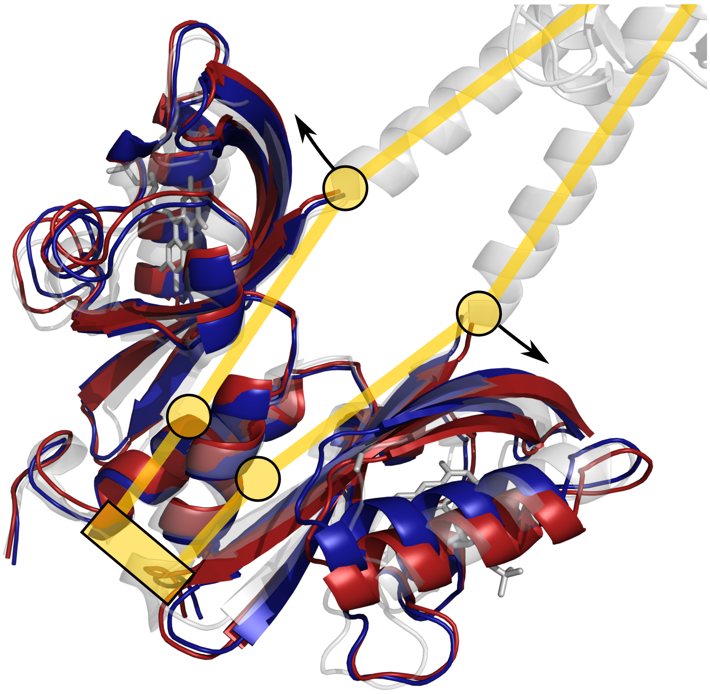

Figure 6.20. – **A schematic description of the transition from the YF1 dark (blue) to light (red) state.** The outward tilt of the LOV domains in a hinge-like motion (yellow) exerts a force onto the coiled-coil linker that can be transferred to the effector domain. The model shown is ENM-all.

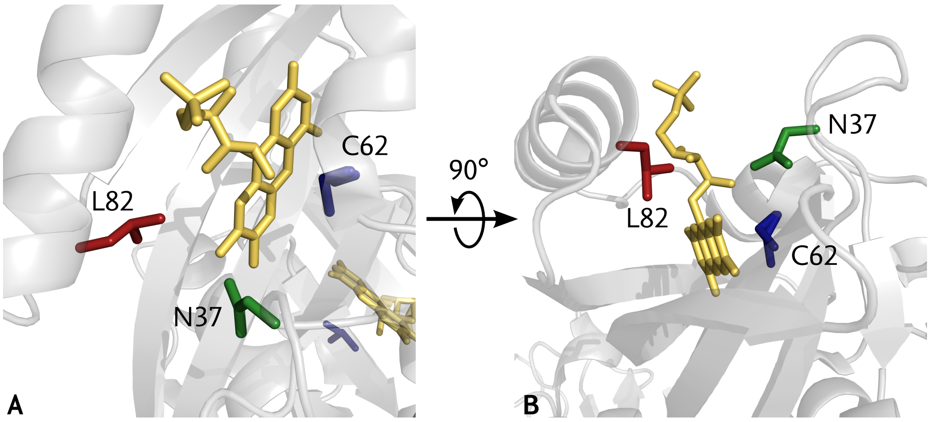

FIGURE 6.21. – **Residues in YF1 investigated by ENDOR.** YF1 and AsLOV2 share N37 (N425 in AsLOV2) (green), AsLOV2 has an isoleucine (I470) in place of YF1's leucine at position 82 (red). The replacement C62A (C450A in AsLOV2) (blue) causes LOV domains to accumulate a flavin radical under blue-light illumination, enabling study by EPR.[22,34] The structure shown is pdb 4GCZ.[9]

of the flavin's C8α methyl group, L82I, N37C and N37C/L82I (Table 6.5, column 2 and Figure 6.21), were targeted for study using UV/vis and ENDOR. To test whether these residues have similar effects across different LOV domains, the corresponding mutations were investigated also in the phototropin-1 LOV2 domain from *Avena sativa* (AsLOV2) (Table 6.5, column 3), which is widely used as a "standard" LOV domain in research.

**UV/vis measurements of dark recovery rates** Dark recovery rates $k_{-1}$ of all variants were determined using UV/vis spectroscopy[B]. In YF1, the rates varied from $(1.62 \pm 0.05) \times 10^{-4}\,\mathrm{s}^{-1}$ for YF1 wt to $(1.29 \pm 0.10) \times 10^{-3}\,\mathrm{s}^{-1}$ for YF1 N37C/L82I (Table 6.6), about one order of magnitude. The dark recovery rates in the corresponding AsLOV2 variants, while faster by about two orders of magnitude in general compared to YF1, show that the different mutations have a very similar relative effect (Table 6.6).

**ENDOR measurements** In order to analyse the molecular basis for these effects on dark recovery kinetics in more detail, the immediate environment of the flavin cofactor was probed using ENDOR spectroscopy. To this end, all previously mentioned variants had the active-site cysteine residue C62 (C450 in AsLOV2) replaced by alanine (Table 6.5), preventing formation of the Cysteinyl-C4a-adduct and al-

---

[B] These experiments were performed by N. Lemke and R. Diensthuber in the group of A. Möglich. Details are described in DIENSTHUBER *et al.*[149]

Table 6.5. – **YF1 and AsLOV2 variants investigated.** Each residue configuration was prepared in YF1 and AsLOV2, both for UV/vis and for ENDOR spectroscopy.

| Method | YF1 variant | AsLOV2 equivalent | Notes |
|---|---|---|---|
| UV/vis | wt | I470L | YF1 wt-like |
| | L82I | wt | AsLOV2 wt-like |
| | N37C | N425C/I470L | |
| | N37C/L82I | N425C | *C. reinhardtii* LOV wt-like |
| ENDOR | C62A | C450A/I470L | YF1 wt-like |
| | C62A/L82I | C450A | AsLOV2 wt-like |
| | N37C/C62A | N425C/C450A/I470L | |
| | N37C/C62A/L82I | N425C/C450A | *C. reinhardtii* LOV wt-like |

Table 6.6. – **Dark recovery rates of YF1 and AsLOV2 variants at 22 ℃.** While recovery rates in YF1 are slower than in AsLOV2 by about two orders of magnitude, the relative changes between variants are very similar in both proteins. Values taken from Diensthuber *et al.*.[149]

| Protein | Variant | $k_{-1}$ ($s^{-1}$) |
|---|---|---|
| YF1 | wt | $(1.62 \pm 0.05) \times 10^{-4}$ |
| | L82I | $(3.06 \pm 0.13) \times 10^{-4}$ |
| | N37C | $(6.94 \pm 0.07) \times 10^{-4}$ |
| | N37C/L82I | $(1.29 \pm 0.10) \times 10^{-3}$ |
| AsLOV2 | I470L | $(1.34 \pm 0.03) \times 10^{-2}$ |
| | wt | $(2.62 \pm 0.08) \times 10^{-2}$ |
| | N425C/I470L | $(5.71 \pm 0.04) \times 10^{-2}$ |
| | N425C | $(9.00 \pm 0.03) \times 10^{-2}$ |

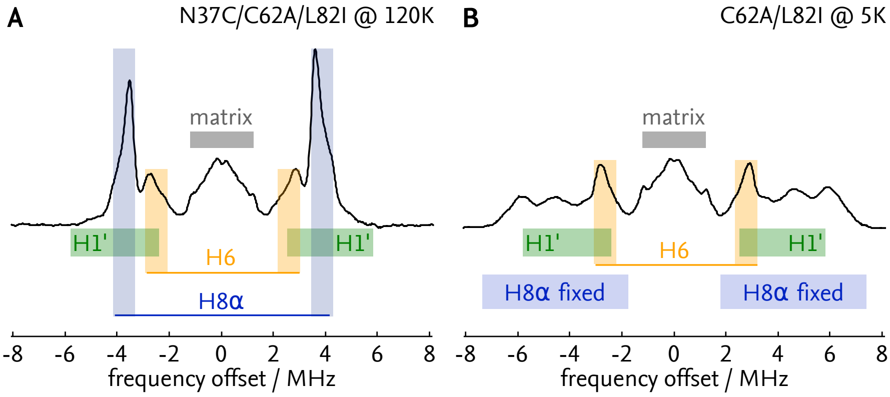

FIGURE 6.22. – **Example ENDOR spectra of a neutral flavin radical.** (A) Typical case. Clearly visible couplings are those of H8α at ± 4 MHz (blue) and H6 at ± 3 MHz (yellow) (See Fig. 2.1 for their location on the flavin). A H1' coupling (green) is visible at the outer edge of the H8α peaks, but mostly hidden beneath it. The central part of the spectrum stems mainly from unresolved couplings from matrix protons (gray). (B) Immobile case. The H8α line from (A) has given way to three individual couplings (See Section 4.1.2).

lowing for the photoaccumulation of a flavin radical.

Figure 6.22A shows a typical flavin spectrum. Besides the central matrix region, containing mainly unresolved small proton couplings (gray), three major components can be identified, namely the couplings of H6 (yellow), the three H8α (blue) and two H1' (green), of which only the outermost edge is distinctly visible. The peaks arising from H8α couplings are most pronounced because all three methyl protons have the same coupling. By contrast, Fig. 6.22B shows the unusual case of a flavin with an immobilised C8α group, causing the H8α line to split into three distinct couplings, one for each proton (See Section 4.1.2).

ENDOR measurements on YF1 and AsLOV2 variants were performed as described (p. 44). The results are shown in Figure 6.23. YF1 C62A at a temperature of 120 K shows the typical spectrum of a neutral flavin radical,[167] (Fig. 6.23A), with sharp peaks of the H6 at ± 3 MHz and freely rotating and thus averaged (see Eq. (4.14)) H8α protons appearing at ± 3.6 MHz[C]. Underlying both peaks are signals arising from the two H1' protons, the large coupling of the H5 proton of about 30 MHz falls outside the recording range. The intensity difference within pairs of lines is due to Boltzmann population differences and ENDOR enhancement[119] (for details see Section 5.1.1, p. 44).

Even though the mobile H8α peak still dominates the spectrum, a fraction of

---

[C] The frequency is given relative to the free proton frequency, thus the numbers on the x-axis correspond to ½ the hyperfine coupling frequency

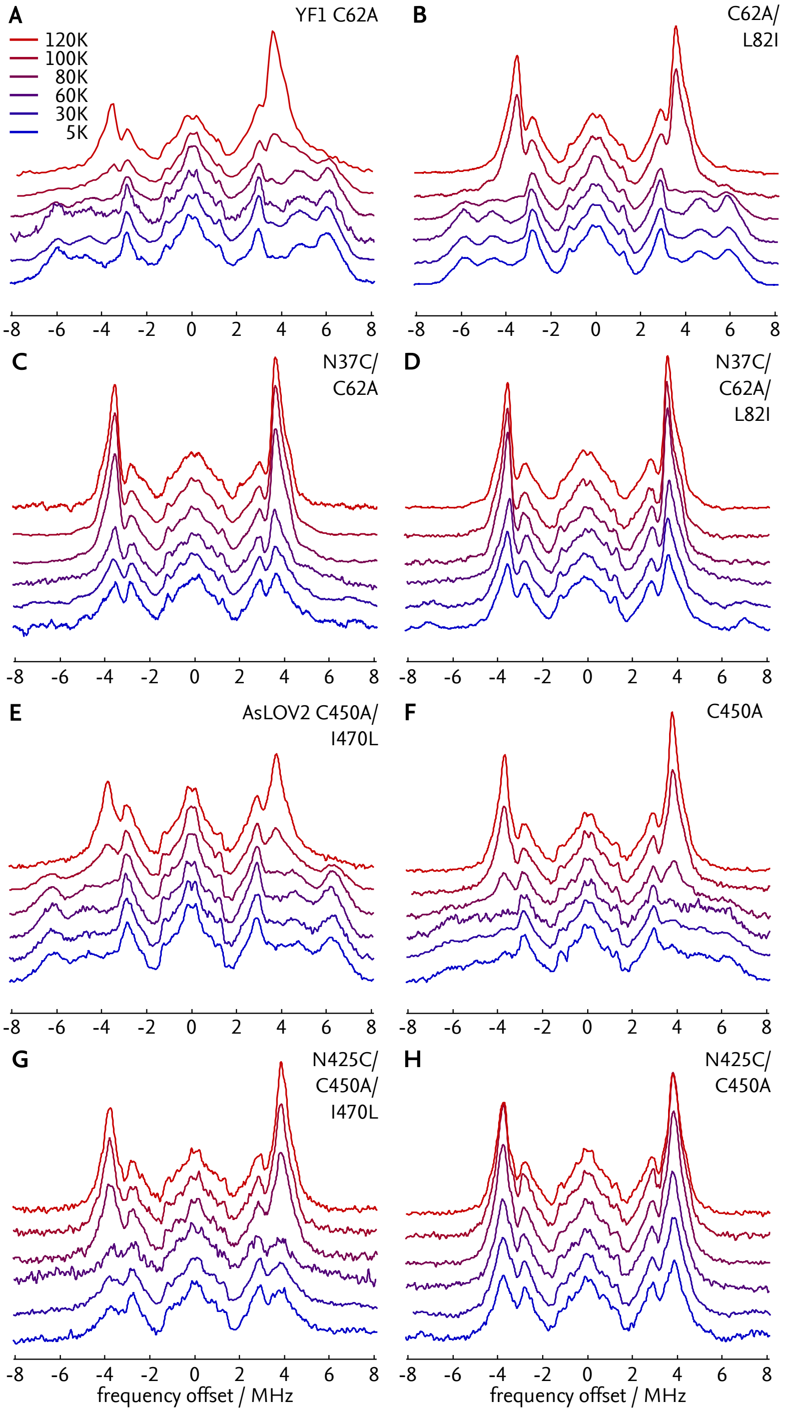

Figure 6.23. – **ENDOR spectra of YF1 (A-D) and AsLOV2 (E-H) variants**. The frequencies are given relative to the free proton frequency. Each variant was measured over a temperature range from 5 K to 120 K (blue to red). The typical features of a neutral flavin radical as described in Fig. 6.22A are clearly visible at higher temperatures for all variants. At low temperatures, signals from immobilised H8α appear between ± 1–7.5 MHz.

immobilised methyl group protons is already discernible in the ±1–7.5 MHz range. With lower temperatures, the mobile fraction is progressively lost, and already at 60 K, atypically high for a methyl group, the entire methyl group population has become immobilised.

The YF1 variants C62A/L82I (Fig. 6.23B), N37C/C62A (Fig. 6.23C) and N37C/-C62A/L82I (Fig. 6.23D) show essentially the same spectra, although with the transition from mobile to spatially restricted C8α group occurring at successively lower temperatures, with N37C/C62A/L82I especially retaining a relatively large fraction of mobile C8α even at a temperature of 5 K. Additionally, while the structure of the spatially restricted methyl group's signals is the same between C62A and C62A/L82I (Fig. 6.23A and B, 5–6 MHz range), both N37C/C62A and N37C/C62A/-L82I show a markedly different structure (Fig. 6.23C and D, peak at 7 MHz). This is indicative of the methyl group being fixed at a different angle relative to the π system in these variants (see Section 4.1.2, p. 23).

The corresponding AsLOV2 variants, strikingly, show the same behaviour (Fig. 6.23E–H), both in terms of the transition from mobile to immobile C8α group, which happens at the highest temperature in AsLOV2 C450A/I470L (Fig. 6.23E) and the lowest in AsLOV2 N425C/C450A (Fig. 6.23H), as well as in terms of the change in the immobile methyl group's orientation, with similar patterns observed for AsLOV2 C450A/I470L and C450A as for YF1 C62A and C62A/L82I ((Fig. 6.23E and F versus A and B) and for AsLOV2 N425C/C450A/I470L and N425C/C450A as for YF1 N37C/C62A and N37C/C62A/L82I (Fig. 6.23G and H versus C and D).

**Simulating ENDOR spectra** In order to quantitatively characterise these observations, simulation of all spectra were performed. To minimise the number of free parameters, these simulations were, as far as possible, performed collectively, i.e. with one parameter set describing all spectra. To this end, the following initial assumptions were made based on visual inspection of the spectra:

1. Both H6 and H1' couplings are identical for all samples.
2. The anisotropic part of the immobile H8α hyperfine matrix is identical for all samples.
3. The isotropic part can be described using the Heller-McConnell model[112] according to Eq. (4.13) and (4.14). The 120° symmetry between the three protons allows one set of parameters $a_1$, $a_2$ and $\theta$ to be used for all three.
4. Changing the temperature has no influence on the hyperfine couplings, only on relative line intensities,

resulting in a minimal parameter set.

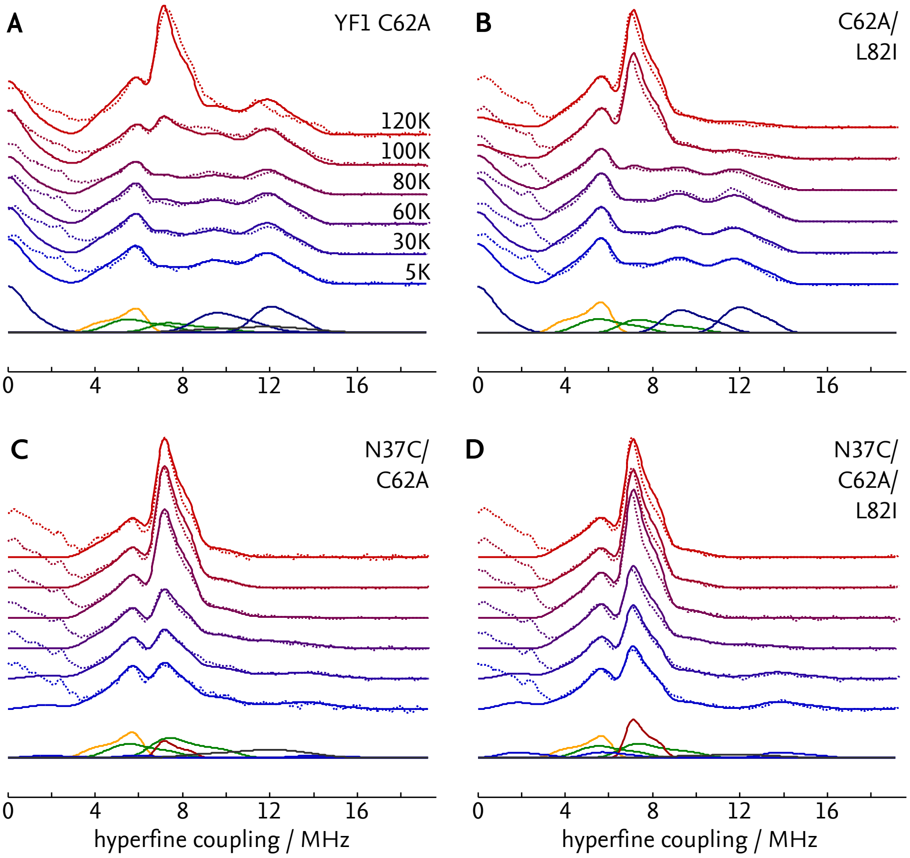

Figure 6.24. – **Simulation of ENDOR spectra of YF1 (solid) compared to measured spectra (dotted) from 5–120 K (blue–red).** Underneath each set of measurements, the individual 8 components making up each spectrum are shown exemplarily for 5 K: H6 (yellow), H1' (2x green), immobile H8α (3x blue), mobile H8α (red) and an additional intermediate, semi-mobile component (gray). With the exception of the unresolved matrix protons between 0–3 MHz, all simulations excellently reproduce the data. The parameters used are given in Table 6.7 and Appendix A, Table A.2.

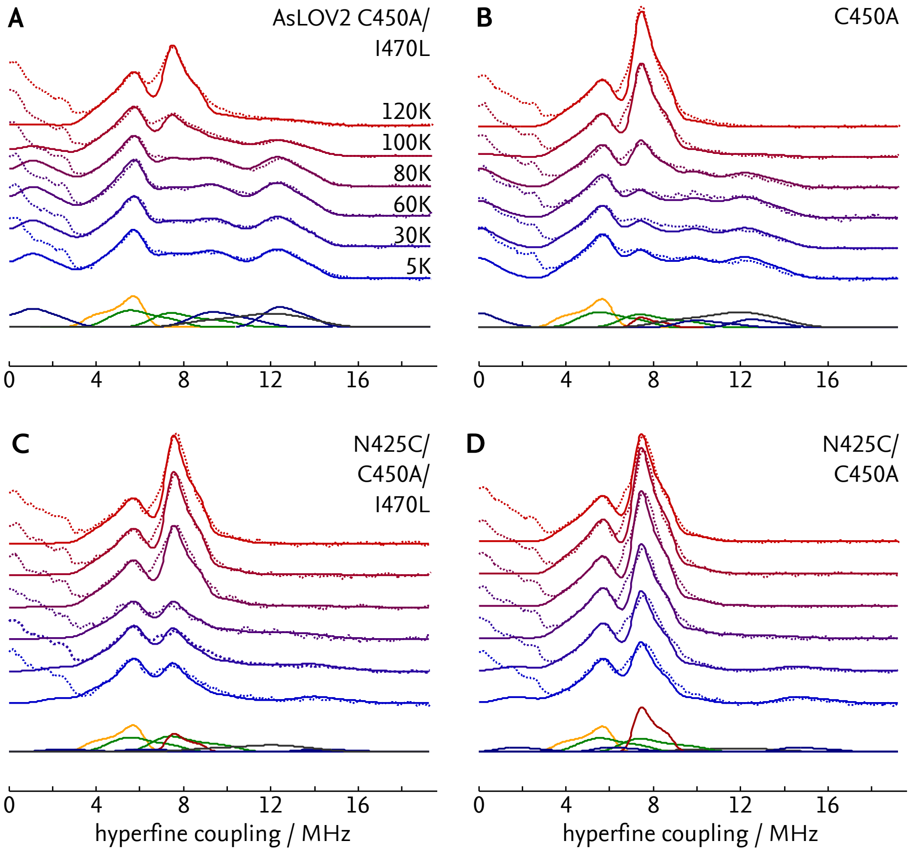

Figure 6.25. – **Simulation of ENDOR spectra of AsLOV2.** The parameters used are given in Table 6.7 and Appendix A, Table A.3. For details, see 6.24.

Since the H1' matrices cannot be reliably identified due to spectral overlap with H6 and H8α, values derived from AsLOV2 C450A incorporating selectively deuterated FMN (unpublished data from R. Brosi, used with permission) where adopted as-is. After an initial manual simulation/optimisation, assumption (1) and (2) were relaxed as needed, though only very small changes were required for an optimal fit. Lastly, parameters critical to this study were programmatically optimised as described in Section 5.1.1 (p. 46). The resulting simulations are shown in Figures 6.24 (YF1) and 6.25 (AsLOV2).

Overall, a very good agreement between simulation and measurement could be achieved with the parameters set up as explained above, with only very slight adaptations of H6 isotropic and H8α anisotropic couplings needed for some of the samples (the full set of hyperfine and other simulation parameters is given in Appendix A).

Table 6.7. – **C8α methyl group isotropic hyperfine couplings and angles.** θ is given relative to the orientation of the π system as indicated in Figure 4.2B. Errors for hyperfine parameters $a_1$ and $a_2$ are estimated.

| Variant | $a_1$ (MHz) | $a_2$ (MHz) | θ (°) |
|---|---|---|---|
| YF1 C62A | $0.64 \pm 0.05$ | $14.00 \pm 0.05$ | $36.7 \pm 0.4$ |
| YF1 C62A/L82I | $0.23 \pm 0.05$ | $14.44 \pm 0.05$ | $35.5 \pm 0.2$ |
| YF1 N37C/C62A | $0.09 \pm 0.05$ | $14.90 \pm 0.05$ | $-6 \pm 5$ |
| YF1 N27C/C62A/L82I | $0.09 \pm 0.05$ | $14.84 \pm 0.05$ | $-7 \pm 3$ |
| AsLOV2 C450A/I470L | $0.54 \pm 0.05$ | $14.40 \pm 0.05$ | $37.8 \pm 0.8$ |
| AsLOV2 C450A | $1.09 \pm 0.05$ | $13.12 \pm 0.05$ | $35 \pm 5$ |
| AsLOV2 N425C/C450A/I470L | $0.40 \pm 0.05$ | $15.09 \pm 0.05$ | $-11 \pm 6$ |
| AsLOV2 N425C/C450A | $0.05 \pm 0.05$ | $15.62 \pm 0.05$ | $-11 \pm 6$ |

Table 6.7 gives the resulting hyperfine coefficients $a_1$ and $a_2$ as well as the angle of one methyl group proton relative to the flavin π system in the sterically hindered configuration. In the wt analogue YF1 C62A, the angle of 36.7(4)° shows the group to have one proton close to aligned with the flavin isoalloxacine plane[D]. Exchanging leucine 82 with isoleucine brings the proton closer to alignment by about 1°, to an angle of 35.5(2)°. Replacing asparagine 37 in both these variants with cysteine causes a large reorientation of the sterically hindered group, close to an alignment parallel to the π system (-6(5)° for N37C/C62A, -7(3)° N37C/C62A/L82I). The effects of both exchanges, asparagine to cysteine and leucine to isoleucine, appear to be cumulative, although in the cysteine-containing variants, the change induced by isoleucine is actually within the margin of error. The orientation of the immobilised C8α methyl group appears to be conserved across different LOV domains, since the corresponding AsLOV2 variants give the same results, taking into account errors. A previous study by Brosi *et al.*,[34] using *ab initio* quantum-mechanical (QM) calculations, found a similar angle for AsLOV2 C450A.

While the fully averaged and fully immobile components of the C8α group are perfectly described by Eq. (4.13) and (4.14), the transition from one to the other does not happen instantaneously but proceeds via a broad distribution of intermediate "slow" states. These "slow" states are especially apparent in the asparagine-to-cysteine mutants at intermediate temperatures, e.g. in the broad shoulder next to the mobile C8α peak in YF1 N37C/C62A at 60 K, Figure 6.24C), because they are well separated from the signals of fully immobilised protons. Accordingly, difference spectra of these mutants, particularly YF1 N37C/C62A at 60 K minus 80 K,

---

[D] Due to the 120° symmetry of the methyl group and the 180° symmetry of the π system, an angle of 0°, 60°, 120° … indicates alignment of one proton perpendicular to the molecular plane, while 30°, 90°, 150°, … indicates alignment with the molecular plane.

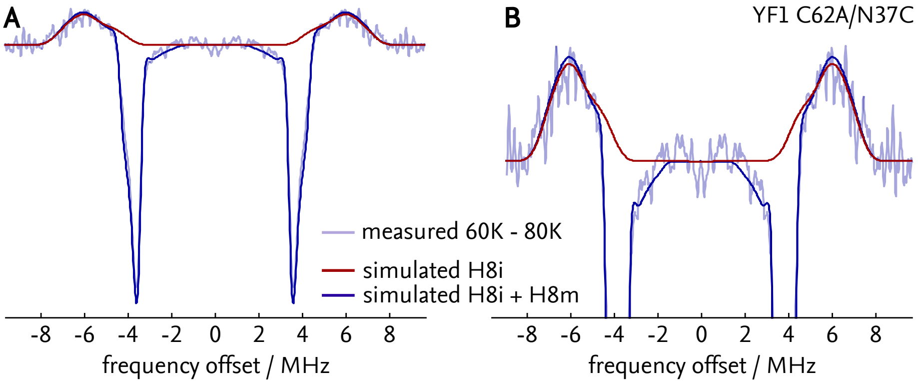

FIGURE 6.26. – **Intermediate “slow” states of H8α coupling in YF1 N37C/C62A at 60 K and 80 K.** (A) Difference spectrum of YF1 N37C/C62A at 60 K minus 80 K (blue, dotted) show the appearance of “slow” C8α proton states, H8i (red) in parallel to a decrease in the amount of mobile C8α protons H8m (blue). (B) 3x magnified view of (A).

were used to produce a fit of these states (Figure 6.26).

### 6.3.1 RELATING THE FMN CHROMOPHORE ENVIRONMENT TO DARK RECOVERY KINETICS

Unfortunately, due to spectral overlap of the “slow” component H8i and the immobile component, the fractional population of these intermediate states could not be determined with any great accuracy for YF1 C62A and C62A/L82I as well as AsLOV2 C450A and C450A/I470L in particular. Therefore, the fractional population of the fully mobile C8α as a function of temperature derived from the simulations was used to characterise the transition kinetics by non-linear least-squares fitting of a logistic function for a two-state transition model (Figure 6.27A and B).

All asparagine-to-cysteine variants, as well as to some degree AsLOV2 C450A, show a significant fraction of mobile methyl group even at 5 K. This is not unexpected, since the complex energy landscape and conformational space of the chromophore environment produces populations with varying transition activation energies, and quantum-mechanical tunnelling allows for proton interchangeability down to 0 K.

Accordingly, the two-state transition model was fit without imposing boundary conditions for T = 0 K. For YF1 C62A, a midpoint transition temperature of $(124 \pm 2)$ K was determined, while YF1 C62A/L82I, YF1 N37C/C62A and YF1 N37C/C62A/L82I showed successively lower midpoint temperatures of $(93.3 \pm 0.1)$ K, $(68 \pm 2)$ K and $(53 \pm 5)$ K, respectively. As was to be expected from the raw data, the AsLOV2 variants show much the same behaviour, with transition temperatures

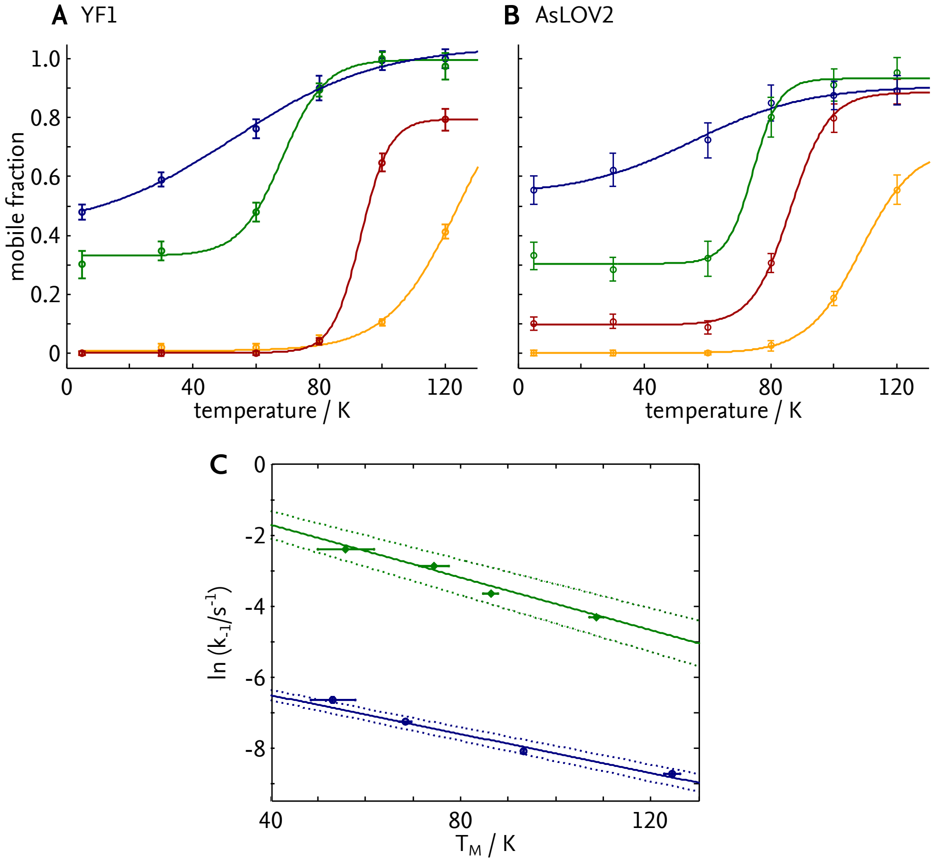

FIGURE 6.27. – **Fractional population of mobile C8α as a function of temperature in YF1 variants (A) and AsLOV2 variants (B).** The fitted two-state transition model allows for the extraction of transition temperatures (Table 6.8). Plotting the natural logarithm of the dark state recovery rate $k_{-1}$ as a function of $T_M{}^{C8\alpha}$ reveals a linear dependence (C) for both LOV domains.

TABLE 6.8. – Transition temperatures for mobile-to-restricted C8α.

| Variant | $T_M{}^{C8\alpha}$ (K) |
|---|---|
| YF1 C62A | 124 ± 2 |
| YF1 C62A/L82I | 93.3 ± 0.1 |
| YF1 N37C/C62A | 68 ± 2 |
| YF1 N27C/C62A/L82I | 53 ± 5 |
| AsLOV2 C450A/I470L | 109 ± 2 |
| AsLOV2 C450A | 86 ± 2 |
| AsLOV2 N425C/C450A/I470L | 74 ± 3 |
| AsLOV2 N425C/C450A | 56 ± 6 |

TABLE 6.9. – Correlation coefficient and proportionality factor of $\ln(k_{-1}/s^{-1})$ and $T_M^{C8\alpha}$ derived from Fig. 6.27C.

| Protein | Correlation coeff. | slope (1/K) |
|---|---|---|
| YF1 | −0.989 | $-0.027 \pm 0.001$ |
| AsLOV2 | −0.986 | $-0.038 \pm 0.003$ |

of (86 ± 2) K for AsLOV2 C450A, (109 ± 2) K for AsLOV2 C450A/I470L, (56 ± 6) K for AsLOV2 N425C/C450A and (74 ± 3) K for AsLOV2 N425C/C450A/I470L (Table 6.8).

Somewhat surprisingly, plotting the natural logarithm of the dark state recovery rates at 22 °C $k_{-1}$ (see Table 6.6) versus the midpoint transition temperature of each variants reveals a linear dependence with linear correlation coefficients of -0.989 and -0.986 and slopes of $(-0.027 \pm 0.001)\,\mathrm{K}^{-1}$ and $(-0.038 \pm 0.003)\,\mathrm{K}^{-1}$ for YF1 and AsLOV2, respectively. In keeping with what has been previously noted, the different residue combinations have the same effect in both LOV domains (Table 6.9). This is especially notable bearing in mind the inherent conformational flexibility of proteins as well as the fact that two entirely different LOV domains, bacterial LOV in the case of YF1 and plant LOV2 in the case of AsLOV2 were chosen for this study.

Obviously, the correlation of two quantities can not be considered proof of a causal relationship. In this case in particular, the fact that the effects on dark recovery rates are observed at physiological temperatures, while the effects on methyl group mobility and orientation are observed at 120 K and lower makes a direct causation of the former by the latter very unlikely. The likeliest explanation is that both processes are similarly affected by the changes in the flavin chromophore environment induced by mutation.

Looking at the flavin binding pocket in high-resolution crystal structures,[9,168] one finds that in both proteins the C8α methyl group is embedded into multiple hydrophobic side chains, comprising T30, N37, L82, I108 and F119 in YF1 (T418, N425, I470, L496 and F509 in AsLOV2). However, while the side chain of isoleucine I470 in AsLOV2 is branched at the Cβ atom, orienting its Cγ1 away from the C8α group of the chromophore, the corresponding leucine L82 in YF1 is branched at the Cγ atom, causing the Cδ1 and Cδ2 methyl groups to bracket the C8α of the chromophore. As shown above, replacing leucine 82 with isoleucine in YF1 grants greater conformational freedom to the methyl group, as does replacing asparagine 37 with cysteine. For AsLOV2, similar effects have been previously observed for other residues in the aforementioned group.[34] All these observations clearly point to the rotational freedom typically observed in methyl groups being hindered by the packing of the hydrophobic side chains surrounding the chromophore in the

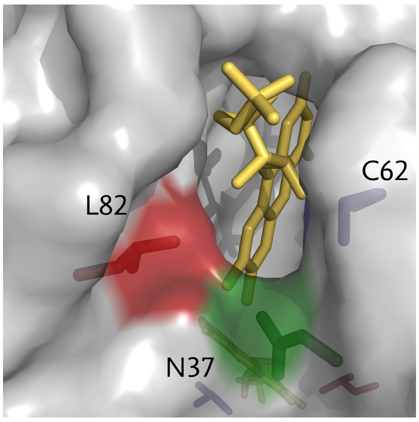

FIGURE 6.28. – **FMN situated inside the YF1 binding pocket**. L82 (red) and N37 (green) are surface-exposed and can likely influence the water accessibility of the flavin (yellow).

investigated LOV domains.

Alterations in the hydrophobic residues in the vicinity of the flavin ring can also account for the changes in dark recovery rates observed. In LOV domains, the flavin is situated relatively close to the protein surface inside a surface-exposed, water-filled binding pocket (Fig. 6.28). It is therefore likely that alterations of residues in this region not only affect the conformational freedom of the chromophore, but also solvent access. The return from the signalling to the dark state involves the initial abstraction of the proton bound at flavin position N5 and is base-catalysed.[169] Here, the water filling the binding pocket could act as a general base catalyst. Different configurations of hydrophobic side chains could influence how closely water can approach the chromophore, thereby modulating dark recovery kinetics, explaining the observed effects. Altered water access has already recently been suggested as a possible explanation for varying photocycle kinetics in AsLOV2 variants.[170]

### 6.3.2 STUDYING YF1 IN AN *IN VIVO* CONTEXT

The effect of water accessibility on photocycle kinetics gives rise to the question in how far the *in vivo* solvent, i.e. the cell environment can influence the photoreceptor's function. To this end, the YF1 variant YF1 C62A was injected into *X. laevis* oocytes, which where then transferred into EPR capillaries, illuminated and frozen (see Section 5.2.1, p. 61) and studied using ENDOR in a single cell experiment under conditions otherwise identical to the previous *in vitro* experiments.

Measurements were taken at 30 K and 80 K (Figure 6.29). Due to the limited SNR of single-cell experiments, no spectra at higher temperatures could be recorded,

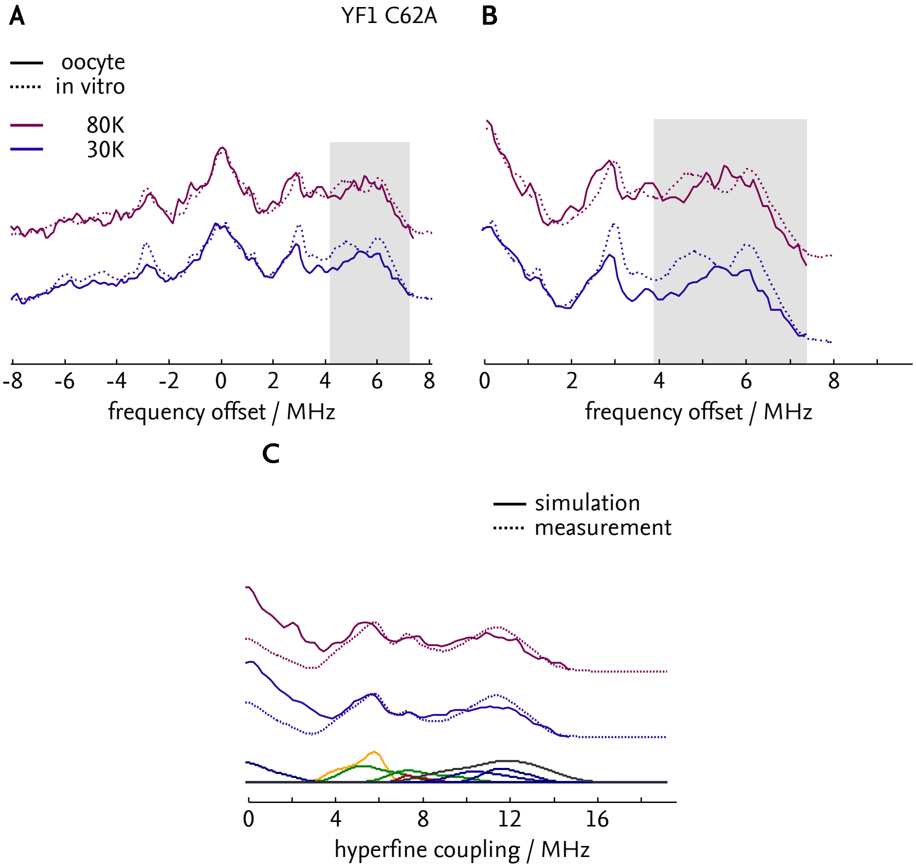

FIGURE 6.29. – **ENDOR measurements of YF1 C62A in a single *X. laevis* oocyte.** (A) *In vivo* measurements (solid lines) reveal a distinctly different pattern of sterically hindered H8α couplings than *in vitro* (dotted lines) between ±4.0–7.2 MHz (shaded). (B) Enlarged view of (A). (C) Simulation of YF1 C62A *in vivo* spectra (solid) compared to measurements (dotted) at 30 K and 80 K.

TABLE 6.10. – Methyl group angle and mobility of YF1 C62A at 80 K in a single oocyte and *in vitro*. Full simulation parameters are found in Appendix A, Table A.1.

| Context | θ (°) | fraction of mobile C8α |
|---|---|---|
| *in vitro* | 36.7 ± 0.4 | 0.045 ± 0.016 |
| *in vivo* | 34.3 ± 0.6 | 0.09 ± 0.03 |

meaning that at least for this variant, the mobile-to-sterically hindered transition could not be mapped.

Strikingly, comparing the single-cell spectra to corresponding spectra *in vitro* (Fig. 6.29A) reveals that the pattern of sterically hindered C8α couplings differs between *in vivo* and *in vitro* spectra, again indicative of a changed orientation of the immobile methyl group. Indeed, simulating the spectra (Figure 6.29B) yields a nominal angle θ of (34.3 ± 0.6)°, shifted from (36.7 ± 0.4)° (Table 6.10). The mobile-to-immobile transition temperature also appears to be slightly changed, since the fraction of mobile C8α at 80 K is slightly higher in the single cell spectrum than *in vitro* (Table 6.10).

Usually in in-cell EPR experiments, a spectrum averaged over all cell environments is observed. This is not the case for a single cell experiment, where all observed proteins share the same environment. If the cell environment itself induces larger conformational freedom instead of a defined conformational change, in the protein, again an averaged spectrum is observed. It should be noted, that due to the limited SNR of the *in vivo* measurement, this possibility cannot be fully excluded. Thus, there are two possible explanations for the changes in the C8α methyl group's ENDOR spectrum, one, the change from buffer solution to cell environment causes a slight reorientation of the hydrophobic amino acids that results in a change of the "clamping" of the methyl group, two, the cell environment confers additional conformational flexibility to the entire protein, and thereby produces multiple methyl group orientations that then overlay in the spectrum. In either case, ENDOR measurements of the flavin cofactor are a sensitive probe for the conformational energy landscape of the protein *in cellulo*.

### 6.3.3 A UNIFIED APPROACH TO LOV DOMAIN PHOTOCYCLE DYNAMICS

The ENDOR simulations demonstrate that the flavin chromophore's proton hyperfine parameters are very much conserved across different LOV domain variants, with differences mainly being caused by reorientations of ENDOR-accessible β-protons, mainly H8α and H1',[171] which can be described using a simple Heller-McConnell model,[112] rendering simulation of the spectra both reliable and straightforward, potentially allowing the prediction of photocycle kinetics in contexts where direct measurements are not feasible, e.g. *in vivo*.

Being able to tune the photocycle kinetics of LOV proteins by variations of residues in the vicinity of the flavin chromophore has large implications for applications in cell biology, biotechnology and synthetic biology. That variations in residues change the chromophore environment in a predictable manner conserved across LOV domains, as evidenced by the ENDOR and dark state recovery kinetics data, demonstrates that such tuning is possible in a predictable manner. However, bearing in mind the clear correlation between dark state recovery kinetics and C8α methyl group conformational freedom, the finding that the flavin environment, by proxy of the C8α methyl group is different *in vivo* and *in vitro* emphasises the importance of studying these effects, as far as possible, in an *in vivo* context.

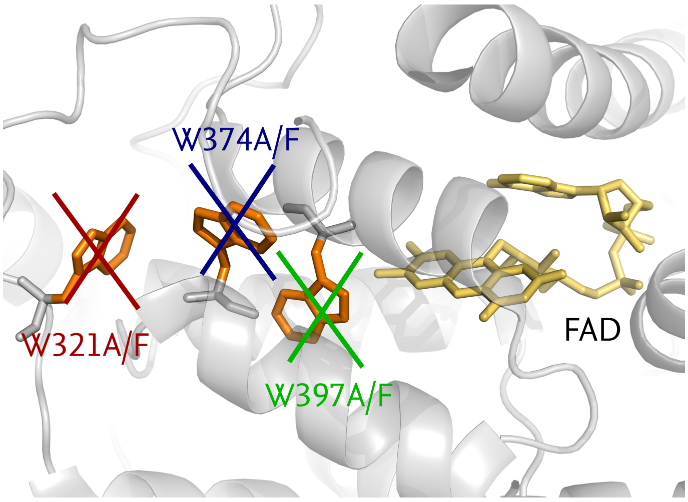

FIGURE 6.30. – **trp triad mutants of cryptochrome-2 targeted in this study**. Six variants, each with one of the three tryptophanes in the trp triad, W321 (marked red), W374 (blue) and W397 (green) selectively replaced by alanine or phenylalanine. (pdb: 1U3D[60]).

## 6.4 THE EFFECT OF CELLULAR METABOLITES ON THE LIGHT SENSITIVITY OF *A. THALIANA* CRY2

As described in Chapter 2.3, photoreduction of the FMN cofactor via the conserved trp triad has long been considered the essential first step in the signalling process of cryptochromes, an interpretation that is well supported by several lines of evidence. However, cry2 variants with interrupted trp triads, cry2 W321A, W374A and W397A, were found to show biological activity *in vivo* while not undergoing significant photoreduction *in vitro*.[16]

To address this seeming contradiction, the same variants, as well the their WxxxF analogues (Fig. 6.30) were investigated both *in vivo* and *in vitro* using cw EPR and trEPR.

### 6.4.1 IN-CELL CW EPR OF CRY2 VARIANTS

To characterise potential redox forms of flavin generated *in vivo*, Sf21 cells expressing the trp triad mutants cry2 W321A, W321F, W374A, W374F, W397A and W397F as well as wt were illuminated with blue light, frozen and measured using cw EPR (see Materials section, 5.2). The expected signal intensity from whole cell samples is small due to the low effective sample concentration. Since some background signal is unavoidable, a sample of uninfected control cells, treated exactly as the

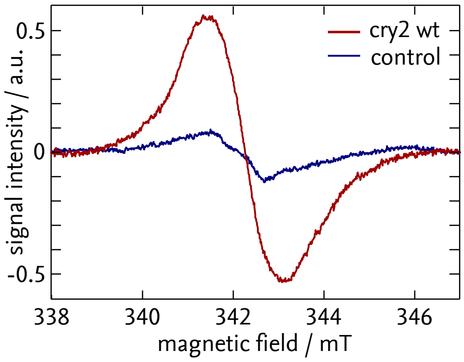

Figure 6.31. – **continuous-wave EPR spectra of cells expressing cry2 wt (red) and control cells (blue), both after illumination** The EPR spectrum of cry2 is typical for a flavin radical..

cry2-expressing variants, was measured and its spectrum subtracted from each as background correction. Since the reference background was taken from an illuminated control, this eliminates both the spectrometer background and potential light-induced or stable radicals present in the cells, but unrelated to cry2.

Fig. 6.31 shows the uncorrected spectrum obtained from cry2 wt together with the control. As expected, illuminated cry2 wt shows an unresolved line common for many organic radicals, including flavins, with a peak-to-peak width and shape consistent with a flavin radical. This is indicative of the photoreduction of the flavin from the oxidised to the radical form in the cry2 photoreceptor.

Spectra after background correction of the six trp triad mutants are shown in Fig. 6.32A-F. Strikingly, with the exception of W397F (Figure 6.32F), all trp triad mutants show a clear flavin radical signal above background as well (Figure 6.32A-E), indicating the formation of a flavin radical even in the absence of a functional trp triad. As can be seen from the SNR, WxxxF mutations (Fig. 6.32E-G) show less signal than WxxxA variants (Fig. 6.32B and D), hinting that the phenylalanine substitutions might destabilise the protein. However, the data as recorded here does not lend itself easily to quantitative analysis, since external factors like cell density and in-cell protein concentrations have a large influence on the signal intensity and cannot be completely controlled for (A discussion of the difficulties involved in performing quantitative EPR on cell samples can be found in [171]).

Regardless, the spectra, particularly of the tryptophane-to-alanine mutants, demonstrate conclusively that cry2 variants lacking a functional trp triad retain, to a varying degree, their photochemical activity *in vivo*, in marked contrast to results *in vitro*.[16,172]

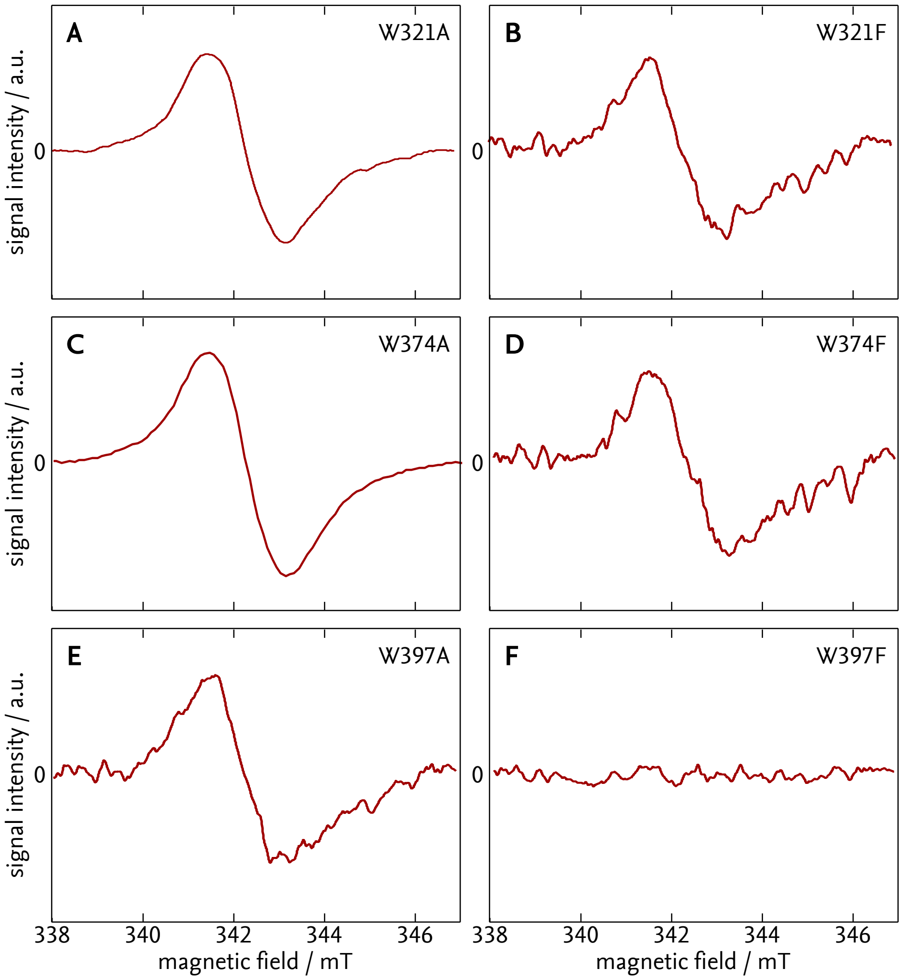

FIGURE 6.32. – **continuous-wave EPR spectra of cells expressing cry2 variants after illumination.** With the exception of W387F (G), all samples show significant signal above background. Spectra have been normalised.

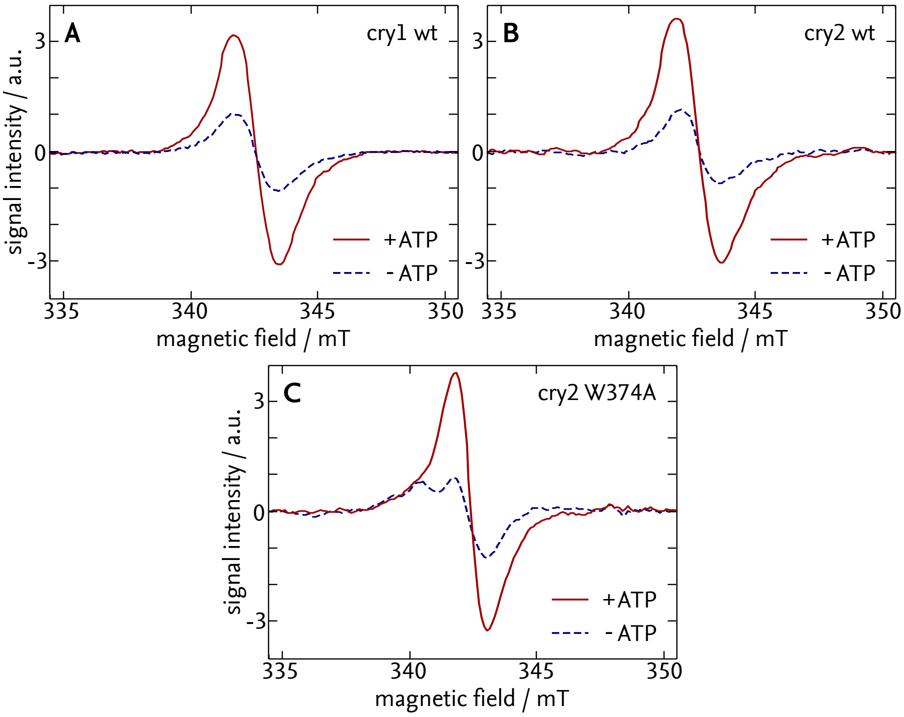

Figure 6.33. – **Continuous-wave EPR spectra of flavin radical accumulated in isolated cry2 trp triad mutants without (blue, dashed) and with 10 mM ATP added.** Spectra have been scaled relative to each sample's ATP-less intensity. Both cry1 (A) and cry2 (B) as well as cry2 W374A (C) show a similar increase in signal intensity in the presence of ATP.

## 6.4.2 TRANSIENT EPR AND CW EPR OF CRY2 VARIANTS *IN VITRO*

Experiments performed in the group of M. Ahmad, described in detail in Engelhard *et al.*[150] indicated that while both cry2 wt and trp triad mutants were photochemically active *in vivo*, only wild type proteins retained their photochemical activity after the removal of small molecular weight soluble factors (weight cutoff at 3500 kD), while trp triad mutant variants lost theirs. Since cryptochrome is known to have affinity for nucleotide-based cofactors such as ATP[60,173] the effect of these cofactors on photoreduction and radical formation in purified cryptochrome variants was further investigated.

**cw EPR experiments on purified proteins** As expected, cw spectra of both cry1 and cry2 wt proteins showed a pronounced signal from accumulated flavin radical (Fig 6.33A and B, blue). These signals increased markedly when 10 mM ATP was added to the sample prior to illumination (red).

The W374A spectrum showed some accumulated flavin radicals signal even in the absence of ATP (Fig. 6.33C, blue). Addition of ATP again significantly increased the amount of accumulated flavin radical (red) in a quantitatively similar fashion as observed for cry1 and cry2 wt. The same effect for ATP, as well as nicotinamide adenine dinucleotide (NADH), was observed in UV/vis spectroscopy.[150]

It is clear from both the EPR (this work) and UV/vis[150] data that the presence of ATP and similar metabolites potentiates the photochemical activity in cry2. Since this effect, present in crude and dialysed cell lysates, persists in isolated proteins, this can not be due to these metabolites modulating the activity of other proteins which in turn promote cryptochrome photoreduction, but has to be a direct effect on cryptochrome itself. Additionally, a role of ATP as direct electron donor can be excluded since addition of inosine triphosphate (ITP), the oxidised analogue of ATP, produced the same effect.[150] The most likely explanation therefore is that binding of ATP to cry2 results in small conformational changes of the protein that potentiate its photosensitivity.

There are two possible means by which this could be achieved. One, the conformational changes induced by ATP's and related metabolites' binding to cry2 could stabilise the radical form of the protein, formed after light-excitation, as has been reported previously for cry2 *in vitro*.[174] This would reduce the flavin reoxidation rate and promote radical accumulation, yielding the larger signals observed *in vivo* and in the presence of ATP *in vitro*. Two, the efficiency of the primary electron transfer from the solvent to the flavin itself could be increased in an *in vivo* context.

The electron transfer efficiency is experimentally accessible by way of observing the scRP formed immediately after photoexcitation using trEPR.

**Transient EPR experiments on purified proteins** The trEPR experiments were performed on liquid samples at 274 K. While this necessitates very low sample volumes and drastically reduces the achievable SNR, staying in a physiological temperature range ensures the relevance of the observed effects.

The wildtype spectra of cry2 in the absence of ATP (Fig. 6.34A and C, blue, dashed) shows an emissive-absorptive pair of lines split by approximately 1.5 mT. This signal arises from the scRP formed between the flavin and a distal trp or tyrosine (tyr) radical[66] and is a direct indicator of the forward electron transfer reaction. The same signal can be observed in cry1 wt (Figure 6.30B, blue, dashed). In the cry2 W321A mutant, with the trp triad interrupted at the distal tryptophane, a small scRP signal is still discernible (Figure 6.30E, blue, dashed), while in cry2 W374A, interrupted at the middle tryptophane, the signal has dropped below the detection threshold (Figure 6.30D, blue, dashed). The presence of a scRP signal even in the absence of ATP in cry2 W321A is an indication for the existence of

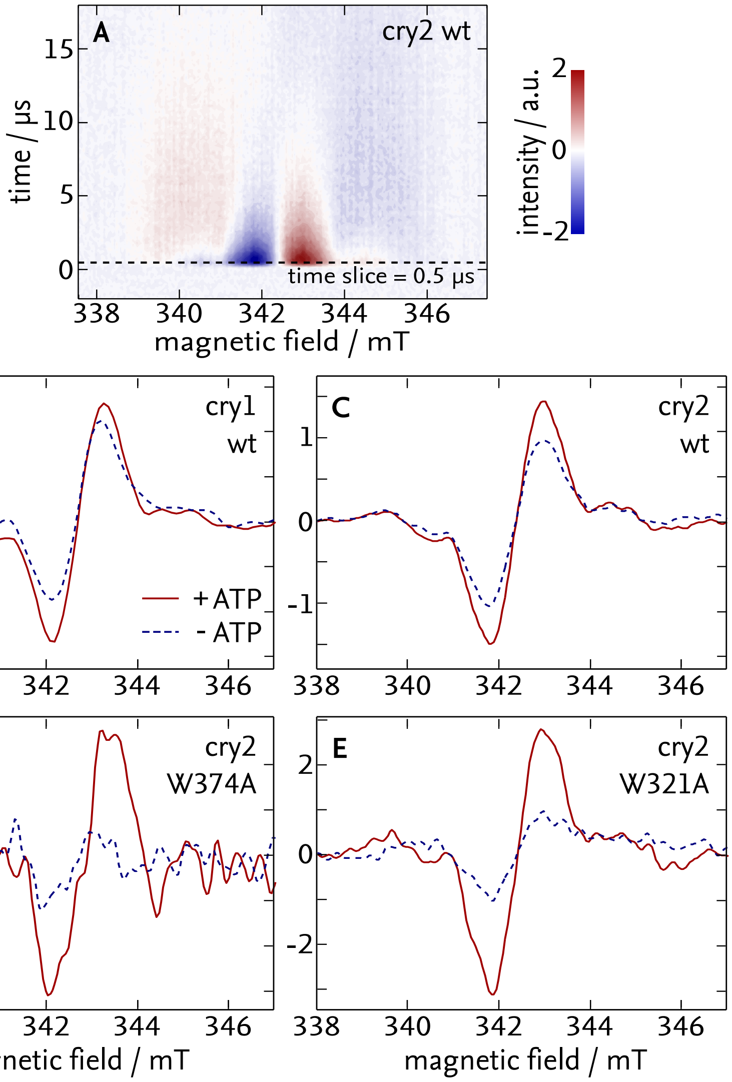

Figure 6.34. – **Transient EPR spectra of isolated wt proteins and cry2 trp triad mutants.** (A) raw 2-dimensional trEPR spectrum of cry2 wt in the absence of ATP, showing the typical scRP signal. Blue indicates emissive, red absorptive parts of the spectrum. (B-E) 1-dimensional time slices at t = 0.5 µs of trEPR spectra from cry1 wt (B), cry2 wt (C), cry2 W374A (D) and cry2 W321A (E) with (red, solid) and without (blue, dashed) addition of 10 mM ATP. All variants show an increase in scRP signal in the presence of ATP.

alternative electron pathways that bypass W321A, as reported previously.[66,175] While no such signal is apparent in the transient data from W374A, it is possible that such pathways still play a minor role under the saturating illumination conditions used for cw EPR experiments, which could explain the residual signal observed for W374A in those experiments.

Upon addition of ATP, the scRP signal of both cry2 W321A and W374A increase significantly (Figure 6.30D, E, red) compared to the spectra from samples lacking ATP. A similar but quantitatively smaller increase can be observed for the wildtype samples of cry1 (Fig. 6.30B, red) and cry2 (Fig. 6.30C, red). Since these increases in signal are not accompanied by changes in spectral shape and/or width, which would point to ATP altering the magnetic parameters of the sample, they instead directly demonstrate that the addition of ATP increases the quantum yield of the forward electron transfer.[175] Since both mutant proteins lack a functional trp triad, this, by definition, demonstrates that ATP facilitates electron pathways along alternate pathways, bypassing the trp triad. The decreased effect observed in wildtype proteins is most likely due to the electron transfer along the trp triad being already efficient at the light intensity and temperature used. Nonetheless, the effect of ATP is clearly visible even in wildtype proteins, demonstrating the relevance of alternate pathways even when the trp triad is uninterrupted. The dependence of scRP quantum yield on the presence of ATP in cry2 is in agreement with results obtained on isolated cry1 wt.[176]

As mentioned, the existence of alternate electron pathways has been demonstrated previously for cryDASH.[66] The new finding here is that the binding of ATP and similar metabolites to cry2 opens up new pathways for electron transfer *in vitro*, and thus, since the effect of photoreduction appeared also at physiologically relevant concentrations of ATP,[150] also *in vivo*. This then explains the discrepancy between *in vivo* and *in vitro* photochemical activity:[16] While the interruption of the trp triad does, indeed, negatively impact the photochemical activity of cry2 *in vivo*, the presence of ATP *in vitro* causes alternate electron pathways bypassing the triad to become accessible, restoring photoactivity even in the absence of a functional triad.

### 6.4.3 THE EFFECT OF THE Y399F MUTATION

Candidates for alternate pathways can be immediately suggested based on the *A. thaliana* cry1 crystal structure.[60] These include W331 and W376, situated 9.5 Å and 13.5 Å from W321A and 10.7 Å and 7.7 Å from W397, respectively. The latter of these has already been shown to form a pathway W376–W374–W397–FAD in cryDASH.[66] A second, interesting possibility can be seen in the structure of *A. thaliana* cry1 with added ATP (pdb code 1U3D[60]), where the adenine moiety of ATP is situated within 11 Å of the FAD chromophore's isoalloxacine ring. It is

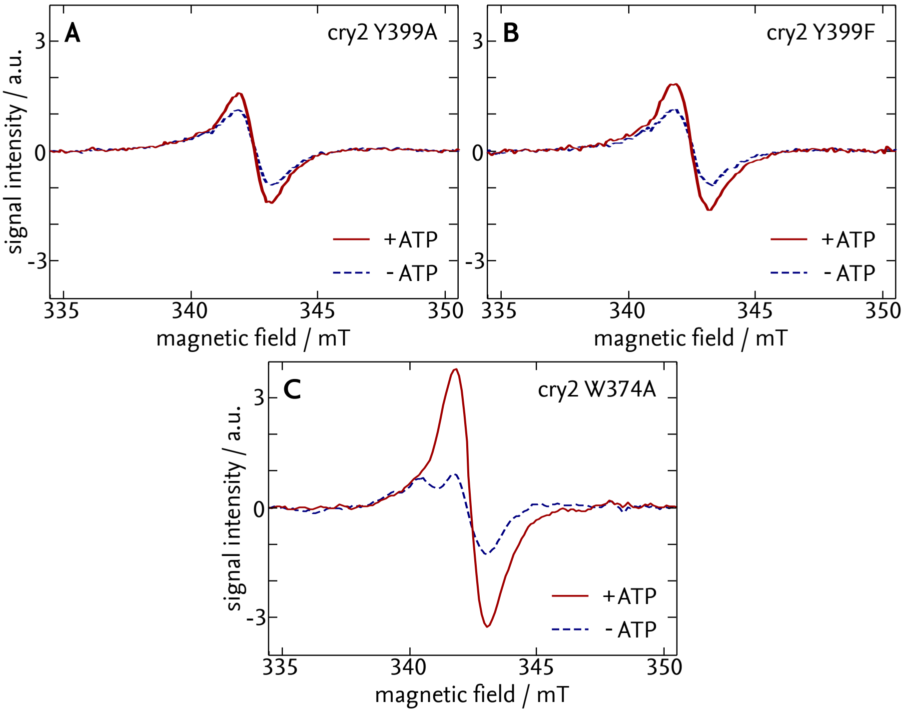

Figure 6.35. – **Continuous-wave EPR spectra of isolated cry2 Y399A/F without (blue, dashed) and with 10 mM ATP added (red, solid).** Spectra have been scaled relative to each sample's ATP-less intensity. Both cry2 Y399A (A) and cry2 Y399F (B) show an ATP effect that is much smaller than that of W374A (C, taken from Fig. 6.33).

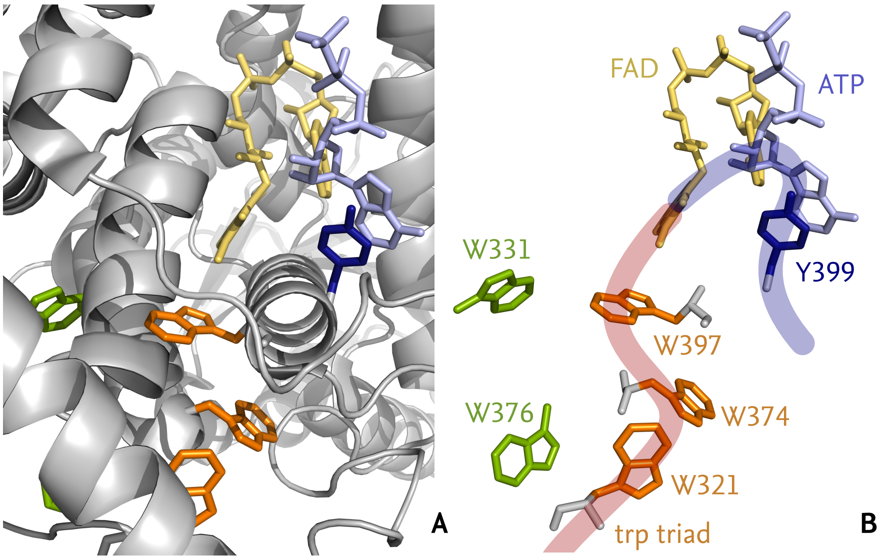

Figure 6.36. – **Alternate electron pathways in cry2.** The pathway along the trp triad is shown in red. Binding of ATP opens an additional pathway to the flavin involving the adenine moiety of ATP and Y399 (blue). Potential further pathways could involve W376 and W331 (green). The structure shown is from cry1, pdb 1U3D.[60] The cry2 ATP binding site is, with the exception of N356 (D359 in cry1) and R289 (K292 in cry1), strongly conserved.

therefore suitably positioned to form an alternate pathway to the nearby redox-active surface residue Y399 (Y402 in cry1).

The existence of this pathway was investigated by repeating the cw EPR experiments on purified protein with the two mutants cry2 Y399A and cry2 Y399F (Fig. 6.35). The spectra of APT-less Y399A (Fig. 6.35A, blue) and Y399F (Fig. 6.35B, blue) samples have been normalised to that of ATP-less W374A (Fig. 6.35C, blue), shown for comparison. While addition of 10 mM ATP produces a small signal increase in both samples (Fig. 6.35A and B, red), the effect is drastically reduced when compared to that of W374A (Fig. 6.35C, red).

Since replacing Y399 was shown not to negatively impact ATP binding,[150] this is directly indicative of a lessened ATP effect, demonstrating that Y399 forms part of at least one of the alternate pathways potentiated by ATP. Figure_6.36 shows the flavin moiety with the trp triad (orange) and the newly identified Y399F (blue) electron transfer pathway.

These results demonstrate that the *in vivo* properties of cryptochrome differ markedly from what is observed in an *in vitro* context and thus shed light on the long-standing dispute about the functional relevance of flavin photoreduction and the trp triad by identifying ATP and other small metabolites as responsible for restoring photochemical activity *in vivo* in protein variants that lack such capabilities *in vitro*, by effectively tuning the protein for maximal electron transfer efficiency over multiple independent pathways. It should be noted that this work by no means excludes additional electron pathways or indeed mechanisms by which the intracellular environment may tune the FAD cofactor's photochemistry, as both the residual flavin radical signal in the absence of ATP observed in W374A cw EPR experiments and in W321A in trEPR experiments, as well as the residual ATP effect in Y399F and Y399A point to the existence of other potentiating agents.

Meanwhile, emerging evidence suggests that the feature of cryptochrome activation by metabolites such as ATP may very well be a general feature, as mutants without a functional trp triad in Dm-cry show photoreduction[172,177,178] and biological signalling function *in vivo*,[72,73] but do not photoreduce *in vitro*.[72,73]

# CHAPTER 7.

# CONCLUSION AND OUTLOOK

## CHANNELRHODOPSIN-2

After the demonstration of its activity as a light-gated cation channel,[19] channelrhodopsin-2 has received widespread attention due to its potential for applications in neurophysiology, where it could be envisioned to optically control in-cell processes like action potentials.[179] Via the crystal structure of a ChR1-ChR2 hybrid,[90] the overall arrangement of ChR2 as a dimer is known, while infrared difference spectroscopy demonstrated large changes of the tertiary structure in various intermediate states of the photocycle.[180,181] However, a more detailed knowledge of the structural changes that accompany the opening of the channel is still lacking.

This study sought to address this using SDSL and ELDOR on multiple ChR2 mutants. Cysteine 128 was replaced by threonine throughout, resulting in variants that accumulate the conducting state $P_3^{520}$ instead of the desensitised state $P_4^{480}$.[96,97,157] Of the nine naturally occurring cysteines in ChR2, cysteine 79 in the loop connecting helices A and B, close to helix B, was found to be essential for protein expression and was therefore used as the initial labelling position. Two further variants, containing additional spinlabels at C208 at the cytoplasmic end of helix F and Q117C, on the extracellular side of helix C, respectively, were also investigated.

The C1C2 structure is the only point of reference, thus a direct evaluation of the observed distances is difficult. The distances observed for the closed state of ChR2 in all three variants were fully compatible with those determined from the crystal structure of C1C2, demonstrating that this structure is indeed a valid template for further structural studies on ChR2.

In the initial experiments of this study, the resolution of the distance distribution was hampered mainly due to the presence of protein aggregates. Nonetheless, upon illumination, a clear increase of the C79–C79 distance could be observed in the singly labelled variant, as well as a global shift of the distribution towards larger distances in the variant containing labels at C79 and C208, indicating an increase of the C208–C208 distance as well. By reconstituting the protein in nanodiscs,[158] the problem of protein aggregation could be eliminated, greatly enhancing the resolution of later distance distributions determined for variants containing only labels at C79 as well as at C79 and Q117C. Thus, it could be shown that the C79–C79 distance increases from 3.6 nm to 4.4 nm upon illumination, while the Q117C–Q117C distance does not change significantly.

Together, these results indicate that in the open state of ChR2, both helix B and helix F shift outwards relative to the closed state, a result that is in line with previous results from BR and SRII[100–102] for the movement of helix F, and results from BR in purple membranes[162–166] for the movement of helix B. Thus the major structural changes upon illumination and opening of the channel appear to be conserved throughout different microbial rhodopsins. A similar ELDOR study by SATTIG *et al.*[182] performed on variants lacking the C128T mutation, which therefore accumulate the desensitised state $P_4^{480}$, found the same structural changes as observed for $P_3^{520}$, despite that fact that $P_4^{480}$ is non-conducting. Therefore, contrary to the opening of the channel, its closing requires only small structural changes in the channel interior, as has been inferred from time-resolved FTIR experiments.[95]

An interesting observation that bears further study is that, even under saturating illumination conditions, the distance distribution of illuminated ChR2-C79 is bimodal with contributions from the open as well as the closed state. However, crucially, no intermediate distances from ChR2 dimers where only one monomer resides in the open state. While this could be due to a fraction of inactive ChR2, it could also indicate cooperativity between the monomers. Light titration experiments using samples that are deliberately only partially illuminated are planned to distinguish between these two cases.

While the problem of protein aggregation has been solved by the reconstitution into nanodiscs a central limiting factor for the interpretation of spinlabel distance distributions in ChR2 remains: The likely unavoidable presence of cysteine C79, yielding at least four labels per dimer in any future spinlabelled protein variant. Additionally, while the fact that the Q117C–Q177C distance does not change significantly would make this position ideal for triangulation, drawing meaningful conclusions from a sample containing six labels is not feasible. Absent C79-less variants, experimentally suppressing the C79–C79 distance is therefore of utmost importance. Fortunately, C79 is highly accessible, so that it is possible to use differential accessibility to selectively label only part of the protein in variants where the second position is comparatively inaccessible. This can be done, for example by blocking C79 with a Förster resonance energy transfer (FRET) marker before, or selectively reducing the label at C79 after spin-labelling. In fact, preliminary experiments tracking the EPR signal intensity of ChR2 labelled at C79 and C208 over time during reduction with ascorbic acid show a biexponential signal decay, with time constants of $(18 \pm 1)$ min and $(200 \pm 10)$ min for the fast and the slow component, respectively. Whether these two components correspond to the labels at C79 and C208, respectively, will be demonstrated using ELDOR spectroscopy.

While this would limit further investigations to positions with low accessibility, it would still pave the way for a more detailed study of the conformational changes associated with the opening of the channel. Of interest as well would be the incorporation of the D156C mutation, which is reported to cause accumulation of $P_2^{390}$[97,183] into the exiting variants. If successful, this would make a further intermediate in the ChR2 photocycle accessible to structural analysis using EPR.

## LOV PROTEINS

LOV blue-light photoreceptor domains have long been a focus of research, due to their ubiquity in nature, as well as their capability of interfacing with a wide range of effector domains. The latter in particular has implications for synthetic biology, as it opens up the possibility of artificially coupling a LOV domain to a target effector domain, creating a "designer protein". Recently, the artificial SHK protein YF1, consisting of the LOV domain from *B. subtilis* YtvA and the histidine kinase domain from *Bradyrhizobium japonicum* FixL has been developed.[8] Due to the availability of both a functional assay for this protein[53] and a crystal structure,[9] all work related to LOV proteins was based on this protein.

This study focused on two aspects of the LOV domain photocycle, one, the question of how the initial photoreduction of the flavin cofactor leads to the activation of the protein's effector domain and two, what effect causes the LOV domain's extraordinarily wide range of photocycle kinetics.

**The conformation of the signalling state** The first question, how the information of the flavin's photoreduction is transmitted to the effector domain, was addressed using intra-protein distance measurements via SDSL and ELDOR. It has been shown that LOV proteins do not undergo large-scale conformational changes upon light excitation,[50,52,184] making it necessary to target residues close to suspected sites of conformational changes. Based on the crystal structure, 10 sites were chosen: Two (Q44 and E55) in the YtvA LOV domain close to the N-terminus, three (D71, N84, and P87) in or close to the outermost α-helix, two (Q93 and M101) close to the linker region and three sites (Q130, A134 and V144) along the linker helices themselves.

ELDOR measurements of YF1 in the dark state yielded distance distributions in good agreement with the crystal structure for the variants Q44C, E55C, D71C, N84C, P87C and M101C, but wholly incompatible for Q93C, Q130C, A134C and V144C. The distance distribution gathered for the labels attached to the linker in particular were incompatible not only with the crystal structure, but with the motif of a coiled-coil linker in general. In the case of Q93C and Q130C, the protein's function was disturbed after labelling, indicating a disturbance of the protein structure by the label, as evidenced by the ELDOR measurements. For the remaining positions it is likely that only a non-functional fraction of the protein was labelled.

Of the fully functional variants, comparison of distances obtained from the protein's active state with the dark state showed increasing mean distances in D71C, N84C, P87C and M101C, while both Q44C and E55C showed no change upon illumination, indicating that the N-terminal region of the LOV domain remains fixed while the β-sheets at the C-terminus twist apart slightly. This marks the first time conformational changes localised at individual residues have been observed in LOV domains.

The changes in distance observed in the ELDOR experiments were translated to conformational changes using ENM and RBD simulations. The resulting model structures indicate that the observed changes in distances can indeed be explained by a twisting apart of the two monomer's β-sheets at the LOV domain's C-terminus, expressed in the models through a movement of I126 connecting the LOV domain to the linker by between 0.17 nm and 0.31 nm. This translates into a separation of the two individual linker helices by 0.17 nm, putting stress on the coiled-coil helices. Thus, signal transmission from LOV to effector domain would be achieved via mechanical force on the interconnecting helices.

The sparsity of available constraints in combination with the small observed changes in distance does not allow for more than qualitative conclusions. Nonetheless, knowledge of the precise structural changes responsible for signal transmission from LOV to effector domain has so far been completely lacking. Thus, the data presented here gives a first indication of a likely mechanism and forms an ideal basis for more targeted studies.

One way to address these issues is investigating more labelling positions, and further studies in this direction are already planned. Variants D76C and D115C are in preparation.

**LOV photocycle kinetics** To address the second question, the structural basis for LOV domains wide range of photo cycle kinetics, the flavin itself was employed as a spin probe by mutationally blocking the formation of the Cysteinyl-C4a-adduct. The hyperfine couplings of the flavin's protons to the unpaired electron's spin were used as a probe for the protein's conformational energy landscape. In particular, the C8α methyl group's mobility, as detected by ENDOR, proved to be highly sensitive to residue exchange in its vicinity. Four variants carrying mutations of residues close to this group, YF1 C62A, C62A/L82I, N37C/C62A and N37C/C62A/L82I, as well their analogues in AsLOV2, AsLOV2 C450A/I470L, C450A, N425C/C450A/I470L and N425C/C450A, were investigated at temperatures ranging from 5 K to 120 K. All showed a different temperature dependence of the C8α methyl group's mobility, with variations containing cysteine showing higher methyl group mobility than those containing asparagine, and variants containing isoleucine showing higher mobility than those containing leucine.

Most importantly, these changes in mobility were clearly correlated with changes in the dark state recovery rate of the protein, with higher methyl group mobility indicating a faster dark recovery. Such an effect had been previously reported for a pair of AsLOV2 variants.[34] This study extends this finding to a more general motif of dark recovery kinetics in LOV domains.

A causal relationship between these two effects is unlikely given the differences in the temperature (22 ℃ versus $<120$ K) involved. Rather, these effects point towards the changes in hydrophobic packing of the flavin cofactor being responsible both for a more or less sterically confined methyl group and greater or lesser solvent accessibility of the flavin, aiding or hindering abstraction of the proton attached to N5 in the active state, thus modulating the dark recovery rates.

Simulations of the spectra revealed the existence of different protein conformations with different activation energies for the mobile-to-hindered transition of the C8$\alpha$ methyl group. This was evidenced by the fact that more than half of the variants did not show a smooth transition from mobile to sterically hindered methyl group, but would, after an initial decrease, remain at a constant fraction of the mobile C8$\alpha$ over a wide temperature range, even down to 5 K. Additionally, the simulations made the extraction of the angle of the immobile methyl group relative to the flavin's $\pi$-system possible, which was previously shown to be sensitive to residue exchanges as well.[34] In particular, the variants containing cysteine showed an orientation of one of the methyl group' protons aligned almost in parallel with the $\pi$-system, while variants containing asparagine had the proton aligned almost perpendicularly. Leucine-to-isoleucine variants had no significant effect on the alignment. Both findings reveal the hyperfine coupling of the C8$\alpha$ methyl group to be an extraordinarily sensitive probe for the conformational energy landscape of LOV domains.

With the exception of the methyl group orientation and the relative intensities of signals from mobile and sterically hindered methyl groups, different residues as well as different LOV domains had little effect on the spectra. This implies that the simulation data obtained here can be easily repurposed for measurements under different conditions. This result was utilised for the measurement of a single oocyte injected with the photoadduct-inhibited YF1 C62A. Obviously, spectra obtained from a single cell are limited in SNR, however they could still be simulated using the simulation system obtained from the *in vitro* experiments.

The spectra showed a distinctly different methyl group orientation than that found in the isolated protein. Due to the limited SNR, it was not possible to distinguish between a single, different orientation and a superposition of many different orientations. Therefore, there are two possible interpretations of this result: Either the changed solvent when going from an *in vitro* to a cell environment causes a slight rearrangement of the flavin's hydrophobic packing, giving rise to a different methyl group orientation, or the cell environment confers an additional degree of conformational freedom to the protein, resulting in many different superimposed orientations. An additional possibility is that the flavin itself is, by way of its surface-exposed side chain, slightly reoriented due to interaction with the solvent. One of the advantages single cell experiments have over standard experiments on a cell ensemble is in this case that an averaging due to variations in the solvent can be excluded.

Being able to adapt a sensor's photocycle kinetics to a target application has large implications for the fields of bioengineering and synthetic biology. The correlation between dark recovery kinetics and methyl group mobility makes ENDOR spectroscopy an ideal method for investigating such manipulations in contexts like *in vivo*, where direct measurements of the recovery rates might not be possible. Strikingly, all these effects were conserved across LOV domains, as the AsLOV2 variants, derived from a plant LOV2 domain, behaved exactly as their YF1 counterparts, derived from a bacterial LOV domain, revealing an astonishing conservation of functional and structural motifs within the LOV family of proteins. Thus, it is likely that results obtained for one LOV domain can directly be transferred to others, making manipulations of photocycle kinetics both predictable and reliable.

However, the experiments on single oocytes indicate that YF1 might behave distinctly differently *in vivo* than *in vitro*. Future flavin ENDOR experiments will therefore focus on the investigation of YF1 variants in an *in vivo* context, both in cell ensembles and individual cells.

## CRYPTOCHROMES

Another area of research is the investigation of cryptochromes, where discrepancies between results obtained *in vivo* and *in vitro* have recently gotten a lot of attention.. It was long thought that cryptochrome activity is induced by the photoreduction of its flavin chromophore by way of electron transfer from the solvent to the flavin along a highly conserved chain of trp residues (W321, W374 and W397 in cry2), termed the trp triad. Recently, however, experiments have shown that cry2 variants without a functional trp triad showed no photoreduction *in vitro*, while still being biologically active *in vivo*.[16]

This study sought to address this seeming contradiction by way of EPR, since the flavin radical produced by photoreduction is readily observed even in whole cell samples. First, cry2 variants with the three trp triad tryptophans replaced by alanine and phenylalanine, namely cry2 W321A, W321F, W374A, W374F, W397A and W397F as well as cry2 wt, were investigated *in vivo* using cw EPR. As has been well established in the literature,[14,15] cry2 wt showed a clear flavin radical signal. Strikingly, with the exception of cry2 W397F, all mutant variants showed a clear signal above background as well, despite them lacking a functional trp triad.

In particular, cry2 W374A, which showed no photoreduction *in vitro*,[16] showed a robust radical signal *in vivo*.

Cw EPR experiments performed on isolated proteins revealed that the addition of ATP drastically enhanced the flavin radical signal after illumination in cry2 W321A and W374A. While the existence of alternative electron pathways has been previously shown,[66,175] this result demonstrates that the efficiency of these alternate pathways can be modulated by small metabolites like ATP.

To address the question of whether the increase in signal is due to changes in the lifetime of the photoreduced flavin, which would make the radical accumulate more easily, leading to a signal increase, or due to a direct change of the photoreduction's quantum yield, isolated cry1 and cry2 wt as well as cry2 W321A and W374A were measured with transient EPR, to detect the transient radical pair formed after illumination directly, both in the presence and absence of added ATP. In the absence of ATP, both cry1 and cry2 wt show a significant transient radical pair signal, as was to be expected from studies performed on cry-DASH[66] and cry2.[171] The W321A variant still showed some radical pair signal, albeit at a drastically reduced quantum yield, indicative of the presence of alternative transfer pathways. This signal, though likely still present, dropped below the detection limit in W374A. Upon the addition of ATP, quantum yield of all variants was significantly enhanced, indicating that the presence of ATP does indeed enhance the forward electron transfer's yield itself. The effect was largest in W374A and W321A, which, since they are both lacking the traditional trp triad, leads to the conclusion that ATP potentiates other pathways unrelated to the trp triad.

There are multiple candidate tyrosines and tryptophans for alternate transfer pathways, including Y399. A variant carrying the mutations Y399F and Y399A was expressed and measured *in vitro* using cw EPR, again both in the presence and absence of ATP. Interestingly, both variants showed a greatly reduced ATP effect when compared to both wt protein and variants W374A and W321A. This is somewhat surprising, since previously demonstrated alternate pathways still involved the trp triad at least in part, while Y399 is situated remote from it.

These experiments resolve the conflict between *in vivo* and *in vitro* data by demonstrating that mutants lacking a functional trp triad undergo photoreduction in a cellular context, indicating that only limited conclusions about photochemical processes in cryptochromes *in vivo* can be drawn from experiments *in vitro*.

Additionally, they identify a new mechanism of regulation of the cryptochrome photoreduction, in which metabolites like ATP potentiate additional electron transfer pathways, thereby increasing the transfer's quantum yield.

Further, a new pathway activated by ATP can be identified, where ATP bound with its alanine moiety situated close to both the FAD cofactor and the surface exposed tyrosine Y399 apparently bridges the two, creating an additional electron path entirely separate from the trp triad. Given these findings as well as previously published results[66,175] on pathways not involving the entire trp triad, it seems unlikely that there are individual pathways that are switched on or off by the presence of ATP. Rather, it is likely that binding of ATP confers additional conformational flexibility to the protein, generally increasing the likelihood of an electron being transferred along an atypical pathway that is suppressed in the more ordered conformation *in vitro*.

This paints a very similar picture to that discussed for methyl group rotations in the context of LOV domain. A reorientation of the FAD side chain in cry2 examined *in vivo* has been reported.[171] It would therefore be interesting to try and identify conformational changes or conformational flexibility by performing similar experiments using the mutants investigated here, both *in vivo* and *in vitro* with and without added ATP.

## SUMMARY

In sum, this work has validated the C1C2 structure[90] as a template for the structure of ChR2, as well as provided initial evidence for the structural changes involved in the opening of the channel of ChR2, changes that appear to be conserved despite the different lateral arrangement of the TM helices in ChR2 compared to other microbial rhodopsins. Additionally, comparison of results obtained here for the conductive state $P_3^{520}$ with results by SATTIG *et al.*[182] for $P_4^{480}$ find these two states to be identical in terms of their tertiary structure, indicating the closing of the channel involves only small structural changes inside it.

For LOV domains, this work has provided tentative evidence for a structural model of signal transmission between a LOV domain and the coupled effector domain, in which a slight moving apart of the two LOV monomers exerts a force on the coiled-coil helices linking the receptor and effector domains. Using ENDOR spectroscopy, a clear correlation between the packing of the flavin chromophore and the dark state recovery rate could be demonstrated. Employing the flavin's C8$\alpha$ methyl group's mobile and sterically hindered state as a marker, one can identify small conformational changes in the chromophore's vicinity and chart, to some degree, the conformational energy landscape. Applied to measurements of YF1 in a single oocyte, this method showed that the conformation of the flavin's environment differs *in vitro* and *in vivo*, with the methyl group adopting different conformations in the two environments. This emphasises the importance of verifying results obtained *in vitro* in an *in vivo* context.

A similar behaviour was observed in cryptochromes, where EPR experiments could resolve the apparent contradiction of variants that, lacking the conserved trp triad, were not photoreducible *in vitro* nonetheless showed biological activity *in vivo* by demonstrating the photoreduction of those same variants in a cellular context. Cellular ATP was found to mediate this effect by potentiating the efficiency of additional electron transfer pathways. One of the pathways, involving the surface-exposed tyrosine Y399, could be identified, although the total electron transfer quantum yield in a cellular context is most likely the result of multiple pathways, enabled by ATP-induced conformational flexibility.

Altogether, this works provides new insights into *in vivo* effects and structural changes of three classes of proteins, that are of high scientific interest due to their widespread occurence in nature as well as due to potential applications. In addition it shows the versatility of advanced EPR techniques to elucidate these mechanisms.

# APPENDIX A.

# ADDITIONAL DATA

TABLE A.1. – **Hyperfine parameters of YF1 flavin in oocytes**. All values in MHz. $H8_{a,b,c}$ are individual protons, $H8_m$ is the mobile H8α coupling, $H8_i$ the semi-mobile.

| Variant | Proton | $a_{iso}$ | $a_{XX}$ | $a_{YY}$ | $a_{ZZ}$ | linewidth |
|---|---|---|---|---|---|---|
| YF1 | H6 | 5.30 | 3.60 | 6.20 | 6.20 | 0.45 |
| C62A | $H1'_a$ | 5.80 | 4.10 | 5.40 | 7.90 | 0.60 |
| oocytes | $H1'_b$ | 8.30 | 6.40 | 7.40 | 10.60 | 0.65 |
| | $H8\alpha_m$ | 7.80 | 7.03 | 7.42 | 8.96 | 0.30 |
| | $H8\alpha_a$ | 10.53 | 9.33 | 10.33 | 12.93 | 0.85 |
| | $H8\alpha_b$ | 11.96 | 10.59 | 11.69 | 13.59 | 0.55 |
| | $H8\alpha_c$ | 0.91 | −0.29 | 0.51 | 2.51 | 0.65 |
| | $H8\alpha_i$ | 11.50 | 8.00 | 12.00 | 14.50 | 1.00 |

Table A.2. – **Hyperfine parameters of YF1 flavin.** All values in MHz. $H8_{a,b,c}$ are individual protons, $H8_m$ is the mobile H8α coupling, $H8_i$ the semi-mobile.

| Variant | Proton | $a_{iso}$ | $a_{XX}$ | $a_{YY}$ | $a_{ZZ}$ | linewidth |
|---|---|---|---|---|---|---|
| YF1<br>C62A | H6 | 5.30 | 3.60 | 6.20 | 6.20 | 0.45 |
| | $H1'_a$ | 6.00 | 4.30 | 5.60 | 8.10 | 0.60 |
| | $H1'_b$ | 8.30 | 6.40 | 7.40 | 10.60 | 0.65 |
| | $H8\alpha_m$ | 7.54 | 6.77 | 7.16 | 8.70 | 0.30 |
| | $H8\alpha_a$ | 9.72 | 8.52 | 9.52 | 12.12 | 0.85 |
| | $H8\alpha_b$ | 12.43 | 11.06 | 12.16 | 14.06 | 0.55 |
| | $H8\alpha_c$ | 0.47 | −0.73 | 0.07 | 2.07 | 0.65 |
| | $H8\alpha_i$ | 11.50 | 8.00 | 12.00 | 14.50 | 1.00 |
| YF1<br>C62A/L82I | H6 | 5.10 | 3.40 | 6.00 | 6.00 | 0.45 |
| | $H1'_a$ | 6.00 | 4.30 | 5.60 | 8.10 | 0.60 |
| | $H1'_b$ | 8.30 | 6.40 | 7.40 | 10.60 | 0.65 |
| | $H8\alpha_m$ | 7.54 | 6.77 | 7.16 | 8.70 | 0.30 |
| | $H8\alpha_a$ | 9.80 | 8.40 | 9.30 | 11.70 | 0.65 |
| | $H8\alpha_b$ | 12.37 | 11.00 | 12.10 | 14.00 | 0.55 |
| | $H8\alpha_c$ | 0.45 | −0.75 | 0.05 | 2.05 | 0.65 |
| | $H8\alpha_i$ | 11.50 | 8.00 | 12.00 | 14.50 | 1.00 |
| YF1<br>N37C/C62A | H6 | 5.10 | 3.40 | 6.00 | 6.00 | 0.45 |
| | $H1'_a$ | 6.00 | 4.30 | 5.60 | 8.10 | 0.60 |
| | $H1'_b$ | 8.30 | 6.40 | 7.40 | 10.60 | 0.65 |
| | $H8\alpha_m$ | 7.54 | 6.77 | 7.16 | 8.70 | 0.30 |
| | $H8\alpha_a$ | 14.37 | 12.97 | 13.87 | 16.27 | 0.65 |
| | $H8\alpha_b$ | 2.04 | 0.67 | 1.77 | 3.67 | 0.55 |
| | $H8\alpha_c$ | 6.22 | 5.02 | 5.82 | 7.82 | 0.65 |
| | $H8\alpha_i$ | 11.50 | 8.00 | 12.00 | 14.50 | 1.00 |
| YF1<br>N37C/C62A/L82I | H6 | 5.10 | 3.40 | 6.00 | 6.00 | 0.45 |
| | $H1'_a$ | 6.00 | 4.30 | 5.60 | 8.10 | 0.60 |
| | $H1'_b$ | 8.30 | 6.40 | 7.40 | 10.60 | 0.65 |
| | $H8\alpha_m$ | 7.54 | 6.77 | 7.16 | 8.70 | 0.30 |
| | $H8\alpha_a$ | 14.41 | 13.01 | 13.91 | 16.31 | 0.65 |
| | $H8\alpha_b$ | 2.13 | 0.76 | 1.86 | 3.76 | 0.55 |
| | $H8\alpha_c$ | 6.08 | 4.88 | 5.68 | 7.68 | 0.65 |
| | $H8\alpha_i$ | 11.50 | 8.00 | 12.00 | 14.50 | 1.00 |

TABLE A.3. – **Hyperfine parameters of AsLOV2 flavin**. All values in MHz. $H8_{a,b,c}$ are individual protons, $H8_m$ is the mobile H8α coupling, $H8_i$ the semi-mobile.

| Variant | Proton | $a_{iso}$ | $a_{XX}$ | $a_{YY}$ | $a_{ZZ}$ | linewidth |
|---|---|---|---|---|---|---|
| AsLOV2 C450A | H6 | 5.10 | 3.40 | 6.00 | 6.00 | 0.45 |
| | $H1'_a$ | 6.00 | 4.30 | 5.60 | 8.10 | 0.60 |
| | $H1'_b$ | 8.30 | 6.40 | 7.40 | 10.60 | 0.65 |
| | $H8\alpha_m$ | 7.86 | 7.09 | 7.48 | 9.02 | 0.30 |
| | $H8\alpha_a$ | 10.47 | 9.07 | 9.97 | 12.37 | 0.65 |
| | $H8\alpha_b$ | 12.83 | 11.46 | 12.56 | 14.46 | 0.55 |
| | $H8\alpha_c$ | 0.28 | −0.92 | −0.12 | 1.88 | 0.65 |
| | $H8\alpha_i$ | 11.50 | 8.00 | 12.00 | 14.50 | 1.00 |
| AsLOV2 C450A/I470L | H6 | 5.10 | 3.40 | 6.00 | 6.00 | 0.45 |
| | $H1'_a$ | 6.00 | 4.30 | 5.60 | 8.10 | 0.60 |
| | $H1'_b$ | 8.30 | 6.40 | 7.40 | 10.60 | 0.65 |
| | $H8\alpha_m$ | 7.86 | 7.09 | 7.48 | 9.02 | 0.30 |
| | $H8\alpha_a$ | 9.44 | 8.24 | 9.24 | 11.84 | 0.85 |
| | $H8\alpha_b$ | 12.72 | 11.35 | 12.45 | 14.35 | 0.55 |
| | $H8\alpha_c$ | 1.43 | 0.23 | 1.03 | 3.03 | 0.65 |
| | $H8\alpha_i$ | 11.50 | 8.00 | 12.00 | 14.50 | 1.00 |
| AsLOV2 N425C/C450A | H6 | 5.10 | 3.40 | 6.00 | 6.00 | 0.45 |
| | $H1'_a$ | 6.00 | 4.30 | 5.60 | 8.10 | 0.60 |
| | $H1'_b$ | 8.30 | 6.40 | 7.40 | 10.60 | 0.65 |
| | $H8\alpha_m$ | 7.86 | 7.09 | 7.48 | 9.02 | 0.30 |
| | $H8\alpha_a$ | 15.12 | 13.72 | 14.62 | 17.02 | 0.65 |
| | $H8\alpha_b$ | 2.00 | 0.63 | 1.73 | 3.63 | 0.55 |
| | $H8\alpha_c$ | 6.45 | 5.25 | 6.05 | 8.05 | 0.65 |
| | $H8\alpha_i$ | 11.50 | 8.00 | 12.00 | 14.50 | 1.00 |
| AsLOV2 N425C/C450A/I470L | H6 | 5.10 | 3.40 | 6.00 | 6.00 | 0.45 |
| | $H1'_a$ | 6.00 | 4.30 | 5.60 | 8.10 | 0.60 |
| | $H1'_b$ | 8.30 | 6.40 | 7.40 | 10.60 | 0.65 |
| | $H8\alpha_m$ | 7.94 | 7.17 | 7.56 | 9.10 | 0.30 |
| | $H8\alpha_a$ | 14.64 | 13.24 | 14.14 | 16.54 | 0.65 |
| | $H8\alpha_b$ | 2.75 | 1.38 | 2.48 | 4.38 | 0.55 |
| | $H8\alpha_c$ | 6.45 | 5.25 | 6.05 | 8.05 | 0.65 |
| | $H8\alpha_i$ | 11.50 | 8.00 | 12.00 | 14.50 | 1.00 |

# APPENDIX B.

# PUBLICATIONS

## ELEMENTS OF THIS WORK THAT HAVE BEEN PUBLISHED

ELDOR and cw data from proteins in detergent presented in Section 6.1, *ELDOR experiments on spin-labelled ChR2*:

N. KRAUSE, C. ENGELHARD, J. HEBERLE, R. SCHLESINGER, R. BITTL, "Structural differences between the closed and open states of channelrhodopsin-2 as observed by EPR spectroscopy.", *FEBS Lett.* **Oct. 2013**, *587*, 3309–13

Data presented in Section 6.3, *ENDOR experiments on YF1 and AsLOV2*, excluding simulations and in-cell experiments:

R. P. DIENSTHUBER, C. ENGELHARD, N. LEMKE, T. GLEICHMANN, R. OHLENDORF, R. BITTL, A. MÖGLICH, "Biophysical, Mutational, and Functional Investigation of the Chromophore-Binding Pocket of Light-Oxygen-Voltage Photoreceptors.", *ACS Synth. Biol.* **Mar. 2014**, *9*, DOI `10.1021/sb400205x`

Data presented in Section 6.4, *The effect of cellular metabolites on the light sensitivity of* A. thaliana *cry2*:

C. ENGELHARD, X. WANG, D. ROBLES, J. MOLDT, L.-O. ESSEN, A. BATSCHAUER, R. BITTL, M. AHMAD, "Cellular metabolites enhance the light sensitivity of Arabidopsis cryptochrome through alternate electron transfer pathways.", *Plant Cell* **Nov. 2014**, *26*, 4519–31

## OTHER PUBLICATIONS

C. ENGELHARD, S. RAFFELBERG, Y. TANG, R. P. DIENSTHUBER, A. MÖGLICH, A. LOSI, W. GÄRTNER, R. BITTL, "A structural model for the full-length blue light-sensing protein YtvA from Bacillus subtilis, based on EPR spectroscopy.", *Photochem. Photobiol. Sci.* **Oct. 2013**, *12*, 1855–63

R. Brosi, R. Bittl, C. Engelhard, “EPR on Flavoproteins.”, *Methods Mol. Biol.* **Jan. 2014**, *1146*, 341–60

A. Hahn, C. Engelhard, S. Reschke, C. Teutloff, R. Bittl, S. Leimkühler, T. Risse, “Structural insights into the incorporation of the Mo cofactor into sulfite oxidase from site directed spin labeling”, *Angew. Chemie - Int. Ed.* **2015**, *in press*, DOI `10.1002/anie.201504772R1`

# ABBREVIATIONS

**3pELDOR** three-pulse ELDOR (pp. 49 f., 54)

**(6-4)** (6-4) pyrimidine-pyrimidone (p. 9)

**ADC** analog-digital converter (p. 37)

**ANM** anisotropic network model (p. 60)

**AsLOV2** phototropin-1 LOV2 domain from *Avena sativa* (pp. 7, 98–100, 102, 104–106, 108 f., 126–128)

***A. thaliana*** *Arabidopsis thaliana* (pp. 2, 119)

**ATP** adenosine triphosphate (pp. 62, 64, 116 f., 119, 121 f., 129–131)

***B. japonicum*** *Bradyrhizobium japonicum* (pp. 1, 8, 125)

**BLUF** blue-light sensor using flavin adenine dinucleotide (p. 5)

**BR** bacteriorhodopsin (pp. 16, 77 f., 124)

***B. subtilis*** *Bacillus subtilis* (pp. 1, 8, 125)

**C1C2** ChR1-ChR2 hybrid (pp. 16, 70 f., 73, 78, 123, 130)

**CCT** C-terminal extension (p. 11)

***C. reinhardtii*** *Chlamydomonas reinhardtii* (pp. 2, 15)

**ChR** channelrhodopsin (pp. 2, 15 f.)

**ChR1** channelrhodopsin-1 (pp. 15 f., 71, 73)

**ChR2** channelrhodopsin-2 (pp. 2, 15 f., 18, 61, 63, 67, 69–71, 73, 75, 77 f., 123–125, 130)

**CPD** cyclobutane pyrimidine dimer (p. 9)

**cry1** cryptochrome-1 (pp. 9–11, 13, 116 f., 119, 121, 129)

**cry2** cryptochrome-2 (pp. 2, 9, 11, 13, 61, 64, 67, 113 f., 116 f., 119, 121, 128–130)

**cw** continuous-wave (pp. 2, 19, 31–33, 35 f., 41, 48, 57 f., 61, 63 f., 77, 113, 116, 119, 121 f., 128 f., 137)

**DEER** double electron-electron resonance (pp. 2, 50, 54, 63)

**DM** n-Decyl-β-D-maltopyranoside (p. 70)

***D. melanogaster*** *Drosophila melanogaster* ()

**Dm-cry** *Drosophila melanogaster* cryptochrome (pp. 13, 122)

**DNA** deoxyribonucleic acid (pp. 5, 10 f.)

**ED** essential dynamics (p. 60)

**ELDOR** electron-electron double resonance (pp. 2, 48, 50 f., 53 f., 58, 61–64, 67, 70, 73, 77–79, 87, 90 f., 123–126, 137)

**ENDOR** electron-nuclear double resonance (pp. 2, 41, 43–47, 60–63, 96, 98, 100, 102, 109, 111 f., 126, 128, 130)

**ENM** elastic network model (pp. 60, 91 f., 94 f., 126)

**EPR** electron paramagnetic resonance (pp. 2, 5, 19 f., 25, 29–35, 37, 41, 57 f., 61–64, 77 f., 109, 111, 113 f., 116 f., 119, 121 f., 124 f., 128–130)

**ESEEM** electron spin-echo envelope modulation (pp. 52 f., 63)

**FAD** flavin adenine dinucleotide (pp. 1, 5, 10 f., 129)

**FID** free induction decay (p. 37)

**FMN** flavin mononucleotide (pp. 5, 7, 104, 113)

**FRET** Förster resonance energy transfer (p. 124)

**FSE** field-swept echo (p. 39)

**FTIR** fourier-transform infrared (pp. 18, 124)

**GNM** gaussian network model (p. 60)

**HEPES** 4-(2-hydroxyethyl)-1-piperazineethanesulfonic acid (p. 61)

**HFC** hyperfine coupling (pp. 41, 44 f.)

**ITP** inosine triphosphate (p. 117)

**LOV** light, oxygen and voltage (pp. 1 f., 5–9, 11, 56, 61 f., 67, 79, 82, 86 f., 90, 92, 94, 96, 98, 105, 108 f., 111 f., 125–128, 130)

**MD** molecular dynamics (pp. 60, 87)

**MES** 2-(N-morpholino)ethanesulfonic acid (p. 70)

**MTSSL** (1-Oxyl-2,2,5,5-tetramethyl-pyrroline-3-methyl) methanethiosulfonate spin label (pp. 56, 58, 67)

**NADH** nicotinamide adenine dinucleotide (p. 117)

**NMR** nuclear magnetic resonance (pp. 20, 37, 41)

**PAS** Per-ARNT-Sim (pp. 6–9)

**QM** quantum-mechanical (p. 105)

**RBD** rigid-body docking (pp. 60, 91 f., 94–96, 126)

**RF** radio frequency (pp. 41, 43–46, 63)

**RMSD** root-mean-square deviation (pp. 64, 74, 93 f., 96)

**SB** Schiff base (p. 16)

**scRP** spin-correlated radical pair (pp. 26 f., 29, 117, 119)

**SDM** site-directed mutagenesis (p. 61)

**SDSL** site-directed spin labelling (pp. 2, 67, 79, 123, 125)

**SHK** sensor histidine kinase (pp. 8, 125)

**SNR** signal-to-noise ratio (pp. 46, 53 f., 57, 70, 86 f., 109, 111, 114, 117, 127)

**SRII** sensory rhodopsin II (pp. 78, 124)

**TM** transmembrane (pp. 16, 67, 78, 130)

**trEPR** transient EPR (pp. 2, 57 f., 63 f., 113, 117, 122)

**trp** tryptophane (pp. 1, 11, 13, 113 f., 117)

**TWT** travelling-wave tube amplifier (pp. 37, 52, 63)

**tyr** tyrosine (p. 117)

**UV/vis** ultraviolet/visual (pp. 7, 75, 77, 98, 117)

**vdW** van-der-Waals (pp. 87 f.)

**wt** wildtype (pp. 9, 16, 64, 67, 91, 96, 98, 105, 113 f., 116 f., 119, 128 f.)

***X. laevis*** *Xenopus laevis* (pp. 61, 109)

# BIBLIOGRAPHY

[1] P. Hegemann, "Algal sensory photoreceptors.", *Annu. Rev. Plant Biol.* **Jan. 2008**, *59*, 167–89 (cit. on pp. 1, 2, 16).

[2] A. Losi, W. Gärtner, "Old chromophores, new photoactivation paradigms, trendy applications: flavins in blue light-sensing photoreceptors.", *Photochem. Photobiol.* **Jan. 2011**, *87*, 491–510 (cit. on pp. 1, 5, 7).

[3] A. Losi, "Flavin-based Blue-Light photosensors: a photobiophysics update.", *Photochem. Photobiol.* **2007**, *83*, 1283–300 (cit. on pp. 1, 5, 8).

[4] B. D. Zoltowski, A. I. Nash, K. H. Gardner, "Variations in protein-flavin hydrogen bonding in a light, oxygen, voltage domain produce non-Arrhenius kinetics of adduct decay.", *Biochemistry* **Oct. 2011**, *50*, 8771–9 (cit. on pp. 1, 5, 7).

[5] J. M. Christie, P. Reymond, G. K. Powell, P. Bernasconi, A. A. Raibekas, E. Liscum, W. R. Briggs, "Arabidopsis NPH1: A flavoprotein with the properties of a photoreceptor for phototropism", *Science (80-. ).* **Nov. 1998**, *282*, 1698–1701 (cit. on pp. 1, 6).

[6] J. Herrou, S. Crosson, "Function, structure and mechanism of bacterial photosensory LOV proteins.", *Nat. Rev. Microbiol.* **Oct. 2011**, *9*, 713–23 (cit. on p. 1).

[7] S. Crosson, S. Rajagopal, K. Moffat, The LOV domain family: Photoresponsive signaling modules coupled to diverse output domains, **2003** (cit. on p. 1).

[8] A. Möglich, R. A. Ayers, K. Moffat, "Design and signaling mechanism of light-regulated histidine kinases.", *J. Mol. Biol.* **Feb. 2009**, *385*, 1433–44 (cit. on pp. 1, 2, 8, 9, 125).

[9] R. P. Diensthuber, M. Bommer, T. Gleichmann, A. Möglich, "Full-length structure of a sensor histidine kinase pinpoints coaxial coiled coils as signal transducers and modulators.", *Structure* **July 2013**, *21*, 1127–36 (cit. on pp. 1, 7–9, 59, 79, 87, 98, 108, 125).

[10] M. Ahmad, A. R. Cashmore, "HY4 gene of A. thaliana encodes a protein with characteristics of a blue-light photoreceptor.", *Nature* **Nov. 1993**, *366*, 162–6 (cit. on pp. 1, 5, 10).

[11] I. Chaves, R. Pokorny, M. Byrdin, N. Hoang, T. Ritz, K. Brettel, L.-O. Essen, G. T. J. van der Horst, A. Batschauer, M. Ahmad, "The cryptochromes: blue light photoreceptors in plants and animals.", *Annu. Rev. Plant Biol.* **Jan. 2011**, *62*, 335–364 (cit. on pp. 1, 5, 11).

[12] C. Lin, T. Todo, "The cryptochromes.", *Genome Biol.* **Jan. 2005**, *6*, 220 (cit. on pp. 1, 10, 11).

[13] K. Brettel, M. Byrdin, "Reaction mechanisms of DNA photolyase", *Curr. Opin. Struct. Biol.* **Dec. 2010**, *20*, 693–701 (cit. on pp. 1, 5, 11).

[14] R. Banerjee, E. Schleicher, S. Meier, R. M. Viana, R. Pokorny, M. Ahmad, R. Bittl, A. Batschauer, "The signaling state of Arabidopsis cryptochrome 2 contains flavin semiquinone", *J. Biol. Chem.* **May 2007**, *282*, 14916–14922 (cit. on pp. 2, 5, 11, 13, 128).

[15] J.-P. P. Bouly, E. Schleicher, M. Dionisio-Sese, F. Vandenbussche, D. Van Der Straeten, N. Bakrim, S. Meier, A. Batschauer, P. Galland, R. Bittl, M. Ahmad, "Cryptochrome blue light photoreceptors are activated through interconversion of flavin redox states", *J. Biol. Chem.* **Jan. 2007**, *282*, 9383–9391 (cit. on pp. 2, 5, 11, 13, 128).

[16] X. Li, Q. Wang, X. Yu, H. Liu, H. Yang, C. Zhao, X. Liu, C. Tan, J. Klejnot, D. Zhong, C. Lin, Arabidopsis cryptochrome 2 (CRY2) functions by the photoactivation mechanism distinct from the tryptophan (trp) triad-dependent photoreduction, **2011** (cit. on pp. 2, 13, 113, 114, 119, 128, 129).

[17] E. Gouaux, R. Mackinnon, "Principles of selective ion transport in channels and pumps.", *Science* **Dec. 2005**, *310*, 1461–5 (cit. on pp. 2, 15).

[18] G. R. Dubyak, "Ion homeostasis, channels, and transporters: an update on cellular mechanisms.", *Adv. Physiol. Educ.* **Dec. 2004**, *28*, 143–54 (cit. on pp. 2, 15).

[19] G. Nagel, T. Szellas, W. Huhn, S. Kateriya, N. Adeishvili, P. Berthold, D. Ollig, P. Hegemann, E. Bamberg, "Channelrhodopsin-2, a directly light-gated cation-selective membrane channel.", *Proc. Natl. Acad. Sci. U. S. A.* **Nov. 2003**, *100*, 13940–5 (cit. on pp. 2, 15, 16, 123).

[20] A. K. Sharma, J. L. Spudich, W. F. Doolittle, "Microbial rhodopsins: functional versatility and genetic mobility.", *Trends Microbiol.* **Nov. 2006**, *14*, 463–9 (cit. on pp. 2, 16).

[21] J. L. Spudich, C. S. Yang, K. H. Jung, E. N. Spudich, "Retinylidene proteins: structures and functions from archaea to humans.", *Annu. Rev. Cell Dev. Biol.* **Jan. 2000**, *16*, 365–92 (cit. on pp. 2, 16).

[22] R. Bittl, C. W. M. Kay, S. Weber, P. Hegemann, "Characterization of a flavin radical product in a C57M mutant of a LOV1 domain by electron paramagnetic resonance.", *Biochemistry* **July 2003**, *42*, 8506–12 (cit. on pp. 2, 5, 98).

[23] R. Brosi, R. Bittl, C. Engelhard, "EPR on Flavoproteins.", *Methods Mol. Biol.* **Jan. 2014**, *1146*, 341–60 (cit. on pp. 2, 138).

[24] W. Briggs, Blue/UV-A receptors: Historical overview, **2006** (cit. on p. 5).

[25] B. D. Zoltowski, K. H. Gardner, "Tripping the light fantastic: Blue-light photoreceptors as examples of environmentally modulated protein-protein interactions", *Biochemistry* **2011**, *50*, 4–16 (cit. on p. 5).

[26] K. S. Conrad, C. C. Manahan, B. R. Crane, "Photochemistry of flavoprotein light sensors.", *Nat. Chem. Biol.* **Oct. 2014**, *10*, 801–9 (cit. on pp. 5, 7).

[27] M. Iseki, S. Matsunaga, A. Murakami, K. Ohno, K. Shiga, K. Yoshida, M. Sugai, T. Takahashi, T. Hori, M. Watanabe, "A blue-light-activated adenylyl cyclase mediates photoavoidance in Euglena gracilis.", *Nature* **Feb. 2002**, *415*, 1047–51 (cit. on p. 5).

[28] E. Huala, "Arabidopsis NPH1: A Protein Kinase with a Putative Redox-Sensing Domain", *Science (80-. ).* **Dec. 1997**, *278*, 2120–2123 (cit. on p. 5).

[29] V. Massey, G. Palmer, "On the Existence of Spectrally Distinct Classes of Flavoprotein Semiquinones. A New Method for the Quantitative Production of Flavoprotein Semiquinones *", *Biochemistry* **Oct. 1966**, *5*, 3181–3189 (cit. on p. 5).

[30] E. Schleicher, S. Weber, *Flavins & Flavoprotein Protocols*, (Eds.: E. Schleicher, S. Weber), Humana Press, Inc, **2012** (cit. on p. 5).

[31] V. Massey in Biochem. Soc. Trans. *Vol. 28*, **2000**, pp. 283–296 (cit. on p. 5).

[32] A. Edwards, General properties of flavins, **2006** (cit. on p. 5).

[33] A. Sancar, "Structure and function of DNA photolyase and cryptochrome blue-light photoreceptors.", *Chem. Rev.* **June 2003**, *103*, 2203–37 (cit. on pp. 5, 11).

[34] R. Brosi, B. Illarionov, T. Mathes, M. Fischer, M. Joshi, A. Bacher, P. Hegemann, R. Bittl, S. Weber, E. Schleicher, "Hindered rotation of a cofactor methyl group as a probe for protein-cofactor interaction.", *J. Am. Chem. Soc.* **July 2010**, *132*, 8935–44 (cit. on pp. 5, 98, 105, 108, 127).

[35] B. L. Taylor, I. B. Zhulin, PAS domains: Internal sensors of oxygen, redox potential, and light, **1999** (cit. on p. 6).

[36] J. H. Morals Cabral, A. Lee, S. L. Cohen, B. T. Chait, M. Li, R. Mackinnon, "Crystal structure and functional analysis of the HERG potassium channel N terminus: A eukaryotic PAS domain", *Cell* **1998**, *95*, 649–655 (cit. on p. 6).

[37] J. Key, M. Hefti, E. B. Purcell, K. Moffat, "Structure of the redox sensor domain of Azotobacter vinelandii NifL at atomic resolution: signaling, dimerization, and mechanism.", *Biochemistry* **Mar. 2007**, *46*, 3614–23 (cit. on p. 6).

[38] L. Aravind, C. P. Ponting, "The GAF domain: an evolutionary link between diverse phototransducing proteins", *Trends Biochem. Sci.* **Dec. 1997**, *22*, 458–459 (cit. on p. 6).

[39] J. R. Nambu, J. O. Lewis, K. A. Wharton, S. T. Crews, "The Drosophila single-minded gene encodes a helix-loop-helix protein that acts as a master regulator of CNS midline development", *Cell* **Dec. 1991**, *67*, 1157–1167 (cit. on p. 6).

[40] W. R. Briggs, "The LOV domain: a chromophore module servicing multiple photoreceptors.", *J. Biomed. Sci.* **July 2007**, *14*, 499–504 (cit. on p. 7).

[41] M. H. Hefti, K.-J. Françoijs, S. C. De Vries, R. Dixon, J. Vervoort, "The PAS fold", *Eur. J. Biochem.* **Mar. 2004**, *271*, 1198–1208 (cit. on p. 7).

[42] M. T. A. Alexandre, T. Domratcheva, C. Bonetti, L. J. G. W. Van Wilderen, R. Van Grondelle, M. L. Groot, K. J. Hellingwerf, J. T. M. Kennis, "Primary reactions of the LOV2 domain of phototropin studied with ultrafast mid-infrared spectroscopy and quantum chemistry", *Biophys. J.* **2009**, *97*, 227–237 (cit. on p. 7).

[43] C. Bauer, C. R. Rabl, J. Heberle, T. Kottke, "Indication for a radical intermediate preceding the signaling state in the LOV domain photocycle", *Photochem. Photobiol.* **2011**, *87*, 548–553 (cit. on p. 7).

[44] A. Pfeifer, T. Majerus, K. Zikihara, D. Matsuoka, S. Tokutomi, J. Heberle, T. Kottke, "Time-resolved fourier transform infrared study on photoadduct formation and secondary structural changes within the phototropin LOV domain", *Biophys. J.* **2009**, *96*, 1462–1470 (cit. on p. 7).

[45] B. D. Zoltowski, B. Vaccaro, B. R. Crane, "Mechanism-based tuning of a LOV domain photoreceptor.", *Nat. Chem. Biol.* **Nov. 2009**, *5*, 827–834 (cit. on p. 8).

[46] M. Kasahara, T. E. Swartz, M. A. Olney, "Photochemical Properties of the Flavin Mononucleotide-Binding Domains of the Phototropins from Arabidopsis, Rice, andChlamydomonas reinhardtii", *Plant ...* **2002**, *129*, 762–773 (cit. on p. 8).

[47] M. Nakasako, D. Matsuoka, K. Zikihara, S. Tokutomi, "Quaternary structure of LOV-domain containing polypeptide of Arabidopsis FKF1 protein.", *FEBS Lett.* **Feb. 2005**, *579*, 1067–71 (cit. on p. 8).

[48] S. Kikuchi, M. Unno, K. Zikihara, S. Tokutomi, S. Yamauchi, "Vibrational assignment of the flavin-cysteinyl adduct in a signaling state of the LOV domain in FKF1.", *J. Phys. Chem. B* **Mar. 2009**, *113*, 2913–21 (cit. on p. 8).

[49] M. Kasahara, M. Torii, A. Fujita, K. Tainaka, "FMN binding and photochemical properties of plant putative photoreceptors containing two LOV domains, LOV/LOV proteins.", *J. Biol. Chem.* **Nov. 2010**, *285*, 34765–72 (cit. on p. 8).

[50] C. Engelhard, S. Raffelberg, Y. Tang, R. P. Diensthuber, A. Möglich, A. Losi, W. Gärtner, R. Bittl, "A structural model for the full-length blue light-sensing protein YtvA from Bacillus subtilis, based on EPR spectroscopy.", *Photochem. Photobiol. Sci.* **Oct. 2013**, *12*, 1855–63 (cit. on pp. 9, 56, 61, 96, 125, 137).

[51] M. Jurk, M. Dorn, A. Kikhney, D. Svergun, W. Gärtner, P. Schmieder, "The switch that does not flip: the blue-light receptor YtvA from Bacillus subtilis adopts an elongated dimer conformation independent of the activation state as revealed by a combined AUC and SAXS study.", *J. Mol. Biol.* **Oct. 2010**, *403*, 78–87 (cit. on p. 9).

[52] M. Jurk, M. Dorn, P. Schmieder, "Blue flickers of hope: Secondary structure, dynamics, and putative dimerization interface of the blue-light receptor YtvA from Bacillus subtilis", *Biochemistry* **Sept. 2011**, *50*, 8163–8171 (cit. on pp. 9, 125).

[53] R. Ohlendorf, R. R. Vidavski, A. Eldar, K. Moffat, A. Möglich, "From dusk till dawn: One-plasmid systems for light-regulated gene expression", *J. Mol. Biol.* **Mar. 2012**, *416*, 534–542 (cit. on pp. 9, 125).

[54] M. Koornneef, E. Rolff, C. Spruit, Genetic control of light-inhibited hypocotyl elongation in Arabidopsis thaliana (L.) Heynh, **1980** (cit. on p. 10).

[55] S. E.-D. El-Assal, C. Alonso-Blanco, A. J. M. Peeters, C. Wagemaker, J. L. Weller, M. Koornneef, "The role of cryptochrome 2 in flowering in Arabidopsis.", *Plant Physiol.* **Dec. 2003**, *133*, 1504–16 (cit. on p. 10).

[56] H. Guo, "Regulation of Flowering Time by Arabidopsis Photoreceptors", *Science (80-. ).* **Feb. 1998**, *279*, 1360–1363 (cit. on p. 10).

[57] Q.-H. Li, H.-Q. Yang, "Cryptochrome signaling in plants.", *Photochem. Photobiol.* **Jan. 2007**, *83*, 94–101 (cit. on pp. 10, 11).

[58] Y. Jiao, H. Yang, L. Ma, N. Sun, H. Yu, T. Liu, Y. Gao, H. Gu, Z. Chen, M. Wada, M. Gerstein, H. Zhao, L.-J. Qu, X.-W. Deng, “A genome-wide analysis of blue-light regulation of Arabidopsis transcription factor gene expression during seedling development.”, *Plant Physiol.* **Dec. 2003**, *133*, 1480–93 (cit. on p. 10).

[59] L. Ma, “Light Control of Arabidopsis Development Entails Coordinated Regulation of Genome Expression and Cellular Pathways”, *PLANT CELL ONLINE* **Dec. 2001**, *13*, 2589–2607 (cit. on p. 10).

[60] C. A. Brautigam, B. S. Smith, Z. Ma, M. Palnitkar, D. R. Tomchick, M. Machius, J. Deisenhofer, “Structure of the photolyase-like domain of cryptochrome 1 from Arabidopsis thaliana.”, *Proc. Natl. Acad. Sci. U. S. A.* **Aug. 2004**, *101*, 12142–7 (cit. on pp. 10, 12, 113, 116, 119, 121).

[61] M. J. Maul, T. R. M. Barends, A. F. Glas, M. J. Cryle, T. Domratcheva, S. Schneider, I. Schlichting, T. Carell, “Crystal structure and mechanism of a DNA (6-4) photolyase.”, *Angew. Chem. Int. Ed. Engl.* **Jan. 2008**, *47*, 10076–80 (cit. on p. 10).

[62] C. P. Selby, A. Sancar, “A cryptochrome/photolyase class of enzymes with single-stranded DNA-specific photolyase activity.”, *Proc. Natl. Acad. Sci. U. S. A.* **Nov. 2006**, *103*, 17696–700 (cit. on p. 10).

[63] C. L. Partch, M. W. Clarkson, S. Ozgür, A. L. Lee, A. Sancar, “Role of structural plasticity in signal transduction by the cryptochrome blue-light photoreceptor.”, *Biochemistry* **Mar. 2005**, *44*, 3795–805 (cit. on p. 11).

[64] H. Wang, L. G. Ma, J. M. Li, H. Y. Zhao, X.-W. Deng, “Direct interaction of Arabidopsis cryptochromes with COP1 in light control development.”, *Science* **Oct. 2001**, *294*, 154–8 (cit. on p. 11).

[65] V. Balland, M. Byrdin, A. P. M. Eker, M. Ahmad, K. Brettel, “What makes the difference between a cryptochrome and DNA photolyase? A spectroelectrochemical comparison of the flavin redox transitions.”, *J. Am. Chem. Soc.* **Jan. 2009**, *131*, 426–7 (cit. on pp. 11, 13).

[66] T. Biskup, K. Hitomi, E. D. Getzoff, S. Krapf, T. Koslowski, E. Schleicher, S. Weber, “Unexpected electron transfer in cryptochrome identified by time-resolved EPR spectroscopy”, *Angew. Chemie - Int. Ed.* **Dec. 2011**, *50*, 12647–51 (cit. on pp. 11, 117, 119, 129, 130).

[67] Z. Zuo, H. Liu, B. Liu, X. Liu, C. Lin, “Blue light-dependent interaction of CRY2 with SPA1 regulates COP1 activity and floral initiation in Arabidopsis.”, *Curr. Biol.* **May 2011**, *21*, 841–7 (cit. on p. 11).

[68] Z.-C. Zuo, Y.-Y. Meng, X.-H. Yu, Z.-L. Zhang, D.-S. Feng, S.-F. Sun, B. Liu, C.-T. Lin, “A study of the blue-light-dependent phosphorylation, degradation, and photobody formation of Arabidopsis CRY2.”, *Mol. Plant* **May 2012**, *5*, 726–33 (cit. on p. 11).

[69] A. Zeugner, M. Byrdin, J.-P. Bouly, N. Bakrim, B. Giovani, K. Brettel, M. Ahmad, “Light-induced electron transfer in Arabidopsis cryptochrome-1 correlates with in vivo function.”, *J. Biol. Chem.* **May 2005**, *280*, 19437–40 (cit. on p. 13).

[70] M. Ahmad, N. Grancher, M. Heil, R. C. Black, B. Giovani, P. Galland, D. Lardemer, “Action spectrum for cryptochrome-dependent hypocotyl growth inhibition in Arabidopsis.”, *Plant Physiol.* **June 2002**, *129*, 774–85 (cit. on p. 13).

[71] V. Herbel, C. Orth, R. Wenzel, M. Ahmad, R. Bittl, A. Batschauer, “Lifetimes of Arabidopsis cryptochrome signaling states in vivo.”, *Plant J.* **May 2013**, *74*, 583–92 (cit. on p. 13).

[72] S. H. Song, N. Öztürk, T. R. Denaro, N. Ö. Arat, Y.-T. Kao, H. Zhu, D. Zhong, S. M. Reppert, A. Sancar, “Formation and function of flavin anion radical in cryptochrome 1 blue-light photoreceptor of monarch butterfly”, *J. Biol. Chem.* **June 2007**, *282*, 17608–17612 (cit. on pp. 13, 122).

[73] N. Öztürk, S. H. Song, C. P. Selby, A. Sancar, “Animal Type 1 cryptochromes: Analysis of the redox state of the flavin cofactor by site-directed mutagenesis”, *J. Biol. Chem.* **Feb. 2008**, *283*, 3256–3263 (cit. on pp. 13, 122).

[74] N. Ozturk, C. P. Selby, Y. Annayev, D. Zhong, A. Sancar, “Reaction mechanism of Drosophila cryptochrome.”, *Proc. Natl. Acad. Sci. U. S. A.* **Jan. 2011**, *108*, 516–21 (cit. on p. 13).

[75] N. Ozturk, C. P. Selby, D. Zhong, A. Sancar, “Mechanism of photosignaling by Drosophila cryptochrome: role of the redox status of the flavin chromophore.”, *J. Biol. Chem.* **Feb. 2014**, *289*, 4634–42 (cit. on p. 13).

[76] F. Tombola, M. M. Pathak, E. Y. Isacoff, “How does voltage open an ion channel?”, *Annu. Rev. Cell Dev. Biol.* **Jan. 2006**, *22*, 23–52 (cit. on p. 15).

[77] B. Corry, S.-H. Chung, “Mechanisms of valence selectivity in biological ion channels.”, *Cell. Mol. Life Sci.* **Feb. 2006**, *63*, 301–15 (cit. on p. 15).

[78] G. Nagel, D. Ollig, M. Fuhrmann, S. Kateriya, A. M. Musti, E. Bamberg, P. Hegemann, “Channelrhodopsin-1: a light-gated proton channel in green algae.”, *Science* **July 2002**, *296*, 2395–8 (cit. on p. 15).

[79] E. G. Govorunova, E. N. Spudich, C. E. Lane, O. A. Sineshchekov, J. L. Spudich, “New channelrhodopsin with a red-shifted spectrum and rapid kinetics from Mesostigma viride.”, *MBio* **Jan. 2011**, *2*, e00115–11 (cit. on p. 15).

[80] F. Zhang, M. Prigge, F. Beyrière, S. P. Tsunoda, J. Mattis, O. Yizhar, P. Hegemann, K. Deisseroth, “Red-shifted optogenetic excitation: a tool for fast neural control derived from Volvox carteri.”, *Nat. Neurosci.* **June 2008**, *11*, 631–3 (cit. on p. 15).

[81] F. Zhang, J. Vierock, O. Yizhar, L. E. Fenno, S. Tsunoda, A. Kianianmomeni, M. Prigge, A. Berndt, J. Cushman, J. Polle, J. Magnuson, P. Hegemann, K. Deisseroth, “The microbial opsin family of optogenetic tools.”, *Cell* **Dec. 2011**, *147*, 1446–57 (cit. on p. 15).

[82] S.-Y. Hou, E. G. Govorunova, M. Ntefidou, C. E. Lane, E. N. Spudich, O. A. Sineshchekov, J. L. Spudich, “Diversity of Chlamydomonas channelrhodopsins.”, *Photochem. Photobiol.* **Jan. 2012**, *88*, 119–28 (cit. on p. 15).

[83] A. P. Plazzo, N. De Franceschi, F. Da Broi, F. Zonta, M. F. Sanasi, F. Filippini, M. Mongillo, “Bioinformatic and mutational analysis of channelrhodopsin-2 protein cation-conducting pathway.”, *J. Biol. Chem.* **Feb. 2012**, *287*, 4818–25 (cit. on p. 15).

[84] J. Y. Lin, M. Z. Lin, P. Steinbach, R. Y. Tsien, “Characterization of engineered channelrhodopsin variants with improved properties and kinetics.”, *Biophys. J.* **Mar. 2009**, *96*, 1803–14 (cit. on p. 15).

[85] A. Berndt, M. Prigge, D. Gradmann, P. Hegemann, “Two open states with progressive proton selectivities in the branched channelrhodopsin-2 photocycle.”, *Biophys. J.* **Mar. 2010**, *98*, 753–61 (cit. on p. 15).

[86] F. Schneider, D. Gradmann, P. Hegemann, “Ion selectivity and competition in channelrhodopsins.”, *Biophys. J.* **July 2013**, *105*, 91–100 (cit. on p. 15).

[87] K. Feldbauer, D. Zimmermann, V. Pintschovius, J. Spitz, C. Bamann, E. Bamberg, “Channelrhodopsin-2 is a leaky proton pump.”, *Proc. Natl. Acad. Sci. U. S. A.* **July 2009**, *106*, 12317–22 (cit. on p. 15).

[88] M. Nack, I. Radu, B.-J. Schultz, T. Resler, R. Schlesinger, A.-N. Bondar, C. del Val, S. Abbruzzetti, C. Viappiani, C. Bamann, E. Bamberg, J. Heberle, “Kinetics of proton release and uptake by channelrhodopsin-2.”, *FEBS Lett.* **May 2012**, *586*, 1344–8 (cit. on p. 15).

[89] L. E. Fenno, O. Yizhar, K. Deisseroth, “The development and application of optogenetics.”, *Annu. Rev. Neurosci.* **Jan. 2011**, *34*, 389–412 (cit. on p. 16).

[90] H. E. Kato, F. Zhang, O. Yizhar, C. Ramakrishnan, T. Nishizawa, K. Hirata, J. Ito, Y. Aita, T. Tsukazaki, S. Hayashi, P. Hegemann, A. D. Maturana, R. Ishitani, K. Deisseroth, O. Nureki, "Crystal structure of the channelrhodopsin light-gated cation channel.", *Nature* **Feb. 2012**, *482*, 369–74 (cit. on pp. 16–18, 68, 70, 71, 73, 78, 123, 130).

[91] M. Müller, C. Bamann, E. Bamberg, W. Kühlbrandt, "Projection structure of channelrhodopsin-2 at 6 Åresolution by electron crystallography.", *J. Mol. Biol.* **Nov. 2011**, *414*, 86–95 (cit. on p. 16).

[92] M.-K. Verhoefen, C. Bamann, R. Blöcher, U. Förster, E. Bamberg, J. Wachtveitl, "The photocycle of channelrhodopsin-2: ultrafast reaction dynamics and subsequent reaction steps.", *Chemphyschem* **Oct. 2010**, *11*, 3113–22 (cit. on p. 18).

[93] M.-K. Neumann-Verhoefen, K. Neumann, C. Bamann, I. Radu, J. Heberle, E. Bamberg, J. Wachtveitl, "Ultrafast infrared spectroscopy on channelrhodopsin-2 reveals efficient energy transfer from the retinal chromophore to the protein.", *J. Am. Chem. Soc.* **May 2013**, *135*, 6968–76 (cit. on p. 18).

[94] O. P. Ernst, P. A. Sánchez Murcia, P. Daldrop, S. P. Tsunoda, S. Kateriya, P. Hegemann, "Photoactivation of channelrhodopsin.", *J. Biol. Chem.* **Jan. 2008**, *283*, 1637–43 (cit. on p. 18).

[95] V. A. Lórenz-Fonfría, T. Resler, N. Krause, M. Nack, M. Gossing, G. Fischer von Mollard, C. Bamann, E. Bamberg, R. Schlesinger, J. Heberle, "Transient protonation changes in channelrhodopsin-2 and their relevance to channel gating.", *Proc. Natl. Acad. Sci. U. S. A.* **Apr. 2013**, *110*, E1273–81 (cit. on pp. 18, 124).

[96] C. Bamann, T. Kirsch, G. Nagel, E. Bamberg, "Spectral Characteristics of the Photocycle of Channelrhodopsin-2 and Its Implication for Channel Function", *J. Mol. Biol.* **Jan. 2008**, *375*, 686–694 (cit. on pp. 18, 67, 123).

[97] C. Bamann, R. Gueta, S. Kleinlogel, G. Nagel, E. Bamberg, "Structural guidance of the photocycle of channelrhodopsin-2 by an interhelical hydrogen bond.", *Biochemistry* **Jan. 2010**, *49*, 267–278 (cit. on pp. 18, 67, 123, 125).

[98] K. Stehfest, P. Hegemann, "Evolution of the channelrhodopsin photocycle model.", *Chemphyschem* **Apr. 2010**, *11*, 1120–6 (cit. on p. 18).

[99] V. a. Lórenz-Fonfría, J. Heberle, "Channelrhodopsin unchained: Structure and mechanism of a light-gated cation channel", *Biochim. Biophys. Acta - Bioenerg.* **2014**, *1837*, 626–642 (cit. on p. 18).

[100] A. A. Wegener, I. Chizhov, M. Engelhard, H.-J. Steinhoff, "Time-resolved detection of transient movement of helix F in spin-labelled pharaonis sensory rhodopsin II.", *J. Mol. Biol.* **Aug. 2000**, *301*, 881–91 (cit. on pp. 18, 78, 124).

[101] J. P. Klare, E. Bordignon, M. Engelhard, H.-J. Steinhoff, "Sensory rhodopsin II and bacteriorhodopsin: light activated helix F movement.", *Photochem. Photobiol. Sci.* **June 2004**, *3*, 543–547 (cit. on pp. 18, 78, 124).

[102] A. A. Wegener, J. P. Klare, M. Engelhard, H. J. Steinhoff, "Structural insights into the early steps of receptor-transducer signal transfer in archaeal phototaxis.", *EMBO J.* **Oct. 2001**, *20*, 5312–5319 (cit. on pp. 18, 78, 124).

[103] A. Schweiger, G. Jeschke, *Principles of pulse electron paramagnetic resonance*, Oxford University Press, **2001** (cit. on pp. 19, 33, 34).

[104] A. Carrington, A. D. McLachlan, *Introduction to magnetic resonance: with applications to chemistry and chemical physics*, Chapman and Hall, **1979** (cit. on p. 19).

[105] J. A. Weil, J. R. Bolton, *Electron Paramagnetic Resonance: Elementary Theory and Practical Applications*, John Wiley & Sons, **2007** (cit. on p. 19).

[106] W. Gerlach, O. Stern, "Der experimentelle Nachweis der Richtungsquantelung im Magnetfeld", *Zeitschrift für Phys.* **Dec. 1922**, *9*, 349–352 (cit. on p. 19).

[107] P. Zeeman, "On the Influence of Magnetism on the Nature of the Light Emitted by a Substance.", *Astrophys. J.* **May 1897**, *5*, 332 (cit. on p. 19).

[108] Y. K. Zavoisky, "Measurements on CuCl2·2H2O", *J. Phys. USSR* **1945**, *9*, 221 (cit. on p. 19).

[109] Y. K. Zavoisky, "Paramagnetic Absorption In Some Salts In Perpendicular Magnetic Fields", *Zhurnal Eksp. I Teor. Fiz.* **1946**, *16*, 603–606 (cit. on p. 19).

[110] B. Odom, D. Hanneke, B. D'Urso, G. Gabrielse, "New Measurement of the Electron Magnetic Moment Using a One-Electron Quantum Cyclotron", *Phys. Rev. Lett.* **July 2006**, *97*, 30801 (cit. on p. 19).

[111] H. M. McConnell, "Indirect Hyperfine Interactions in the Paramagnetic Resonance Spectra of Aromatic Free Radicals", *J. Chem. Phys.* **1956**, *24*, 764 (cit. on p. 22).

[112] C. Heller, H. M. McConnell, "Radiation Damage in Organic Crystals. II. Electron Spin Resonance of (CO2H)CH2CH(CO2H) in $\beta$-Succinic Acid", *J. Chem. Phys.* **1960**, *32*, 1535 (cit. on pp. 23, 102, 111).

[113] A. Einstein, “Zur Quantentheorie der Strahlung”, *Phys. Zeitschrift* **May 1917**, *18*, 121 (cit. on p. 32).

[114] C. P. Poole, H. A. Farach, *Relaxation in Magnetic Resonance*, Academic Press, Inc., **1971** (cit. on pp. 32, 33).

[115] E. Hahn, “Spin Echoes”, *Phys. Rev.* **Nov. 1950**, *80*, 580–594 (cit. on p. 37).

[116] G. Feher, “Observation of Nuclear Magnetic Resonances via the Electron Spin Resonance Line”, *Phys. Rev.* **Aug. 1956**, *103*, 834–835 (cit. on p. 41).

[117] W. B. Mims, “Pulsed Endor Experiments”, *Proc. R. Soc. A Math. Phys. Eng. Sci.* **Jan. 1965**, *283*, 452–457 (cit. on p. 41).

[118] E. Davies, “A new pulse endor technique”, *Phys. Lett. A* **Feb. 1974**, *47*, 1–2 (cit. on p. 41).

[119] D. Whiffen, “ENDOR transition moments”, *Mol. Phys.* **Jan. 1966**, *10*, 595–596 (cit. on pp. 44, 45, 100).

[120] C. Fan, P. E. Doan, C. E. Davoust, B. M. Hoffman, “Quantitative studies of davies pulsed ENDOR”, *J. Magn. Reson.* **June 1992**, *98*, 62–72 (cit. on p. 45).

[121] K. Bowers, W. Mims, “Paramagnetic Relaxation in Nickel Fluosilicate”, *Phys. Rev.* **July 1959**, *115*, 285–295 (cit. on p. 48).

[122] M. Nechtschein, J. S. Hyde, “Pulsed Electron-Electron Double Resonance in an S = 1 2 , I = 1 2 System”, *Phys. Rev. Lett.* **Mar. 1970**, *24*, 672–674 (cit. on pp. 48, 49).

[123] A. D. Milov, K. M. Salikohov, M. D. Shirov, “Application of Endor In Electron-spin Echo For Paramagnetic Center Space Distribution In Solids”, *Fiz. Tverd. Tela* **1981**, *23*, 975–982 (cit. on p. 49).

[124] A. Milov, A. Ponomarev, Y. Tsvetkov, “Electron-electron double resonance in electron spin echo: Model biradical systems and the sensitized photolysis of decalin”, *Chem. Phys. Lett.* **Sept. 1984**, *110*, 67–72 (cit. on p. 49).

[125] A. D. Milov, A. B. Ponomarev, Y. D. Tsvetkov, “Modulation beats of signal of double electron-electron resonance in spin echo for biradical systems”, *J. Struct. Chem.* **1985**, *25*, 710–713 (cit. on p. 49).

[126] R. E. Martin, M. Pannier, F. Diederich, V. Gramlich, M. Hubrich, H. W. Spiess, “Determination of end-to-end distances in a series of TEMPO diradicals of up to 2.8 nm length with a new four-pulse double electron electron resonance experiment”, *Angew. Chemie-international Ed.* **1998**, *37*, 2834–2837 (cit. on p. 49).

[127] M. Pannier, S. Veit, A. Godt, G. Jeschke, H. W. Spiess, “Dead-time free measurement of dipole-dipole interactions between electron spins.”, *J. Magn. Reson.* **Feb. 2000**, *142*, 331–40 (cit. on p. 50).

[128] D. Margraf, B. E. Bode, A. Marko, O. Schiemann, T. F. Prisner, "Conformational flexibility of nitroxide biradicals determined by X-band PELDOR experiments", *Mol. Phys.* **Aug. 2007**, *105*, 2153–2160 (cit. on p. 52).

[129] J. E. Lovett, B. W. Lovett, J. Harmer, "DEER-Stitch: combining three- and four-pulse DEER measurements for high sensitivity, deadtime free data.", *J. Magn. Reson.* **Oct. 2012**, *223*, 98–106 (cit. on p. 54).

[130] W. Mims, "Envelope Modulation in Spin-Echo Experiments", *Phys. Rev. B* **Apr. 1972**, *5*, 2409–2419 (cit. on p. 55).

[131] B. E. Bode, D. Margraf, J. Plackmeyer, G. Dürner, T. F. Prisner, O. Schiemann, "Counting the monomers in nanometer-sized oligomers by pulsed electron-electron double resonance.", *J. Am. Chem. Soc.* **May 2007**, *129*, 6736–45 (cit. on pp. 55, 56).

[132] A. D. Milov, Y. D. Tsvetkov, F. Formaggio, M. Crisma, C. Toniolo, J. Raap, "Self-Assembling Properties of Membrane-Modifying Peptides Studied by PELDOR and CW-ESR Spectroscopies", *J. Am. Chem. Soc.* **Apr. 2000**, *122*, 3843–3848 (cit. on pp. 55, 56).

[133] G. Jeschke, G. Panek, A. Godt, A. Bender, H. Paulsen, "Data analysis procedures for pulse ELDOR measurements of broad distance distributions", *Appl. Magn. Reson.* **Mar. 2004**, *26*, 223–244 (cit. on p. 56).

[134] A. D. Milov, A. G. Maryasov, Y. D. Tsvetkov, "Pulsed electron double resonance (PELDOR) and its applications in free-radicals research", *Appl. Magn. Reson.* **Aug. 1998**, *15*, 107–143 (cit. on p. 56).

[135] A. V. Astashkin, Y. Kodera, A. Kawamori, "Distance between tyrosines Z+ and D+ in plant Photosystem II as determined by pulsed EPR", *Biochim. Biophys. Acta - Bioenerg.* **Aug. 1994**, *1187*, 89–93 (cit. on p. 56).

[136] H. Hara, A. Kawamori, A. V. Astashkin, T.-a. Ono, "The distances from tyrosine D to redox-active components on the donor side of Photosystem II determined by pulsed electron-electron double resonance", *Biochim. Biophys. Acta - Bioenerg.* **Sept. 1996**, *1276*, 140–146 (cit. on p. 56).

[137] E. T. Whittaker, "On the functions which are represented by the expansions of the interpolation theory", *Proc. R. Soc. A* **1915**, *35*, 181–194 (cit. on p. 57).

[138] Y. Polyhach, E. Bordignon, G. Jeschke, "Rotamer libraries of spin labelled cysteines for protein studies.", *Phys. Chem. Chem. Phys.* **Mar. 2011**, *13*, 2356–66 (cit. on pp. 59, 65, 87, 91).

[139] G. HAGELUEKEN, R. WARD, J. H. NAISMITH, O. SCHIEMANN, "MtsslWizard: In Silico Spin-Labeling and Generation of Distance Distributions in PyMOL.", *Appl. Magn. Reson.* **Apr. 2012**, *42*, 377–391 (cit. on pp. 59, 65, 87).

[140] C. ATILGAN, Z. N. GEREK, S. B. OZKAN, A. R. ATILGAN, "Manipulation of conformational change in proteins by single-residue perturbations.", *Biophys. J.* **Aug. 2010**, *99*, 933–43 (cit. on p. 60).

[141] L. YANG, G. SONG, R. L. JERNIGAN, "Protein elastic network models and the ranges of cooperativity.", *Proc. Natl. Acad. Sci. U. S. A.* **July 2009**, *106*, 12347–52 (cit. on p. 60).

[142] K. HINSEN, "Physical arguments for distance-weighted interactions in elastic network models for proteins.", *Proc. Natl. Acad. Sci. U. S. A.* **Nov. 2009**, *106*, E128 (cit. on p. 60).

[143] A. AMADEI, A. B. LINSSEN, H. J. BERENDSEN, "Essential dynamics of proteins.", *Proteins* **Dec. 1993**, *17*, 412–25 (cit. on p. 60).

[144] L. ORELLANA, M. RUEDA, C. FERRER-COSTA, J. R. LOPEZ-BLANCO, P. CHACÓN, M. OROZCO, "Approaching Elastic Network Models to Molecular Dynamics Flexibility", *J. Chem. Theory Comput.* **Sept. 2010**, *6*, 2910–2923 (cit. on pp. 60, 65).

[145] W. ZHENG, S. DONIACH, "A comparative study of motor-protein motions by using a simple elastic-network model.", *Proc. Natl. Acad. Sci. U. S. A.* **Nov. 2003**, *100*, 13253–8 (cit. on p. 60).

[146] W. ZHENG, B. R. BROOKS, D. THIRUMALAI, "Low-frequency normal modes that describe allosteric transitions in biological nanomachines are robust to sequence variations.", *Proc. Natl. Acad. Sci. U. S. A.* **May 2006**, *103*, 7664–9 (cit. on p. 60).

[147] W. ZHENG, B. R. BROOKS, "Modeling protein conformational changes by iterative fitting of distance constraints using reoriented normal modes.", *Biophys. J.* **June 2006**, *90*, 4327–36 (cit. on p. 60).

[148] G. JESCHKE, "Characterization of Protein Conformational Changes with Sparse Spin-Label Distance Constraints", *J. Chem. Theory Comput.* **Oct. 2012**, *8*, 3854–3863 (cit. on p. 60).

[149] R. P. DIENSTHUBER, C. ENGELHARD, N. LEMKE, T. GLEICHMANN, R. OHLENDORF, R. BITTL, A. MÖGLICH, "Biophysical, Mutational, and Functional Investigation of the Chromophore-Binding Pocket of Light-Oxygen-Voltage Photoreceptors.", *ACS Synth. Biol.* **Mar. 2014**, *9*, DOI `10.1021/sb400205x` (cit. on pp. 61, 98, 99, 137).

[150] C. Engelhard, X. Wang, D. Robles, J. Moldt, L.-O. Essen, A. Batschauer, R. Bittl, M. Ahmad, “Cellular metabolites enhance the light sensitivity of Arabidopsis cryptochrome through alternate electron transfer pathways.”, *Plant Cell* **Nov. 2014**, *26*, 4519–31 (cit. on pp. 61, 116, 117, 119, 121, 137).

[151] N. Krause, C. Engelhard, J. Heberle, R. Schlesinger, R. Bittl, “Structural differences between the closed and open states of channelrhodopsin-2 as observed by EPR spectroscopy.”, *FEBS Lett.* **Oct. 2013**, *587*, 3309–13 (cit. on pp. 61, 137).

[152] J. T. Törring, fsc2, **2015** (cit. on p. 64).

[153] W. L. DeLano, “The PyMOL Molecular Graphics System”, *Schrödinger LLC wwwpymolorg* **2002**, *Version 1.* http://www.pymol.org (cit. on p. 64).

[154] S. Stoll, A. Schweiger, “EasySpin, a comprehensive software package for spectral simulation and analysis in EPR.”, *J. Magn. Reson.* **Jan. 2006**, *178*, 42–55 (cit. on p. 64).

[155] G. Jeschke, V. Chechik, P. Ionita, A. Godt, H. Zimmermann, J. Banham, C. R. Timmel, D. Hilger, H. Jung, “DeerAnalysis2006—a comprehensive software package for analyzing pulsed ELDOR data”, *Appl. Magn. Reson.* **June 2006**, *30*, 473–498 (cit. on p. 65).

[156] G. Hagelueken, D. Abdullin, R. Ward, O. Schiemann, “mtsslSuite: In silico spin labelling, trilateration and distance-constrained rigid body docking in PyMOL.”, *Mol. Phys.* **Oct. 2013**, *111*, 2757–2766 (cit. on pp. 65, 91).

[157] A. Berndt, O. Yizhar, L. A. Gunaydin, P. Hegemann, K. Deisseroth, “Bistable neural state switches.”, *Nat. Neurosci.* **Feb. 2009**, *12*, 229–234 (cit. on pp. 67, 123).

[158] T. H. Bayburt, S. G. Sligar, Membrane protein assembly into Nanodiscs, **2010** (cit. on pp. 75, 123).

[159] J. K. Lanyi, B. Schobert, “Local-global conformational coupling in a heptahelical membrane protein: transport mechanism from crystal structures of the nine states in the bacteriorhodopsin photocycle.”, *Biochemistry* **2004**, *43*, 3–8 (cit. on p. 77).

[160] G. Váró, R. Needleman, J. K. Lanyi, “Protein structural change at the cytoplasmic surface as the cause of cooperativity in the bacteriorhodopsin photocycle.”, *Biophys. J.* **1996**, *70*, 461–467 (cit. on p. 77).

[161] Z. Tokaji, “Cooperativity-regulated parallel pathways of the bacteriorhodopsin photocycle”, *FEBS Lett.* **1995**, *357*, 156–160 (cit. on p. 77).

[162] N. A. Dencher, D. Dresselhaus, G. Zaccai, G. Büldt, "Structural changes in bacteriorhodopsin during proton translocation revealed by neutron diffraction.", *Proc. Natl. Acad. Sci. U. S. A.* **1989**, *86*, 7876–7879 (cit. on pp. 78, 124).

[163] M. H. J. Koch, N. A. Dencher, D. Oesterhelt, H. J. Plohn, G. Rapp, G. Buldt, "Time-resolved X-ray diffraction study of structural changes associated with the photocycle of bacteriorhodopsin", *EMBO J.* **1991**, *10*, 521–526 (cit. on pp. 78, 124).

[164] M. Nakasako, M. Kataoka, Y. Amemiya, F. Tokunaga, "Crystallographic characterization by X-ray diffraction of the M-intermediate from the photocycle of bacteriorhodopsin at room temperature.", *FEBS Lett.* **Nov. 1991**, *292*, 73–75 (cit. on pp. 78, 124).

[165] H. J. Sass, I. W. Schachowa, G. Rapp, M. H. J. Koch, D. Oesterhelt, N. A. Dencher, G. Büldt, "The tertiary structural changes in bacteriorhodopsin occur between M states: X-ray diffraction and Fourier transform infrared spectroscopy", *EMBO J.* **Apr. 1997**, *16*, 1484–91 (cit. on pp. 78, 124).

[166] S. Subramaniam, M. Gerstein, D. Oesterhelt, R. Henderson, "Electron diffraction analysis of structural changes in the photocycle of bacteriorhodopsin.", *EMBO J.* **1993**, *12*, 1–8 (cit. on pp. 78, 124).

[167] A. Okafuji, A. Schnegg, E. Schleicher, K. Möbius, S. Weber, "G-tensors of the flavin adenine dinucleotide radicals in glucose oxidase: A comparative multifrequency electron paramagnetic resonance and electron-nuclear double resonance", *J. Phys. Chem. B* **2008**, *112*, 3568–3574 (cit. on p. 100).

[168] A. S. Halavaty, K. Moffat, "N- and C-terminal flanking regions modulate light-induced signal transduction in the LOV2 domain of the blue light sensor phototropin 1 from Avena sativa.", *Biochemistry* **Dec. 2007**, *46*, 14001–9 (cit. on p. 108).

[169] M. T. A. Alexandre, J. C. Arents, R. Van Grondelle, K. J. Hellingwerf, J. T. M. Kennis, "A base-catalyzed mechanism for dark state recovery in the Avena sativa phototropin-1 LOV2 domain", *Biochemistry* **Mar. 2007**, *46*, 3129–37 (cit. on p. 109).

[170] J. P. Zayner, T. R. Sosnick, "Factors that control the chemistry of the LOV domain photocycle", *PLoS One* **Jan. 2014**, *9*, 87074 (cit. on p. 109).

[171] R. Wenzel, PhD thesis, Freie Universität Berlin, **2011** (cit. on pp. 111, 114, 129, 130).

[172] N. Hoang, E. Schleicher, S. Kacprzak, J.-P. P. Bouly, M. Picot, W. Wu, A. Berndt, E. Wolf, R. Bittl, M. Ahmad, “Human and Drosophila cryptochromes are light activated by flavin photoreduction in living cells”, *PLoS Biol.* **July 2008**, *6*, 6 (cit. on pp. 114, 122).

[173] J.-P. P. Bouly, B. Giovani, A. Djamei, M. Mueller, A. Zeugner, E. A. Dudkin, A. Batschauer, M. Ahmad, “Novel ATP-binding and autophosphorylation activity associated with Arabidopsis and human cryptochrome-1”, *Eur. J. Biochem.* **June 2003**, *270*, 2921–2928 (cit. on p. 116).

[174] D. Immeln, R. Schlesinger, J. Heberle, T. Kottke, “Blue light induces radical formation and autophosphorylation in the light-sensitive domain of Chlamydomonas cryptochrome”, *J. Biol. Chem.* **July 2007**, *282*, 21720–21728 (cit. on p. 117).

[175] T. Biskup, B. Paulus, A. Okafuji, K. Hitomi, E. D. Getzoff, S. Weber, E. Schleicher, “Variable electron transfer pathways in an amphibian cryptochrome tryptophan versus tyrosine-based radical pairs”, *J. Biol. Chem.* **Mar. 2013**, *288*, 9249–60 (cit. on pp. 119, 129, 130).

[176] P. Müller, J.-P. Bouly, K. Hitomi, V. Balland, E. D. Getzoff, T. Ritz, K. Brettel, “ATP binding turns plant cryptochrome into an efficient natural photoswitch.”, *Sci. Rep.* **Jan. 2014**, *4*, 5175 (cit. on p. 119).

[177] R. J. Gegear, L. E. Foley, A. Casselman, S. M. Reppert, “Animal cryptochromes mediate magnetoreception by an unconventional photochemical mechanism.”, *Nature* **Feb. 2010**, *463*, 804–807 (cit. on p. 122).

[178] A. T. Vaidya, D. Top, C. C. Manahan, J. M. Tokuda, S. Zhang, L. Pollack, M. W. Young, B. R. Crane, “Flavin reduction activates Drosophila cryptochrome.”, *Proc. Natl. Acad. Sci. U. S. A.* **Dec. 2013**, *110*, 20455–60 (cit. on p. 122).

[179] F. Zhang, A. M. Aravanis, A. Adamantidis, L. de Lecea, K. Deisseroth, “Circuit-breakers: optical technologies for probing neural signals and systems.”, *Nat. Rev. Neurosci.* **Aug. 2007**, *8*, 577–81 (cit. on p. 123).

[180] E. Ritter, K. Stehfest, A. Berndt, P. Hegemann, F. Bartl, “Monitoring light-induced structural changes of Channelrhodopsin-2 by UV-visible and Fourier transform infrared spectroscopy.”, *J. Biol. Chem.* **Dec. 2008**, *283*, 35033–41 (cit. on p. 123).

[181] I. Radu, C. Bamann, M. Nack, G. Nagel, E. Bamberg, J. Heberle, “Conformational changes of channelrhodopsin-2.”, *J. Am. Chem. Soc.* **June 2009**, *131*, 7313–9 (cit. on p. 123).

[182] T. Sattig, C. Rickert, E. Bamberg, H.-J. J. Steinhoff, C. Bamann, “Light-induced movement of the transmembrane helix B in channelrhodopsin-2.”, *Angew. Chemie - Int. Ed.* **Sept. 2013**, *52*, 9705–9708 (cit. on pp. 124, 130).

[183] K. Stehfest, E. Ritter, A. Berndt, F. Bartl, P. Hegemann, “The branched photocycle of the slow-cycling channelrhodopsin-2 mutant C128T.”, *J. Mol. Biol.* **May 2010**, *398*, 690–702 (cit. on p. 125).

[184] A. Möglich, K. Moffat, “Structural basis for light-dependent signaling in the dimeric LOV domain of the photosensor YtvA.”, *J. Mol. Biol.* **Oct. 2007**, *373*, 112–26 (cit. on p. 125).

[185] A. Hahn, C. Engelhard, S. Reschke, C. Teutloff, R. Bittl, S. Leimkühler, T. Risse, “Structural insights into the incorporation of the Mo cofactor into sulfite oxidase from site directed spin labeling”, *Angew. Chemie - Int. Ed.* **2015**, *in press*, DOI `10.1002/anie.201504772R1` (cit. on p. 138).

# ACKNOWLEDGEMENTS

No man is an island, and so there are many people to thank for having helped in getting me to this point, with only this Thank You left to write. This thesis has been written in English, but thanking people in English with whom I converse almost entirely in German feels rather silly. So.

Vielen, herzlichen Dank an, in keiner bestimmten Reihenfolge,

Robert Bittl, weil er mich für EPR begeistert und mir damit das Feld der Biophysik eröffnet hat, weil er immer Zeit für Hilfe und Erklärungen hatte, jederzeit auch selber Probleme im Labor anpackt, aber mich auch hat arbeiten lassen, wie ich wollte – selbst wenn „wie ich wollte" mitunter mehr nach Elektrotechnik ausgesehen haben muss,

Nils Krause, Ralph Diensthuber, Nora Lemke, und Xuecong Wang in den Gruppen von Margaret Ahmad, Andreas Möglich und Ramona Schlesinger, von denen ich über die Jahre eine ungeheure Menge an Proben erhalten habe, und ohne deren unermüdliche Arbeit dieses Werk sehr, sehr kurz geworden wäre,

nochmal Nils, der nicht nur Kanalrhodopsin-Proben gemacht hat, sondern mit dem ich Ergebnisse diskutiert, Ideen entwickelt, Experimente geplant und in dunklen Laboren gestanden habe – viel Erfolg bei deiner eigenen, bald fertigen Doktorarbeit. Ralph und Andreas, mit LOV Proteinen statt Kanalrhodopsin, sonst aber aus denselben Gründen, sogar inklusive der dunklen Labore,

meine Eltern, meine Geschwister und meine Freunde, die mich auf jedem Schritt des Weges begleitet und unterstützt haben,

Richard, Christian und Julia, mit denen ich viel meine Ergebnisse diskutiert habe und die mir oft geholfen haben, Dinge klarer zu sehen,

allen anderen Mitgliedern der AG Bittl, aktuell und ehemalig, mit denen zusammenzuarbeiten immer eine Freude war.